PATTERNS AND INSTABILITIES AT A DRIVEN FLUID-AIR INTERFACE

LIHONG PAN

PATTERNS AND INSTABILITIES AT A DRIVEN FLUID-AIR INTERFACE.

by

Lihong Pan

A THESIS SUBMITTED TO THE SCHOOL OF GRADUATE STUDIES IN PARTIAL FULFILLMENT OF THE REQUIREMENTS FOR THE DEGREE OF DOCTOR OF PHILOSOPHY

DEPARTMENT OF PHYSICS
MEMORIAL UNIVERSITY OF NEWFOUNDLAND
DECEMBER 1993

Abstract

We have studied experimentally the dynamical behaviour of a driven fluid-air interface in the system known as the printer's instability. The system consists of two horizontal cylinders, one mounted eccentrically inside the other, with the narrow part of the gap between them filled with a viscous oil. As one or both of the cylinders rotate, the straight oil-air interface becomes unstable, and the interface displays a variety of dynamical states. These include stationary and traveling finger patterns, solitary waves, and spatio-temporal chaos. Measurements of the onset and development of the stationary finger pattern observed when only one cylinder rotates indicate that finite-size effects delay the onset of the fingering instability. When the two cylinders counter-rotate, we observe a supercritical parity-breaking transition, at which the stationary pattern loses its reflection symmetry and begins to drift along the apparatus. From measurements of the degree of asymmetry of the drifting pattern as a function of the experimental control parameter, we find that the asymmetry increases with the square root of the control parameter, and that the drift velocity is linear in the asymmetry. This behaviour is in accord with recent theoretical predictions. At low values of the control parameter, the drifting pattern is disordered, also in agreement with theoretical results. We have also observed a nonuniform traveling pattern in which the fingers become unstable to the Eckhaus instability, and we measure the Eckhaus stability boundary for this system.

Acknowledgements

As a graduate student, I have benefited immeasurably from the support, advice, and friendship of my supervisor, John de Bruyn. Without his guidance, this thesis would not exist. I thank Bill Kieley and Paul Martin for making the apparatus. I am grateful for helpful discussions with Raymond Goldstein, Wim van Saarloos and Jim Gleeson. Financial support from Memorial University of Newfoundland is gratefully acknowledged.

Table of Contents

List of Tables vi

List of Figures ix

1 Introduction 1

1.1 Pattern formation and the printer's instability 1

1.2 Previous work 7

1.3 Summary of this work 12

2 Theory 15

2.1 Linear stability analysis 15

2.2 Parity breaking 24

2.2.1 Symmetry argument 24

2.2.2 $q - 2q$ mode coupling 26

2.3 Instabilities of the traveling-wave state 28

2.3.1 Results from complex Ginzburg-Landau equation 29

2.3.2 Results from asymmetry equations 33

3 Apparatus 36

4 Experimental Results with One Cylinder Rotating 43

4.1 Experimental results with $\mathbf{r_1 = 50.4}$ mm 43

4.1.1 Results with outer cylinder rotating 44

4.1.2 Results with inner cylinder rotating 49

4.2 Experimental results with $r_1 = 24.85$ mm 65
4.3 Discussion 68

5 Experimental Results with Cylinders Counter-Rotating **74**

5.1 Results 74
5.1.1 Uniform broken-parity waves 75
5.1.2 Nonuniform broken-parity waves 78
5.2 Analysis and discussion 92
5.2.1 Uniform traveling waves at low ϵ_a 94
5.2.2 Nonuniform traveling-wave state 107

6 Conclusions **122**

Bibliography **124**

List of Tables

3.1 Fluid properties 39

List of Figures

1.1 A cross-sectional view of the experimental apparatus. 3

1.2 Examples of patterns observed in the experiment. 5

1.3 Dynamical phase diagram of the interface 6

2.1 Calculated linear stability boundary of the straight meniscus. 23

2.2 Stability diagram of traveling-wave state for the Ginzburg-Landau equation. 31

2.3 Linear stability diagram of the traveling-wave state from the coupled amplitude and phase equations. 34

3.1 Schematic drawing of the experimental apparatus. 37

3.2 Block diagram of the experimental apparatus. 41

4.1 Development of the finger pattern when the outer cylinder rotates. . . 45

4.2 Finger amplitude vs. outer cylinder capillary number Ca_o. 46

4.3 Pattern wavelength vs. Ca_o. 47

4.4 Onset capillary number Ca_c vs. dimensionless gap thickness b_o/R. . . 50

4.5 Pattern wavelength at onset λ_c/R vs. b_0/R. 51

4.6 Phase diagram when the bigger inner cylinder rotates. 53

4.7 Development of the pattern when the bigger inner cylinder rotates. . 54

4.8 Finger amplitude vs. Ca_i at onset for $b_0/R = 0.0024$. 55

4.9 Disordered and traveling patterns observed with the bigger inner cylinder rotating. 58

4.10 Finger amplitude vs. Ca_i at onset for $b_0/R = 0.0046$. 59

4.11 Finger amplitude vs. Ca_i for the bigger inner cylinder. 60
4.12 Width of the hysteresis loop at onset for the bigger inner cylinder. . . 62
4.13 Pattern wavelength λ vs. Ca_i for the bigger inner cylinder. 64
4.14 Finger amplitude and wavelength vs. Ca_o for the smaller inner cylinder. 66
4.15 Finger amplitude and wavelength vs. Ca_i for the smaller inner cylinder. 67
4.16 Comparison of present results with previous work. 69

5.1 Uniform traveling patterns. 76
5.2 Space-time image of a uniform traveling pattern. 77
5.3 v_ϕ^2 vs. v_i for uniform traveling waves. 79
5.4 Pattern wave number vs. v_i. 80
5.5 Nonuniform traveling-finger patterns. 82
5.6 Space-time image of a nonuniform traveling pattern. 84
5.7 The local properties of a nonuniform traveling pattern. 85
5.8 v_ϕ^2 vs. v_i at $v_o = 174.3$ mm/s 87
5.9 v_ϕ^2 vs. v_i at $v_o = 435.7$ mm/s. 88
5.10 The formation of a new finger through the Eckhaus instability. 90
5.11 Space-time image of a drifting pattern showing the Eckhaus instability. 91
5.12 The measured Eckhaus stability boundary for traveling waves. 93
5.13 Fourier amplitudes for a stationary pattern and a drifting pattern. . . 97
5.14 $\mathcal{A}^2$ vs. v_i for uniform traveling pattern. 98
5.15 v_ϕ vs. $\mathcal{A}$ for uniform traveling waves. 100
5.16 Fourier amplitudes of the pattern vs. the control parameter, v_i. . . . 101
5.17 Fourier amplitude of the second spatial harmonic vs. that of the first. 103
5.18 The phase mismatch angle θ vs. the control parameter, v_i. 104
5.19 The pattern's phase velocity against the quantity b_2/q. 106
5.20 The transformed interface $U(l)$ and its Fourier amplitudes. 108

5.21 The two asymmetry parameters, $\mathcal{A}'$ vs. $\mathcal{A}$ from our experiments. . . . 110
5.22 The two asymmetry parameters, $\mathcal{A}'$ vs. $\mathcal{A}$, from simulations. 111
5.23 $\mathcal{A}^2$ vs. v_t at $v_o = 171.3$ mm/s. 113
5.24 v_ϕ vs. $\mathcal{A}$ for $v_o = 171.3$ mm/s. 114
5.25 (a) v_ϕ vs. $\mathcal{A}$ for a nonuniform pattern. (b) ω vs. v_o. 115
5.26 Partial phase diagram of Ref. [81]. 117
5.27 Fig. 14 of Ref. [27], showing spatiotemporal grain boundaries in extended traveling wave. 119

Chapter 1

Introduction

1.1 Pattern formation and the printer's instability

Many dynamical systems undergo instabilities as they are driven out of equilibrium by a driving force. These instabilities can lead to the formation of patterns — states with some form of regular spatial and/or temporal structure. The adjustable driving force is referred to as the control parameter. When this parameter is small, the system is typically in a spatially uniform state. When it is increased to a certain value, a bifurcation — that is, a transition from one state to another — occurs, at which the system loses its original symmetry and goes into a lower symmetry state which exhibits a pattern. When the control parameter is increased further, or when a second control parameter is varied, this pattern can itself become unstable to secondary, and then higher order instabilities, successively breaking the symmetries of the pattern. The global dynamics of the system can go from simple to very complicated, at some stage becoming time dependent and eventually turbulent.

Instabilities in pattern-forming systems have been studied extensively in recent years [1]. Relative to fully three-dimensional pattern-forming systems, one-dimensional systems have the advantage of simplicity, which allows meaningful comparisons of experimental results with theoretical or numerical predictions. A quantitative understanding of several one-dimensional pattern forming systems has been achieved. An important example is Rayleigh-Bénard convection [2-4], in which a thin horizontal fluid layer, confined between two rigid plates, is heated from below.

The temperature difference, ΔT, between the top and bottom of the layer causes the density of the fluid to increase with height. This leads to a potential instability, since the heavier, colder fluid sits above the lighter, warmer fluid. When the control parameter, ΔT, is raised above a critical value, a convection pattern consisting of straight, parallel rolls develops. Rayleigh-Bénard convection has been studied extensively both experimentally [3, 5], and in theory [2, 3], and the experimental and theoretical results agree with each other very well. Other well known one-dimensional pattern-forming systems include Taylor-Couette flow [3, 6], in which the space between two concentric rotating cylinders is fully filled with fluid, and the spatially uniform base state becomes unstable to the formation of vortices above a certain value of the cylinder rotation speed; Taylor-Dean flow [7, 8], which is similar to Taylor-Couette flow, but with the space between the cylinders only partially filled with fluid; directional solidification [9-11], in which a sample, placed in a temperature gradient such that it contains an interface between two different phases, is pulled in the direction of decreasing temperature, and the interface becomes unstable above a certain pulling speed; and the so-called printer's instability [12-17] which is the system studied in this thesis. A rich variety of nonlinear dynamical phenomena has been observed in the printer's instability [12]. We believe that further study of this experimental system will add to the understanding of the dynamics of one-dimensional patterns.

The apparatus used to study the printer's instability in our experiment is composed of two horizontal, parallel, but vertically offset cylinders, one inside the other, such that the cross section is as in Fig. 1.1. A quantity of viscous fluid, just enough to keep the bottom part of the gap between the cylinders filled, is introduced into this gap. When one or both of the cylinders rotate, a variety of dynamical states is observed at the fluid-air interface running the length of the cylinders, depending on

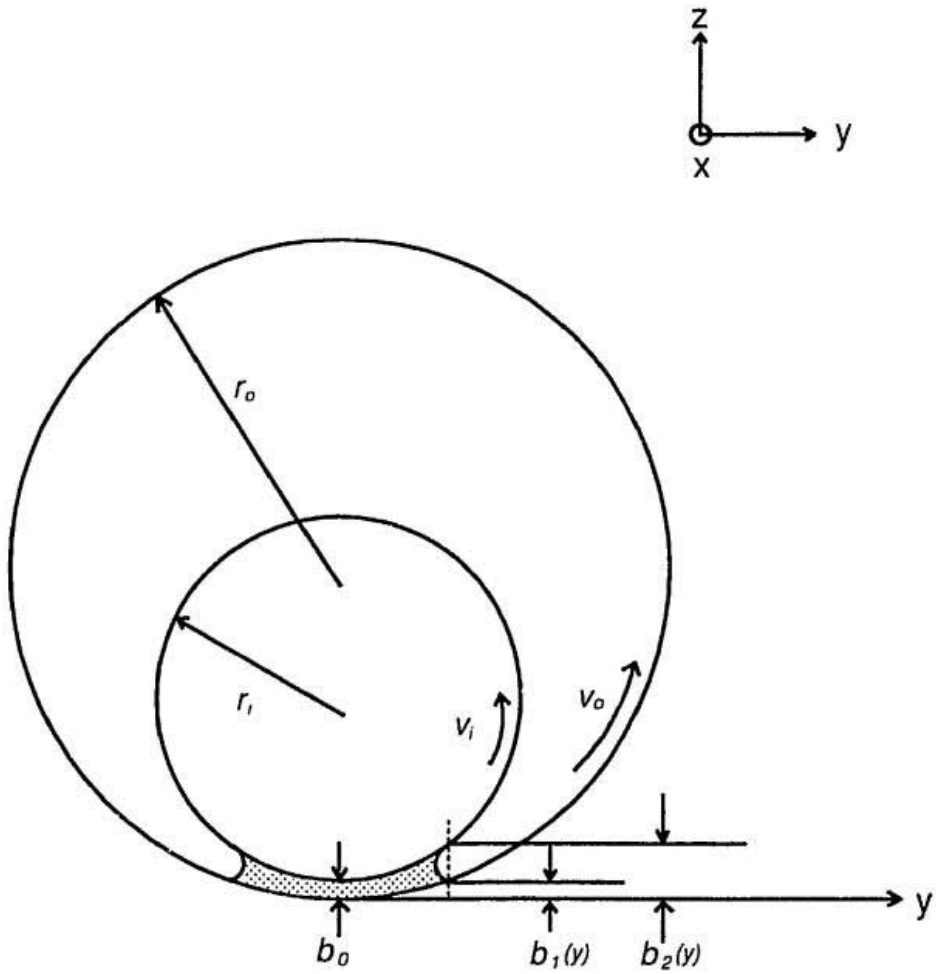

Figure 1.1: A cross-sectional view of the experimental apparatus.

the rotation speeds of the cylinders. Some typical interface patterns are shown in Fig. 1.2. These include a stationary fingering pattern which consists of symmetric, stationary, periodic fingers (Fig. 1.2(a)); a traveling-wave pattern consisting of asymmetric, periodic traveling fingers (Fig. 1.2(b)); solitary traveling waves in the form of localized patches of asymmetric fingers propagating through a background of stationary fingers (Fig. 1.2(c)); and spatio-temporal chaos, in which fingers are formed and destroyed constantly (Fig. 1.2(d)). Fig. 1.3 is the measured dynamical phase diagram of our system, in the space defined by the two control parameters v_i and v_o, the inner and outer cylinder surface speeds, respectively. In the region labeled S, the straight interface is unstable to a pattern of stationary fingers. In the region labeled SW, solitary waves are observed. TW indicates a state in which the entire interface consists of asymmetry traveling fingers, and STC indicates the region where the pattern is spatio-temporally chaotic.

The transition from the stationary, symmetric pattern of Fig. 1.2(a) to the traveling, asymmetric pattern of Fig. 1.2(b) is an example of a parity-breaking bifurcation, at which the pattern's reflection, or parity, symmetry is broken. Both localized regions of broken parity, which propagate through a stationary background pattern, and extended broken-parity traveling-wave states have been observed in several laboratory systems [9-13,18-24]. Parity-breaking bifurcations have also recently been the subject of much theoretical work [25-41]. Parity-breaking was shown to be one of ten possible generic secondary instabilities of stationary one-dimensional patterns by Coullet and Iooss [42]. The parity-breaking bifurcation in our experimental system will be discussed in detail in Chapter 5.

Another well-known instability of one-dimensional pattern is the Eckhaus instability [43]. At a supercritical bifurcation (analogous to a second-order transition in the mean-field theory of phase transition) to a state with a stationary spatial pat-

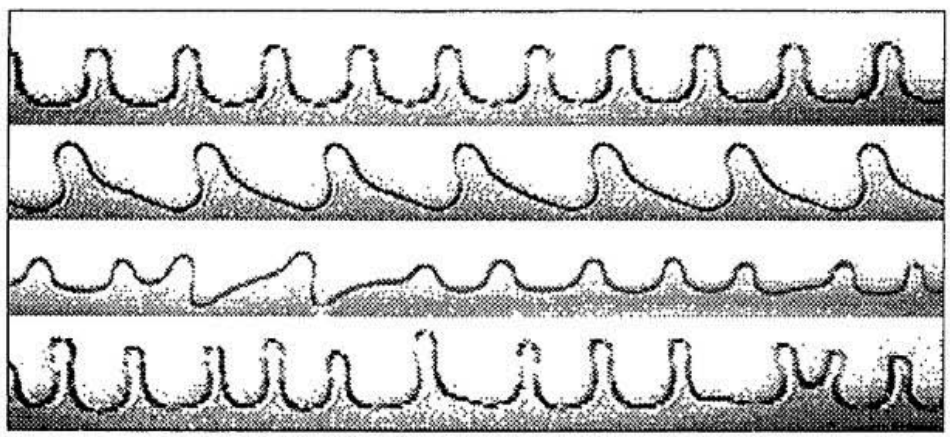

Figure 1.2: Examples of patterns observed at the oil-air interface in the printer's instability experiment. (a) Symmetric, stationary fingers; (b) a asymmetric fingers drifting to the right; (c) solitary wave traveling in the background of stationary fingers ; (d) spatio-temporal chaos.

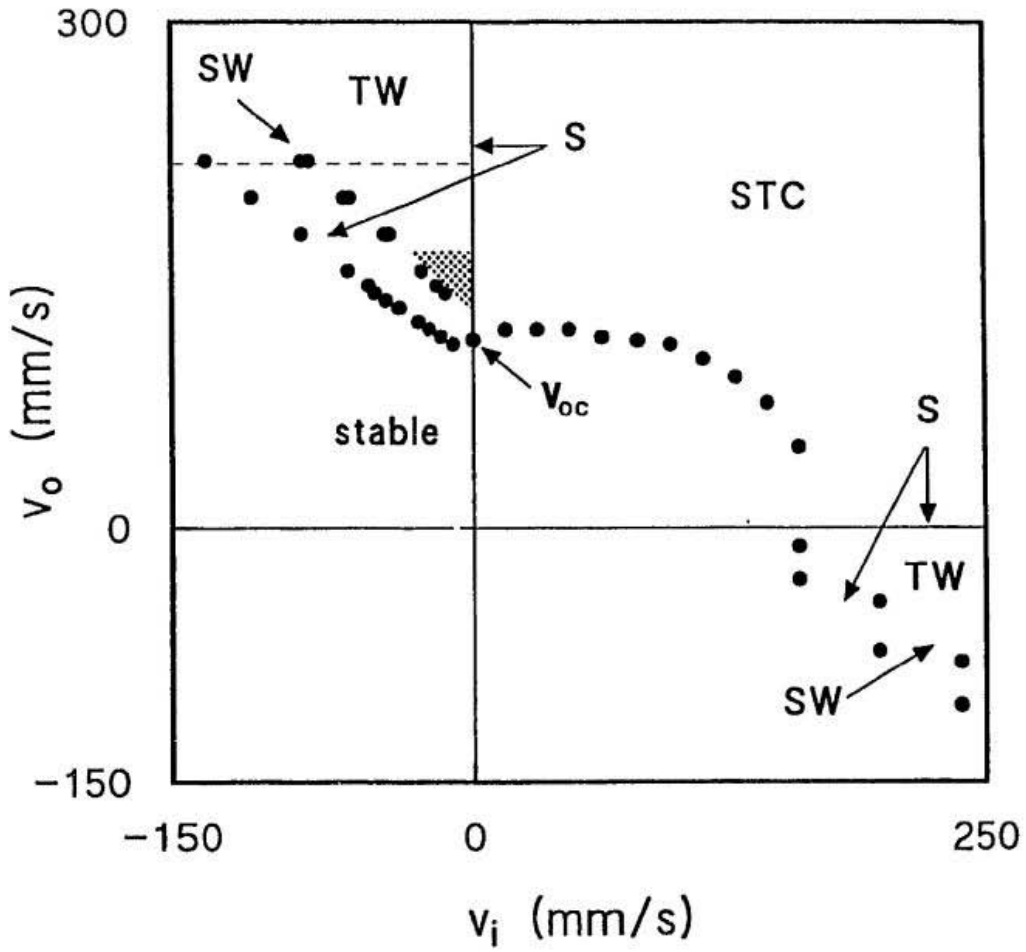

Figure 1.3: Dynamical phase diagram of the interface, in terms of the rotation speeds of the two cylinders. S - stationary fingers; TW - traveling waves; STC - spatio-temporal chaos; SW - solitary waves.

tern, the uniform base state becomes unstable to perturbations of a particular wave number, while above the onset, it is linearly unstable to perturbations within a band of wave numbers. Not all wave numbers within this band lead to stable patterns, however, the pattern is only stable in a narrower wavenumber band defined by the Eckhaus boundary [43, 44]. Patterns with wave numbers lying outside the Eckhaus boundary are unstable to a long-wavelength phase instability, which eventually leads to the gain or loss of individual pattern units so as to bring the pattern back inside the Eckhaus-stable band. This is called Eckhaus instability. The Eckhaus instability has been studied in several systems displaying stationary patterns [9,45-51]. The Eckhaus instability also affects traveling-wave patterns, but it is only recently that it has been studied in this context [4,52-58]. We have observed the Eckhaus instability in the traveling-wave state in our experimental system, and will discuss our results in Chapter 5.

1.2 Previous work

The primary motivation for much of the previous work on the printer's instability has come from industrial coating applications: instabilities that arise when a thin layer of fluid is spread or coated onto a surface lead to an uneven coating thickness, often called ribbing, which is generally undesirable. Fluid dynamical systems with different geometries have been used to model practical coating systems, and the dynamical behaviour of viscous fluids in the narrow passages between two moving surfaces or between a moving and a stationary surface has been extensively investigated, both experimentally and theoretically, over the last thirty years [59-70]. More recently, the ideas of nonlinear dynamics have been applied to problems in coating [71].

Rabaud and Hakim [23] studied the equations of motion of the printer's instability using the lubrication approximation. They pointed out that the equation for the pressure field in the printer's instability,

$$\nabla^2 p + \frac{1}{l(y)}\frac{\partial p}{\partial y} = \frac{2\mu(v_1 + v_2)}{b^2(y)l(y)}, \tag{1.1}$$

where $b(y) = b_2(y) - b_1(y)$ is the gap thickness shown in Fig. 1.1, v_1 and v_2 are the rotation velocities of the two cylinders, μ is the coefficient of viscosity of the fluid, and $l(y) = b(y)/(3db/dy)$, is similar to the equation for the impurity concentration, which governs the slow growth of a crystal in directional solidification,

$$\nabla^2 C + \frac{V}{D}\frac{\partial C}{\partial x} = 0. \tag{1.2}$$

Here C is the impurity concentration, D, the impurity diffusion coefficient, and V, the pulling speed of the container. In a sense the printer's instability is a fluid mechanical analogue of directional solidification, with the pressure field playing the role of the impurity concentration in directional solidification.

For constant thickness, $db/dy = 0$, Eq. (1.1) becomes the Laplace equation, which describes the Saffman-Taylor instability in a Hele-shaw cell [72]. In this system, a more viscous fluid is displaced by a less viscous fluid in the narrow space between two plates, and instabilities arise at the interface between the two fluids. Rabaud et al. [23] compared the shapes of the fingers observed in printer's instability with finger shapes calculated from the equation relevant to the Saffman-Taylor instability, and some similarities have been found.

Rabaud et al. [12] and Couder et al. [13] studied the dynamical behaviour of the printer's instability with an apparatus very similar to that used here — two cylinders, one eccentrically mounted inside the other. They observed the various dynamical states described above, and measured a phase diagram similar to that shown in

Fig. 1.3. Some detailed descriptions of these states can be found in Michalland's thesis [14].

Hakim et al. [73] studied the fingering instability that occurs in a thin layer of silicone oil confined by a single roller rotating above a stationary plane. They observed a continuous transition from the straight meniscus state to a state of stationary fingers. They performed a linear stability analysis of the straight meniscus, similar to that presented earlier by Savage [63, 64]. Their calculated results for the rotation speed at the onset of the instability, and for the onset pattern wavelength, were in reasonably good agreement with their experimental data, while above onset, the pattern wavelength closely followed the low-wavelength edge of the linear stability boundary.

The wavelength selection mechanisms and transient behaviour in the stationary fingering pattern were studied by Rabaud et al. [74] They investigated the various ways in which the pattern relaxed to its preferred wavelength when the rotation speed of the cylinder was changed suddenly. They observed localized disturbances composed of broken-parity fingers propagating through the pattern in much the same way as has been observed in the directional solidification of liquid crystals [75] and of lamellar eutectics [18, 76]. Similar structures also play a role in the development of spatio-temporal intermittency in the case where the two cylinders co-rotate, as studied by Michalland and Rabaud [77]. In Ref. [77], Michalland and Rabaud also studied the out-of-phase damped oscillations of the fingers, which evolve into an optical mode of pulsation after the localized disturbances propagate away. Their results suggested an elastic behaviour of the interface [77].

Michalland et al. [78] investigated the dynamical behaviour of the STC state with the cylinders co-rotating. Decré et al. [79] performed a similar study on a system consisting of two rotating cylinders, one above the other. Both of these

groups studied the statistics of the ordered and chaotic domains, and showed that in both cases, the transition from the ordered state to STC was analogous to a second order phase transition, as found in other theoretical and experimental studies of STC in extended one dimensional systems [80-83].

Cummins et al. [84] studied the printer's instability in an apparatus similar to ours. They increased the inner cylinder speed with the outer cylinder counter-rotating at a fixed low speed (in the fourth quadrant of Fig. 1.3), and observed a sequence of three transitions. First the straight interface became unstable to the stationary finger pattern. Next, there was a transition from the stationary pattern to uniform broken-parity traveling waves, and, finally, the traveling pattern underwent a spatial period-doubling transition. They also observed a pattern made up of coexisting domains of long- and short-wavelength broken-parity traveling fingers.

Parity-breaking transitions have been observed in several other experimental systems, but for the most part have been only qualitatively characterized. The observed broken-parity waves appear to take two forms: localized patches of broken parity, which propagate through an otherwise stationary, symmetric pattern, and extended traveling-wave states, which can include source and sink defects.

A localized broken-parity state was first reported by Simon et al. [9, 10] in experiments on the directional cooling of a liquid crystal at the isotropic-nematic transition. This system was investigated both numerically and analytically by Rappel and co-workers [36-38]. Localized regions of broken parity have also been observed in experiments on Rayleigh-Bénard convection in a narrow slot [11, 22], and in Taylor vortex flow with counter-rotating cylinders [85]. The existence of a parity breaking bifurcation in this last system had been predicted theoretically by Riecke and Paap [39].

Faivre and co-workers have studied broken-parity waves in work on the directional solidification of lamellar eutectics [18-20]. They observed both localized, propagating regions of broken parity [18, 19], and extended regions of uniform propagating cells [20].

Gleeson et al. observed extended regions of propagating, asymmetric cells emanating from a source defect at a grain boundary in a directional solidification experiment [24]. They measured the asymmetry of the traveling cells and demonstrated that the propagation speed was linear in the asymmetry.

Mutabazi and Andereck [8] observed a supercritical bifurcation from a pattern of stationary rolls to an extended state of drifting rolls in the Taylor-Dean system, and concluded that in their system, the drift instability was a result of interactions between the fundamental spatial mode and its second harmonic. This $q-2q$ coupling has been shown to be the cause of the parity-breaking instabilities observed in directional solidification of liquid crystals [37, 38] and in Taylor vortex flow [39].

A secondary instability of a pattern of parametrically excited surface waves in an annular container, leading to a drifting pattern, has been observed by Douady et al. [21]. Fauve et al. showed that this drifting pattern arose from a breaking of parity symmetry [35].

Parity-breaking transitions have been explained through two theoretical approaches. One of these, introduced by Coullet and co-workers [25], and further developed in Refs [26, 27], is based on coupled amplitude and phase equations developed from very general symmetry arguments. The other, which involves the resonant coupling between spatial modes with wave numbers q and $2q$, was first investigated by Malomed and Tribelsky [28], and since then by many other groups [29-40]. In both of these theories, the phase speed of the traveling wave is expected

to be proportional to the asymmetry of the pattern. Both of these theoretical approaches will be discussed in Chapter 2.

The Eckhaus instability has been studied in several systems displaying stationary patterns. These include Taylor-Couette flow [47, 48], electrically-driven convection in liquid crystals [45, 46], and a coating system [51], in which a cylinder coated with an oil film rotates under a horizontal plate. The experimental results on Taylor-Couette flow [47, 48] are in good agreement with theoretical calculations by Riecke and Paap [49]. The Eckhaus instability of a traveling-wave state has been observed recently in Rayleigh-Bénard convection. Janiaud, et al. [54, 55] have studied the Eckhaus instability experimentally in traveling waves produced by the oscillatory instability in Rayleigh-Bénard convection in compressed argon gas, and analytically and numerically in the framework of the complex Ginzburg-Landau equation. Baxter et al. [56] and Kolodner [57, 58] have studied the Eckhaus instability in traveling-wave convection in binary mixtures. The experiments in each of these cases involved preparing the system in a state outside the Eckhaus-stable band and studying its evolution. A modulation of the pattern's phase develops and grows in amplitude, eventually leading to the gain or loss of one wavelength of the oscillatory pattern in the former case [54], or the creation or annihilation of a pair of convection rolls in the latter case [56-58].

1.3 Summary of this work

A variety of dynamical states is observed at the fluid-air interface in our experimental system, as shown in Figs. 1.2 and 1.3. The experiments described in this thesis involve quantitative measurements on some of these states. We studied the formation and development of stationary fingers near the transition at which the straight fluid-air interface loses stability to a stationary fingering pattern. Depending on the

size of the cylinder, and on which of the two cylinders is rotating, the bifurcation to stationary fingers is either imperfect but continuous, or discontinuous, with a small amount of hysteresis. By comparing our results with the theoretical expectations based on linear stability analysis, and with previous experimental results, we find that finite-size effects can substantially delay the onset of the fingering instability. This is the first study of finite-size effects in this type of pattern-forming system, and our results have potential applications in the coating industry.

We have studied in detail the broken-parity traveling patterns observed when the cylinders are in counter-rotation. When the outer cylinder rotation speed is just above its value at the onset of the stationary pattern, with the inner cylinder counter-rotating, a uniform traveling pattern is observed. We find that this pattern appears via a supercritical parity-breaking transition, at which the pattern loses its reflection symmetry and begins traveling along the length of the cylinders. However, when the outer cylinder speed is higher, the traveling patterns are never perfectly uniform, and never perfectly stable. Rather, the pattern's local wavelength, and the finger's asymmetry and traveling speed vary slowly along the pattern. In addition, the finger pattern is intermittently disturbed by transient bursts of disordered behaviour. The variation of wavelength along the pattern in this regime allows us to observe the Eckhaus instability in this traveling-wave system, and we have measured the Eckhaus instability boundary.

A method of measuring the asymmetry of the fingers has been developed using a Fourier transform technique. Measurements of the degree of asymmetry of the traveling pattern as a function of the experimental control parameter show that the asymmetry increases with the square root of the control parameter, and that the drifting speed is linear in the asymmetry. The linear relationship between the traveling speed and asymmetry also holds for the individual fingers of the nonuniform

pattern at a given time. These results are accord with recent theoretical predictions [25-27]. We also compare our results with the predictions of the $q - 2q$ model mentioned above [35], by investigating the behaviour of the spatial modes in the pattern as the control parameter is increased. However, our results do not agree with the predictions of this model. Several possible reasons for this disagreement are suggested. Our quantitative studies of the parity-breaking transition in this system will add to the understanding of the dynamics of one-dimensional patterns.

The remainder of this thesis is organized as follows: in Chapter 2 some important theoretical results are presented. In Chapter 3, we describe our experimental apparatus. Experimental results obtained with one cylinder rotating are presented and discussed in Chapter 4, and results obtained with two cylinders rotating are reported in Chapter 5. Chapter 6 is a brief conclusion.

Chapter 2

Theory

In this chapter, we discuss a number of theoretical topics relevant to our experiments. The stability of the planar interface in our system is investigated by linear stability analysis. The dynamics of the broken-parity traveling-wave state is discussed in terms of the asymmetry of the pattern, as well as a model for parity-breaking involving the coupling of waves with wavenumber q and $2q$. The stability of the broken-parity traveling-wave state with respect to long-wavelength perturbations is analyzed using the complex Ginzburg-Landau equation, and its stability near onset is also discussed.

2.1 Linear stability analysis

The linear stability of coating systems has been studied for over thirty years [59,60,63-65,68-70]. The general idea of linear stability analysis is to add a small perturbation to a base flow, and to see whether the perturbation grows or decays with time. If the perturbation grows with time, the base flow is unstable and a pattern may form. In this section we follow the same route as Hakim et al. [73] did in analyzing the linear stability of of the straight meniscus in the printer's instability. Their treatment is quite similar to that presented by Savage [63, 64]. We first look at the equations for the base state, with a straight interface. In our experimental system, shown in Fig. 1.1, $b_0/R \ll 1$, and $R_e(b_0/R)^2 \ll 1$, where R_e is the Reynolds number, $R_e = vR/\nu$. Here v is the velocity of the fluid, ν is the kinematic viscosity, and R is the effective

radius of the system, defined as

$$\frac{1}{R} = \frac{1}{r_i} - \frac{1}{r_o}. \tag{2.1}$$

We can therefore use the lubrication approximation to describe the flow in the gap [86]. In this approximation, the pressure, p, is only a function of y in our system, and the Navier-Stokes equation for u, the flow velocity, becomes

$$\frac{dp}{dy} = \mu \frac{d^2 u(y,z)}{dz^2}. \tag{2.2}$$

Thus the expression for the flow velocity is

$$u(y,z) = \frac{1}{2\mu}\frac{dp}{dy} z^2 + Az + B. \tag{2.3}$$

No-slip boundary conditions at the surfaces of the two cylinders require

$$u(y, b_1(y)) = v_o \qquad \text{and} \qquad u(y, b_2(y)) = v_i, \tag{2.4}$$

where v_i and v_o are the surface speeds of the inner and outer cylinders, respectively. Since the fluid only fills a small region at the bottom between the cylinders, we have neglected the z components of v_i and v_o. Therefore

$$u(y,z) = v_o + \frac{v_i - v_o}{b(y)}\left(z - b_1(y)\right) + \frac{1}{2\mu}\frac{dp}{dy}\left(z - b_1(y)\right)\left(z - b_2(y)\right), \tag{2.5}$$

where $b(y) = b_2(y) - b_1(y)$ is the width of the gap as shown in Fig. 1.1. If $y/r \ll 1$, where r is the radius of either of the cylinders, $b(y)$ is approximately

$$b(y) = b_0 + \frac{y^2}{2R}. \tag{2.6}$$

The fluid flux per unit length in the gap is then

$$Q = \int_{b_1(y)}^{b_2(y)} u(y,z)dz = \frac{v_i + v_o}{2} b(y) - \frac{b^3(y)}{12\mu}\frac{dp}{dy}, \tag{2.7}$$

or, solving for dp/dy,

$$\frac{dp}{dy} = \frac{12\mu}{b^2(y)}\left(V - \frac{Q}{b(y)}\right), \tag{2.8}$$

where

$$V = \frac{v_i + v_o}{2}. \tag{2.9}$$

We now introduce a mathematical variable θ such that $y = (2Rb_0)^{1/2}\tan\theta$, and $b(y) = b_0(1 + \tan^2\theta)$. Eq. (2.8) then becomes

$$\frac{dp}{d\theta} = 12\mu\sqrt{\frac{2R}{b_0^3}}\left(V\cos^2\theta - \frac{Q}{b_0}\cos^4\theta\right). \tag{2.10}$$

Integrating Eq. (2.10), we get

$$\begin{aligned} p(y,Q) - p_0 \;=\; & 6\mu V\sqrt{2R/b_0^3}\left[\left(\theta + \frac{\pi}{2}\right) + \frac{1}{2}\sin(2\theta)\right] \\ & -6\mu Q\sqrt{2R/b_0^5}\left[\frac{3}{4}\left(\theta + \frac{\pi}{2}\right) + \frac{1}{2}\sin(2\theta) + \frac{1}{16}\sin(4\theta)\right], \end{aligned} \tag{2.11}$$

where p_0 is the pressure at $y = -\infty$, which we take to be atmospheric pressure. If we neglect the influences of the meniscus and gravity, then taking $y = \infty$ and $p(\infty) = p_0$, we get, from Eq. (2.11),

$$Q = \frac{4}{3}b_0 V. \tag{2.12}$$

There is, however a pressure drop at the meniscus, due to surface tension, which is approximately equal to the static value, so

$$p(y_m) = p_0 - \sigma\left(\frac{2}{b_m} + \frac{1}{\rho}\right), \tag{2.13}$$

where y_m is the position of the tip of the meniscus, and $b_m = b(y_m)$. $1/\rho$ is the curvature of the meniscus in the horizontal plane, which is zero at a planar interface, and σ is the surface tension.

At the interface, the pressure given by Eq. (2.11) should equal that from Eq. (2.13), so we get:

$$\begin{aligned}\frac{\sigma}{6\mu V}\sqrt{\frac{2b_0}{R}} &= -\frac{1}{\cos^2\theta_m}\left[\left(\theta_m+\frac{\pi}{2}\right)+\frac{1}{2}\sin(2\theta_m)\right] \\ &+ \frac{1}{\cos^2\theta_m}\cdot\frac{Q}{b_0}\left[\frac{3}{4}\left(\theta_m+\frac{\pi}{2}\right)+\frac{1}{2}\sin(2\theta_m)+\frac{1}{16}\sin(4\theta_m)\right]. \quad (2.14)\end{aligned}$$

In the experiment, the term on the left hand side of Eq. (2.14) is very small, and in this case, the flux calculated from this equation is very close to $\frac{1}{3}b_0V$ as found in Eq. (2.12). This means that the effect of the meniscus on the flux is small.

By the conservation of flux of the fluid, the flux of fluid which enters the gap between the cylinders should be equal to that which exits from the gap, in the form of layers coated onto the cylinders. The thickness of the coating can be expressed as

$$d = b_m f(\frac{\mu v}{\sigma}), \quad (2.15)$$

where $f(Ca)$ is a function of the dimensionless capillary number $Ca = \mu v/\sigma$. By fitting experimental data obtained by Tabeling et al. [87] in a classical Saffman-Taylor experiment, Hakim et al. found $f(Ca)$ to be well approximated by

$$f(Ca) = 0.12[1 - \exp(-0.86Ca^{2/3})]. \quad (2.16)$$

Therefore, we can write the outgoing flux as

$$Q = v_i b_m f\left(\frac{\mu v_i}{\sigma}\right) + v_0 b_m f\left(\frac{\mu v_0}{\sigma}\right). \quad (2.17)$$

Eq. (2.14) together with Eq. (2.17) determines y_m and Q, and therefore the pressure field $p^{(0)}(y) = p(y)$ in the front of the planar interface.

Next, a small perturbation proportional to $\sin(kx)$ will be imposed on the interface, and its linear stability will be studied. The position $\xi(x)$ and the pressure field

$p(x, y)$ at the perturbed interface are now

$$\xi(x, t) = y_m + \epsilon(t) sin(kx), \tag{2.18}$$

$$p(x, y, t) = p^{(0)}(y) + \eta(t) q_k(y) \sin(kx), \tag{2.19}$$

where k is the wavenumber of the perturbation.

By Taylor expansion of Eqs. (2.19) and (2.13) about $y = y_m$ to the first order, we get

$$p(x, y) = p_m^{(0)} + \frac{dp^{(0)}}{dy_m} \epsilon(t) \sin(kx) + \eta(t) q_k(y_m) \sin(kx), \tag{2.20}$$

and

$$p(x, y) = \left(p_0 - \frac{2\sigma}{b_m}\right) + \frac{2\sigma}{b_m^2} \left(\frac{db}{dy}\right)_{y_m} \epsilon(t) \sin(kx) - \frac{\sigma}{\rho}, \tag{2.21}$$

respectively, where $p_0 - 2\sigma/b_m = p_m^{(0)}$ and the curvature of the perturbed interface is

$$\frac{1}{\rho} = \frac{[\epsilon(t) \sin(kx)]_{xx}}{\left[1 + [\epsilon(t) \sin(kx)]_x{}^2\right]^{\frac{3}{2}}} = -\epsilon(t) k^2 \sin(kx). \tag{2.22}$$

By equating the right-hand sides of Eqs. (2.20) and (2.21), we find that the relationship between $\epsilon(t)$ and $\eta(t)$ is

$$\eta(t) q_k(y_m) = \epsilon(t) \left[-\frac{dp^{(0)}}{dy_m} + \frac{2\sigma}{b_m^2} \left(\frac{db}{dy}\right)_{y_m} + \sigma k^2\right]. \tag{2.23}$$

The equation of motion for the boundary is given by the conservation of fluid at the interface:

$$b_m[\vec{u}.\vec{n}(\xi) - v_n] = b_m \left[f(Ca_i)(v_i - v_n) + f(Ca_o)(v_o - v_n)\right], \tag{2.24}$$

where $\vec{n}$ is the normal direction of the interface, and v_n is the velocity of the fluid interface in the y direction:

$$v_n = \frac{d\epsilon(t)}{dt} \sin(kx). \tag{2.25}$$

The left hand side of Eq. (2.24) describes the fluid going into the interface, and the right hand side, the fluid coming out of the interface. The velocity $\vec{u}$ is

$$\vec{u}(x,y) = \vec{V} - \frac{1}{12}\frac{b^2(y)}{\mu}\vec{\nabla}p, \tag{2.26}$$

and

$$\vec{u}\cdot\vec{n} = \vec{V}\cdot\vec{n} - \frac{1}{12}\frac{b^2(y)}{\mu}\frac{dp}{dn}. \tag{2.27}$$

Here $\vec{V} = (\vec{v}_i + \vec{v}_o)/2$.

Inserting Eqs. (2.25)-(2.27) in Eq. (2.21), we get

$$v_n\left[1 - f(Ca_i) - f(Ca_o)\right] = \vec{V}.\vec{n} - \frac{1}{12}\frac{b^2(\xi)}{\mu}\frac{dp}{dn} - \left[f(Ca_i)v_i + f(Ca_o)v_o\right], \tag{2.28}$$

where, by Taylor expansion,

$$b^2(\xi)\frac{dp}{dn} = b_m^2\frac{dp^{(0)}(y_m)}{dn} + \frac{d\left(b^2dp^{(0)}/dn\right)}{dy_m}\epsilon(t)\sin(kx) + b_m^2\eta(t)\frac{dq_k(y_m)}{dn}\sin(kx). \tag{2.29}$$

Since the gap thickness varies very slowly with y, we can take the approximations

$$\frac{dp^{(0)}(y_m)}{dn} \simeq \frac{dp^{(0)}(y_m)}{dy}, \tag{2.30}$$

$$\frac{dq_k(y_m)}{dn} \simeq \frac{dq_k(y_m)}{dy}. \tag{2.31}$$

Combined with Eq. (2.8), Eq. (2.29) becomes

$$b^2(\xi)\frac{dp}{dn} = b_m^2\frac{dp^{(0)}(y_m)}{dn} + \left[\frac{12\mu Qb'_m}{b_m^2} + b_m^2q'_k(y_m)\right]\eta(t)\sin(kx), \tag{2.32}$$

where $b'_m = db(y_m)/dy$, $q'_k(y_m) = dq_k(y_m)/dy$.

From Eqs. (2.23), (2.28), (2.32), the equation for $\epsilon(t)$ is

$$\begin{aligned}\frac{d\epsilon(t)}{dt}&\left[1 - f(Ca_i) - f(Ca_o)\right]\sin(kx) = \\ &-\epsilon(t)\left[\frac{Qb'_m}{b_m^2} + \frac{b_m^2q'_k(y_m)}{12\mu q_k(y_m)}\left(-\frac{dp_m^{(0)}}{dy} + \frac{2\sigma b'_m}{b_m^2} + \sigma k^2\right)\right]\sin(kx) \\ &+\left[\vec{V}\cdot\vec{n} - \frac{b_m^2}{12\mu}\frac{dp_m^{(0)}}{dn} - \left[f(Ca_i)v_i + f(Ca_o)v_o\right]\right].\end{aligned} \tag{2.33}$$

The last term on the right-hand side of Eq. (2.33) is equal to zero for the straight interface. If we now assume that $\epsilon(t) \sim e^{\beta t}$, then from Eq. (2.33) the growth rate β is

$$\beta = -\frac{1}{1 - f(Ca_i) - f(Ca_o)} \cdot \left[\frac{Qb'_m}{b_m^2} + \frac{b_m^2 q'_k(y_m)}{12\mu q_k(y_m)} \left(\frac{2\sigma b'_m}{b_m^2} + \sigma k^2 - \frac{dp_m^{(0)}}{dy} \right) \right]. \quad (2.34)$$

When β is positive, the perturbation will grow, so the base state is unstable. The bifurcation happens at $\beta = 0$.

To calculate β, we need to know $q_k(y_m)$. The incompressibility of the fluid requires that

$$\vec{\nabla} \cdot [b(y)u(y)] = 0, \quad (2.35)$$

and from this, we have

$$\frac{d^2 q_k}{dy^2} + \frac{3}{b}\frac{db}{dy}\frac{dq_k}{dy} - k^2 q_k = 0. \quad (2.36)$$

We also require that q_k goes to zero when $y \to -\infty$. For simplicity, we assume that $(db/dy)/b(y)$ is a constant:

$$\frac{1}{h} = \frac{3}{2b}\left(\frac{db}{dy}\right)_{y=y_m}. \quad (2.37)$$

Then Eq. (2.36) can be solved for q_k. The solution is of the form

$$q_k \sim \exp\left(\frac{y}{h}\left(\sqrt{1 + h^2 k^2} - 1\right)\right). \quad (2.38)$$

Using this, the expression for the growth rate, Eq.(2.34), is now

$$\beta = -\frac{1}{1 - f(Ca_i) - f(Ca_o)} \cdot \left[\frac{Qb'_m}{b_m^2} + \frac{b_m^2}{12\mu}\frac{\sigma}{h}\left(\sqrt{1 + h^2 k^2} - 1\right)\left(\frac{2b'_m}{b_m^2} + k^2 - \frac{12}{b_m^2}\left(Ca - \frac{\mu Q}{\sigma b_m} \right) \right) \right]. \quad (2.39)$$

The relevant physical length scale is R in our system. Actually, if we scale the length variables in Eq. (2.39) by R and scale β by $\sigma/\mu R$, and Q by $R\sigma/\mu$, this equation will remain unchanged except that the variables will now be dimensionless. Thus,

in the following calculations and graphs, we will use dimensionless length variables which have been scaled by R, and the dimensionless capillary number $Ca = \mu v/\sigma$.

The planar interface loses stability when the growth rate $\beta = 0$. For a given gap thickness b_0/R and capillary numbers Ca_i and Ca_o, we can calculate b_m/R and $Q\mu/R\sigma$ by using Eqs. (2.14) and (2.17). Thus we can numerically determine the stability boundary by setting Eq. (2.39) equal to zero. Fig. 2.1 is a plot of the stability boundary calculated for $b_0/R = 0.0024$. The infinite, straight meniscus is stable for values of Ca lying below the plotted curve, and unstable to the formation of sinusoidal fingers above. Beyond the high-wavelength end of the curve plotted, solutions of Eq. (2.39) with $\beta = 0$ could not be found for real k. We would expect the straight interface to become unstable when Ca is increased above the stability boundary plotted in Fig. 2.1. This occurs first at the minimum of the plotted curve, at a wave length λ_c. However, Fig. 2.1 has two local minima — one at the high-wavelength end of the curve, and one at a wavelength $\lambda/R \simeq 0.3$. The high-wavelength behaviour of our stability boundary is unusual and unexpected. It has not been found in other analyses of this type of instability [63, 64], even that of Hakim et al., whose equations we used [73]. Furthermore, our experimental results are most consistent with the short-wavelength instability. While we have no reason to doubt the results of our numerical solution of Eqs. (2.14), (2.17) and (2.39), it seems that the high-wavelength portion of the stability boundary is for some reason not relevant to the physical situation. This will be shown further in Chapter 4.

Recently, Reinelt [70] has taken into account the effects of both the left and the right oil-air interfaces, as shown in Fig. 1.1, on the stability of the meniscus, and has calculated a stability boundary similar to that shown in the phase diagram Fig. 1.3.

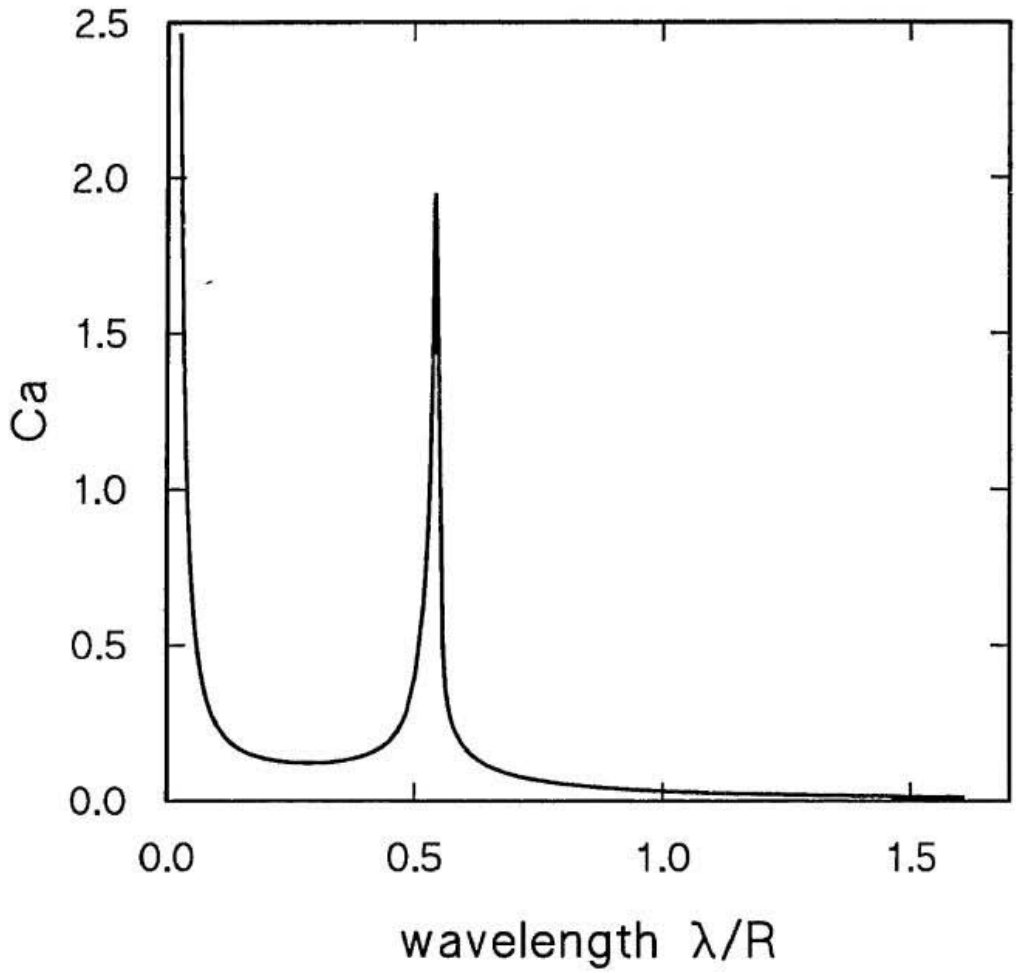

Figure 2.1: Calculated linear stability boundary of the straight meniscus, at a dimensionless gap thickness $b_0/R = 0.0024$. Note the two minima. The stability corresponding to the minimum at larger wavelength occurs at a lower value of Ca and so should in principle be the one observed in an ideal experiment, but the experimental results are in better accord with the shorter wavelength instability.

2.2 Parity breaking

In our experimental system, the stationary fingering patterns observed when only one cylinder rotates undergo a parity-breaking transition when the cylinders begin to counter-rotate. At this transition, the fingers of the pattern lose their reflection symmetry and start to drift. It is impossible, at this stage, to investigate the properties of this traveling-pattern state by solving the Navier-stokes equations. To avoid this mathematically knotty problem, however, we can study the dynamical behaviour of the broken-parity state by considering the symmetry of the pattern. There have been two theoretical approaches to this problem, both of which predict that the breaking of parity symmetry of a pattern leads to a traveling-wave state. One of these theories, introduced by Coullet and co-workers [25-27], is based on coupled amplitude and phase equations developed from very general symmetry arguments. The other, which involves the resonant coupling of spatial modes with wavenumbers q and $2q$, was first investigated theoretically by Malomed and Tribelskey [28], and since then by many other groups [29-35,37-40]. In this section we introduce some of the results of the two theories which are related to our experiments. More detail can be found in Refs. [25-27,35].

2.2.1 Symmetry argument

Following Refs. [25-27], the pattern at the oil-air interface in our experimental system, $U(x,t)$, can always be written as a sum of parity-symmetric (S) and anti-symmetric (A) components:

$$U(x,t) = S(x,t)U_S\left(x+\phi(x,t)\right) + A(x,t)U_A\left(x+\phi(x,t)\right), \qquad (2.40)$$

where S and A are the amplitudes of the symmetric and antisymmetric parts of the pattern, respectively, and ϕ is a phase variable. U_S and U_A are even and odd

functions of their arguments, respectively, i.e.,

$$U_S(x) = U_S(-x) \tag{2.41}$$

$$U_A(x) = -U_A(-x). \tag{2.42}$$

If $A = 0$ the pattern has parity symmetry; A can be taken to be the order parameter of the broken-parity state. The phase variable ϕ gives the phase of the pattern relative to that of the underlying symmetric pattern. A nonzero value of ϕ_t corresponds to a moving pattern, while $\phi_x = (q - q_0)/q_0$ is the relative difference in wave number between the asymmetric state, with wavenumber q, and the underlying symmetric pattern, which has wavenumber q_0. S, A and ϕ are assumed to be slowly varying real functions of space and time.

To describe the dynamics of the broken-parity pattern, equations of motion are required for both A and ϕ, which may be deduced from the invariance of the dynamics seen by observers on opposite sides of the pattern. Assuming that the coordinates of the two observers are x and $\bar{x}$, then $\bar{x} = -x$, and $\bar{\phi}(-x) = -\phi(x)$. Since the amplitude of the pattern seen by both viewers is the same, taking into account the antisymmetry of U_A, we require $\overline{A}(-x) = -A(x)$. The equations of motion which satisfy these symmetries and are invariant with respect to the transformation $\phi \to \phi +$ const are, to the lowest order,

$$A_t = A_{xx} + \mu A - A^3 + \epsilon \phi_x A + \cdots, \tag{2.43}$$

$$\phi_t = \phi_{xx} + \omega A + \cdots, \tag{2.44}$$

where ω and ϵ are coupling constants, and μ (not viscosity!) is the control parameter; the bifurcation occurs at $\mu = 0$. Here we have assumed a supercritical bifurcation to the broken-parity state, in accordance with our experimental results. If a subcritical bifurcation is assumed, a term proportional to A^5 should be included in Eq. (2.43)

and the sign of the A^3 term should be reversed. Other terms involving higher derivatives of A and ϕ are allowed by symmetry, but were not included in the discussion of Ref. [25].

For a spatially uniform pattern, the steady solutions of Eq. (2.13) are given by

$$(\mu + c\phi_x)A - A^3 = 0, \tag{2.45}$$

which has nontrivial solutions

$$A = \pm(\mu + c\phi_x)^{1/2}. \tag{2.46}$$

Eq. (2.44) then gives

$$\phi_t = v_\phi = \omega A, \tag{2.47}$$

where v_ϕ is the phase velocity of the drifting pattern. Parity-breaking states exist when $A \neq 0$, and the different signs of A correspond to two degenerate states which travel in opposite directions. From Eqs (2.46) and (2.47), we expect the square of the asymmetry of the pattern to grow linearly with the control parameter μ, and the phase speed to be proportional to the asymmetry.

2.2.2 $q - 2q$ mode coupling

A more specific model of parity breaking involves the resonant coupling of spatial modes with wavenumber q and $2q$. According to Ref. [35], a pattern $U(x,t)$ involving two modes of wavenumber q and $2q$ can be written as

$$U(x,t) = \left[C(x,t)e^{iqx} + c.c.\right] + \left[D(x,t)e^{2iqx} + c.c.\right] + \cdots. \tag{2.48}$$

Here C and D are the amplitudes of the two modes, and $c.c.$ indicates the complex conjugate. If we assume that the pattern is spatially uniform, then C and D are independent of x. Then, one can write down a set of coupled equations for the

dynamics of the amplitudes of the two modes. These equations, to third order, are of the form

$$C_t = \mu C - C^* D - \alpha|C|^2 C - \beta|D|^2 C, \tag{2.49}$$

$$D_t = \nu D + C^2 - \gamma|C|^2 D - \delta|D|^2 D, \tag{2.50}$$

which describe a resonant interaction of the two modes. The coefficients $\alpha, \beta, \gamma, \delta$ are positive to ensure the stability of the solutions, that is, C_t and D_t should go to zero when C and D increase up to certain values. We assume $\nu < 0$, so that only the planar interface is stable when $\mu < 0$. In this case the $2q$ mode is linearly damped. The signs of the quadratic terms have been chosen such that the parity-breaking instability exists.

Writing

$$C = Re^{i\phi}, \quad D = Se^{i\theta}, \quad \Sigma = 2\phi - \theta, \tag{2.51}$$

we get from Eqs. (2.49) and (2.50)

$$R_t = (\mu - \alpha R^2 - \beta S^2)R - RS\cos\Sigma, \tag{2.52}$$

$$S_t = (\nu - \gamma R^2 - \delta S^2)S + R^2\cos\Sigma, \tag{2.53}$$

$$\Sigma_t = \left(2S - R^2/S\right)\sin\Sigma, \tag{2.54}$$

$$\phi_t = S\sin\Sigma. \tag{2.55}$$

When μ becomes positive, the stable state bifurcates to a stationary pattern with $R \neq 0$, $S \neq 0$, $\Sigma = 0$, and ϕ arbitrary. When μ is increased, this stationary state loses stability, via a supercritical bifurcation, to a state drifting with constant speed, corresponding to

$$R_t = 0, \quad S_t = 0, \quad \Sigma_t = 0, \quad \phi_t = \text{constant} \neq 0, \tag{2.56}$$

which implies $2S - R^2/S = 0$. This can occur as long as ν is not too negative, i.e., as long as the second harmonic is not too strongly damped. The order parameter

of this parity breaking is the phase mismatch Σ. As long as $\Sigma \neq 0$, the pattern will drift with a velocity

$$v_\phi = \phi_t/q = \frac{S}{q}\sin\Sigma. \tag{2.57}$$

This $q - 2q$ model is in fact equivalent to the model of Coullet et al. described above, as long as the pattern involves only two spatial modes. This can be shown by assuming that the pattern is described by

$$\begin{aligned} U(x) &= a\cos[q_0(x+\phi_1)] + b\cos[2q_0(x+\phi_2)] \\ &= a\cos[q_0(x+\phi_1)] + b\cos[2q_0(\phi_1-\phi_2)]\cos[2q_0(x+\phi_1)] \\ &\quad + b\sin[2q_0(\phi_1-\phi_2)]\sin[2q_0(x+\phi_1)]. \end{aligned} \tag{2.58}$$

The first two terms of the right-hand side of Eq. (2.58) are symmetric, while the third term is asymmetric. In this case the phase mismatch is $\Sigma = \phi_1 - \phi_2$, and the asymmetry order parameter of Eq. (2.40) is $A = b\sin 2q_0\Sigma$, so Eq. (2.47) is equivalent to Eq. (2.57) when only modes q_0 and $2q_0$ exist in the pattern.

2.3 Instabilities of the traveling-wave state

In our experimental system, the broken-parity traveling waves are observed to be stable only inside a wavelength band. Also, the traveling state is chaotic when the control parameter, which is the inner cylinder rotation speed in the experiments, is very low. In this section we look at the instability of the traveling wave using the complex Ginzburg-Landau equation, which predicts an Eckhaus instability for traveling waves. The details of this analysis can be found in Ref. [52]. We then investigate the instability of the traveling wave by studying the asymmetry equations (2.43) and (2.44). This leads to a prediction that the traveling state is disordered at low experimental control parameter, in agreement with the results of Fauve et al. [35].

2.3.1 Results from complex Ginzburg-Landau equation

Here we present a qualitative theoretical explanation for the long-wavelength modulational instability of the traveling waves, which is analogous to the Eckhaus instability for stationary patterns. A detailed theoretical analysis can be found in Ref. [52].

A complex Ginzburg-Landau equation (CGLE) up to the third order can be used to describe a system which exhibits a supercritical bifurcation to a traveling-wave state:

$$A_t = \epsilon A + (b_1 + ic_1)A_{xx} - (b_3 - ic_3)|A|^2 A. \tag{2.59}$$

Here A is the amplitude of a complex field, and ϵ the control parameter, where the bifurcation is at $\epsilon = 0$. c_1 and c_3 are associated with dispersion effects and nonlinear frequency renormalization, and b_1 and b_3 correspond to diffusion effects ($b_1 > 0$) and to nonlinear stability ($b_3 > 0$). By appropriately scaling time and space, b_1 and b_3 can be set to one. Thus

$$A_t = \epsilon A + (1 + ic_1)A_{xx} - (1 - ic_3)|A|^2 A. \tag{2.60}$$

Let

$$A(x,t) = a(x,t)e^{i\phi(x,t)}. \tag{2.61}$$

Substituting Eq. (2.61) into Eq. (2.60), we find that the amplitude a and phase ϕ satisfy the following equations:

$$a_t = \epsilon a + a_{xx} - a\phi_x^2 - 2c_1 a_x \phi_x - c_1 \phi_{xx} a - a^3, \tag{2.62}$$

$$\phi_t = 2a^{-1}a_x\phi_x + \phi_{xx} + c_1 a^{-1}a_{xx} - c_1\phi_x^2 + c_3 a^2. \tag{2.63}$$

Traveling-wave solutions can be easily found by setting

$$A = a_0 e^{i(qx - \omega t)}. \tag{2.64}$$

i.e., setting $a = a_0$ and $\phi = qx - \omega t$, and using Eqs. (2.62) and (2.63). This yields

$$a_0^2 = \epsilon - q^2, \tag{2.65}$$

$$\omega = -c_3\epsilon + (c_1 + c_3)q^2. \tag{2.66}$$

Since a_0^2 must be positive, the wavenumber of the drifting pattern must be in the band defined by

$$q^2 < \epsilon, \tag{2.67}$$

as shown in Fig. 2.2. The linear stability of the plane-wave state described in Eq. (2.64) can be studied by the standard linear analysis approach. Let

$$A = (a_0 + \tilde{a})e^{i(qx - \omega t + \tilde{\phi})}, \tag{2.68}$$

where the small perturbation $\tilde{a}$ and $\tilde{\phi}$ have the form

$$\tilde{a} = a_1 e^{iQx + \lambda t}, \tag{2.69}$$

$$\tilde{\phi} = \phi_1 e^{iQx + \lambda t}. \tag{2.70}$$

Substituting Eq.(2.68) into Eqs. (2.62) and (2.63), we get

$$(\lambda - \epsilon + Q^2 + q^2 + 3a_0^2 + i2c_1Qq)a_1 - (c_1a_0Q^2 - i2qQa_0)\phi_1 = 0, \tag{2.71}$$

$$(2c_3a_0^2 - c_1Q^2 - i2qQ)a_0^{-1}a_1 - (\lambda + Q^2 + i2qQc_1)\phi_1 = 0. \tag{2.72}$$

Solving Eqs. (2.71) and (2.72) for λ gives the characteristic equation

$$\tilde{\lambda}^2 + \tilde{\lambda}\beta + \gamma = 0, \tag{2.73}$$

with

$$\tilde{\lambda} = \lambda + 2iqQc_1, \tag{2.74}$$

$$\beta = 2Q^2 + 2a_0^2, \tag{2.75}$$

$$\gamma = Q^2(Q^2 + 2a_0^2) + (c_1Q^2 - i2qQ)^2 - 2a_0^2c_3(c_1Q^2 - i2qQ). \tag{2.76}$$

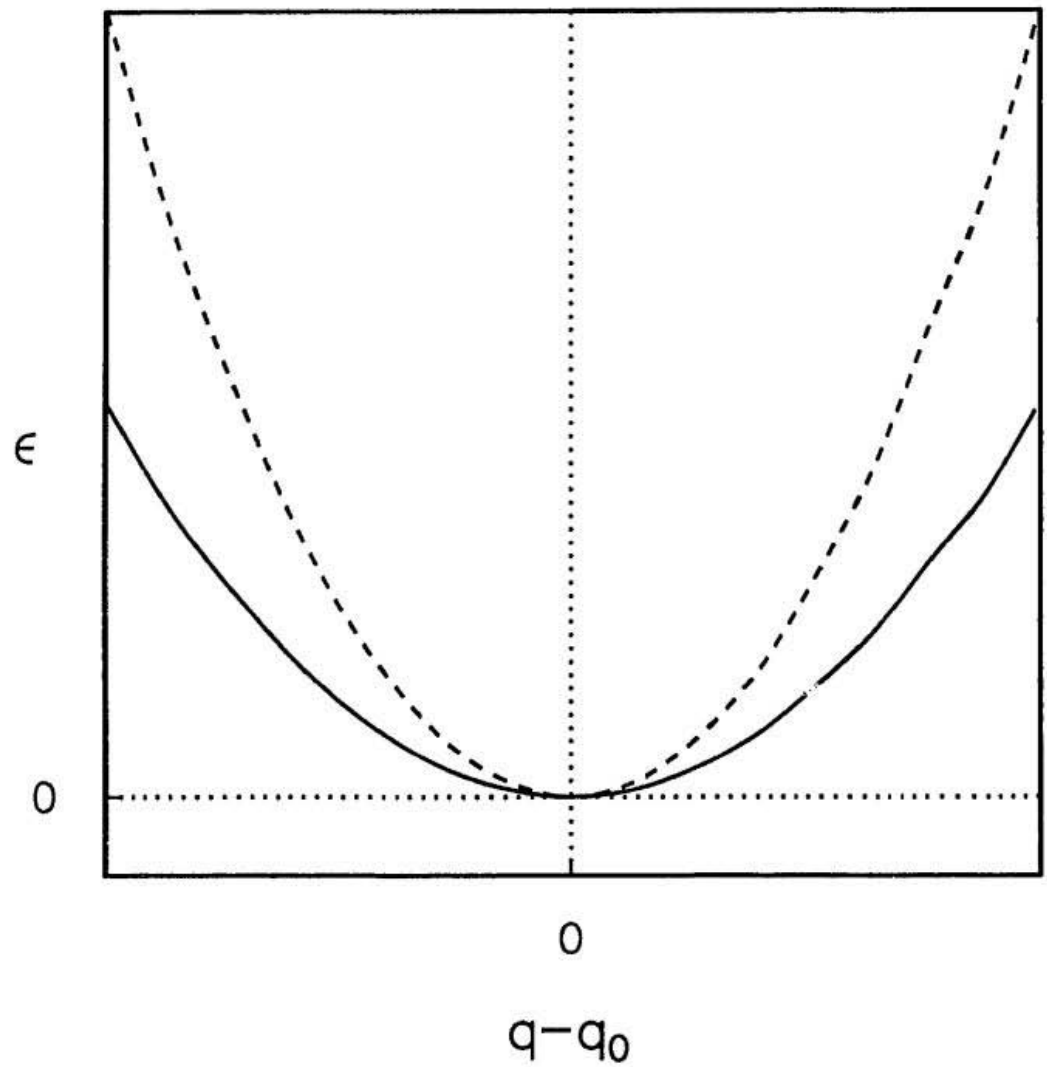

Figure 2.2: Stability diagram of traveling-wave state for the Ginzburg-Landau equation. A traveling-wave state exists above the solid curve, but is only stable above the dashed line. The traveling wave is subject to the Eckhaus instability in the range between the two curves.

The solution to Eq. (2.73) is

$$\tilde{\lambda} = -\frac{\beta}{2} \pm \frac{\beta}{2}\sqrt{1 - \frac{4\gamma}{\beta^2}}. \tag{2.77}$$

The requirement for stability is $\lambda < 0$. For long-wavelength modulation ($Q \to 0$), $\gamma \ll \beta^2$. Then, expanding (2.77) to order Q^4, we get the stability equation

$$\mathrm{Re}\left[\gamma/\beta + \gamma^2/\beta^3\right] > 0. \tag{2.78}$$

Substituting Eqs. (2.75) and (2.76) into Eq. (2.78), we get

$$a_0^2(1 - c_1c_3) - 2q^2 - 2q^2c_3^2 > 0. \tag{2.79}$$

From Eqs. (2.79) and (2.65), we find that the traveling wave is stable in the wavenumber band:

$$q^2 < \epsilon\frac{1 - c_1c_3}{2(1 + c_3^2) + (1 - c_1c_3)}. \tag{2.80}$$

Thus a necessary condition for stability is

$$1 - c_1c_3 > 0. \tag{2.81}$$

From Eq. (2.80), we see that the stable traveling wave exists in a narrower wavenumber band than the allowed traveling-wave band given by Eq. (2.67). A long-wavelength modulation instability of the traveling wave state occurs in the range

$$\epsilon\frac{1 - c_1c_3}{2(1 + c_3^2) + (1 - c_1c_3)} < q^2 < \epsilon, \tag{2.82}$$

as shown in Fig. 2.2. This result is very similar to that describing the Eckhaus instability [43] in the time-independent case. In that case, a stationary periodic pattern of wave number q exists when $q^2 < \epsilon$ (in normalized units), but is only stable against long-wavelength modulation in a narrower wavenumber band, $q^2 < \frac{1}{3}\epsilon$. The stationary periodic pattern is subject to the Eckhaus instability in the wavenumber band, $\frac{\epsilon}{3} < q^2 < \epsilon$.

2.3.2 Results from asymmetry equations

In this section, I will investigate the stability of the spatially uniform traveling-wave state using the asymmetry equations (2.43) and (2.44):

$$A_t = A_{xx} + \mu A - A^3 + \epsilon \phi_x A \tag{2.83}$$

$$\phi_t = \phi_{xx} + \omega A, \tag{2.84}$$

where A represents the degree of asymmetry of the pattern as before.

Assume that the spatially uniform traveling state is given by

$$A = A_0, \quad \phi_x = (q - q_0)/q_0, \quad \phi_t = v_\phi, \tag{2.85}$$

with $A_{xx} = 0$ and $\phi_{xx} = 0$. Substituting Eq. (2.85) into Eqs. (2.83) and (2.84), we get

$$A_0^2 = \mu + \epsilon \frac{q - q_0}{q_0}, \tag{2.86}$$

$$\phi_t = \omega A_0. \tag{2.87}$$

Since $A_0^2 > 0$, the parity-breaking state exists when

$$\mu + \epsilon \frac{q - q_0}{q_0} > 0, \tag{2.88}$$

as shown in Fig. 2.3. We now add a small perturbation to this traveling wave. Let

$$A = A_0 + a_1 e^{iQx + \lambda t}, \tag{2.89}$$

$$\phi = \frac{q - q_0}{q_0} x + v_\phi t + \phi_1 e^{iQx + \lambda t}. \tag{2.90}$$

Substituting Eqs.(2.89) and (2.90) into Eqs. (2.83) and (2.84), and linearizing, we get

$$(\lambda + 2A_0^2 + Q^2) a_1 - i\epsilon Q A_0 \phi_1 = 0, \tag{2.91}$$

$$\omega a_1 - (\lambda + Q^2)\phi_1 = 0. \tag{2.92}$$

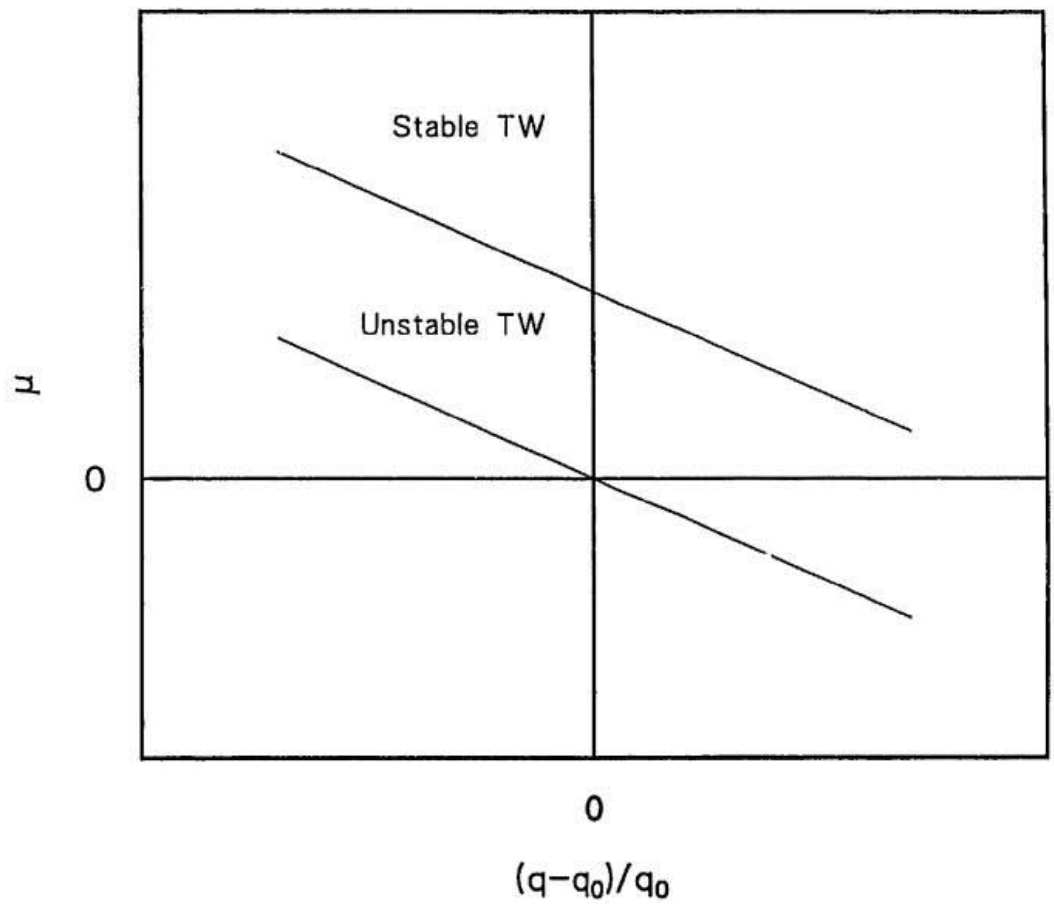

Figure 2.3: Linear stability diagram of the spatially-uniform traveling-wave state from the coupled amplitude and phase equations.

The characteristic equation for λ is

$$\lambda^2 + \lambda\beta + \gamma = 0, \tag{2.93}$$

with

$$\beta = 2(Q^2 + A_0^2), \tag{2.94}$$

$$\gamma = Q^2(2A_0^2 + Q^2) - i\omega\epsilon Q A_0. \tag{2.95}$$

For long-wavelength modulation, $Q \to 0$, $\gamma \ll \beta^2$. Thus, to order Q^4,

$$\lambda = -\frac{\beta}{2} \pm (\frac{\beta}{2} - \frac{\gamma}{\beta} - \frac{\gamma^2}{\beta^3}). \tag{2.96}$$

In this case λ is complex, so the requirement for stability is $\mathsf{Re}(\lambda) < 0$, that is,

$$\mathsf{Re}\left[\frac{\gamma}{\beta} + \frac{\gamma^2}{\beta^3}\right] > 0, \tag{2.97}$$

which gives

$$\mu + \epsilon\frac{q - q_0}{q_0} > \frac{|\epsilon\omega|}{2\sqrt{2}}. \tag{2.98}$$

In this case, there is a unstable traveling-wave band

$$0 < \mu + \epsilon\frac{q - q_0}{q_0} < \frac{|\epsilon\omega|}{2\sqrt{2}}, \tag{2.99}$$

as shown in Fig. 2.3. Thus the coupling terms in Eqs. (2.83) and (2.84) always destabilize the traveling state, regardless of the sign of the coupling constants ω and ϵ. This result agrees with the conclusion of Fauve et al. [35], derived from a more general version of equations (2.43) and (2.44). From Fig. 2.3, we find that, if $q \leq q_0$, as is the case in our experiment, the traveling wave is always unstable when μ is small. This is in agreement with our experiment results, as will be discussed below.

Chapter 3

Apparatus

The apparatus made for our experiments is illustrated schematically in Fig. 3.1. It was composed of two cylinders, with one mounted inside the other. The axes of the two cylinders were horizontal and parallel, but vertically offset, with the gap between the cylinders smallest at the bottom. A cross-section through the two cylinders is shown in Fig. 1.1. The outer cylinder, machined from a solid Plexiglas rod, rested on four bearing-mounted rollers. Plexiglas was used because its transparency allowed the pattern to be monitored with a video camera. Its inner radius was $r_2 = 66.7$ mm and its length was $l_2 = 210$ mm. The inner cylinder, made of white Delrin, was mounted on an axle and supported by bearings. Most of the experiments, including all of those involving the traveling-wave states, were performed using an inner cylinder with radius $r_1 = 50.4$ mm and length $l_1 = 202$ mm. Some of the results reported in Chapter 4 were obtained using an inner cylinder of the same length, but with a smaller radius, $r_1 = 24.85$ mm, in order to gauge the importance of boundary effects. A great deal of effort was spent to ensure that the cylinders were machined to high tolerance. Annular end caps on the outer cylinder confined the experimental fluid. In terms of the coordinate system defined in Fig. 3.1, the z positions of the ends of the inner cylinder could be independently adjusted with micrometer screws, as could the y position of each end of the outer cylinder. The x positions of both inner cylinder and outer cylinder were also adjustable. Two computer-controlled microstepping motors (Computer Plus, CPLX 57-120) were used to drive the rotation of the two cylinders independently, by means of belts

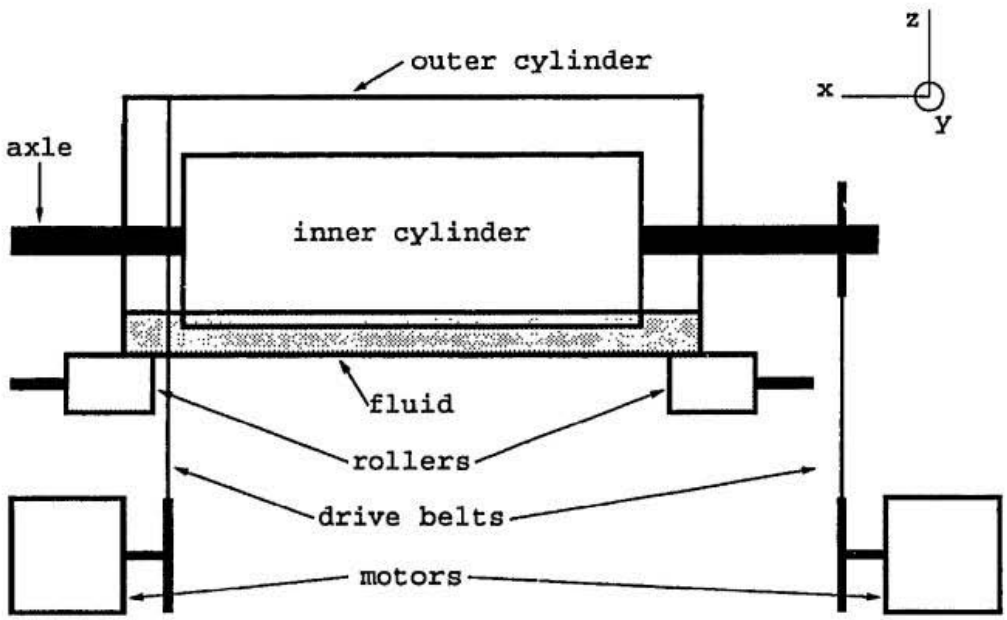

Figure 3.1: Schematic drawing of the experimental apparatus.

connected to a pulley on the axle of the inner cylinder and to a groove on the outer surface of the outer cylinder, as shown in Fig. 3.1. The speed of the motors was controlled from a program running on a 80286-based personal computer interfaced to the motors by an RS-232 serial line. The motors had a minimum increment in rotation frequency of 0.001 Hz, corresponding to a velocity increment of 0.08 mm/s for the inner cylinder with r_1 =50.4 mm, 0.04 mm/s for the inner cylinder with r_1 = 24.85 mm, and 0.04 mm/s for the outer cylinder.

The "nip" region at the bottom of the cylinders, where the gap between the cylinders is smallest, contained a small amount of silicone oil, just enough to keep this region filled. The width of this nip region is in the order of a centimeter in the y direction. The amount of oil used varied with the gap thickness. In the traveling-wave state (Chapter 5), the results of our measurements were independent of the oil volume. In the stationary fingering state (Chapter 4), the results around onset were slightly affected by the amount of oil, but as long as the oil volume was not too large, any volume dependence was small compared with the measurement error. Above onset, the results were independent of oil volume. Most experiments were done with an oil which we refer to as oil A (Aldrich Chemical Co., catalog no. 14,615-3), which had viscosity $\mu = 0.525$ g/cm s, surface tension $\sigma = 19.4$ g/s^2, and density $\rho = 0.963$ g/cm^3 at room temperature. A few runs in the stationary fingering state were done with a more viscous oil, oil B (Dow Corning 550), which had $\mu = 1.78$ g/cm s, $\sigma = 21.8$ g/s^2 and $\rho = 1.048$ g/cm^3. Both of these oils wet the surfaces of the cylinders. The fluid properties at room temperature are listed in Table 3.1.

The width of the gap between the two cylinders was set with the micrometer screws. We increased the gap from zero thickness, but there was an uncertainty in the location of this zero point of about ± 0.05 mm. The uniformity of the gap could

Table 3.1: Fluid properties

fluid	viscosity ($g.cm^{-1}.s^{-1}$)	surface tension ($g.s^{-2}$)	density ($g.cm^{-3}$)	kinematic viscosity ($cm^2.s^{-1}$)
silicone oil A	0.525	19.4	0.963	0.545
silicone oil B	1.78	21.8	1.048	1.70

be fine-tuned by visual inspection of the uniformity of the fingers at onset, which was very sensitive to the gap thickness. The parallelism of the cylinders was adjusted by inspection of the stability of the stationary fingers. If the cylinders were slightly out of alignment, the fingers did not remain stationary, but instead traveled along the length of the apparatus with very low speed.

Since the uniformity of the pattern near onset was very sensitive to the gap thickness, the uniformity of the cylinders was very important to our studies. A substantial amount of effort was put towards ensuring the uniformity of the cylinders. In our experiment, even when the cylinders were optimally aligned, we still observed a slight nonuniformity in the finger patterns, which was due to a nonuniformity of the gap width. From experimental measurements, we infer that the maximum variation in gap thickness was roughly 0.025 mm. Direct measurements indicated that the inside diameter of the outer cylinder was uniform to better than this, but the inner cylinder with radius $r_1 = 50.4$ mm, which was used for most of the experiments, was slightly hourglass-shaped by about the same amount. This caused the finger amplitude to be slightly smaller in the center of the pattern relative to the edges, even when the cylinders were as well aligned as possible. The effect of this nonuniformity could only be observed close to the onset of the stationary fingering state, when only one of the cylinders was rotating. The effect decreased with increasing thickness of the gap. This nonuniformity in the gap thickness did not seem to have

an influence on the behaviour of the broken-parity waves discussed in Chapter 5.

Fig. 3.2 is a block diagram of the experiment. The oil-air interface along the length of the apparatus was monitored with a CCD (charge coupled device) video camera (Pulnix, TM-7CN) and monitor (Burle, TC1910A), and data were recorded on a VCR (Panasonic, AG-1960) or stored on the personal computer using a video frame grabber (Imaging Technology, Inc., PCVISION plus) capable of grabbing 30 frames per second.

Images of the interface presented in this thesis have been contrast-enhanced, but are otherwise unprocessed. Measurements of the amplitude, wavelength, and traveling speed of the patterns were done directly from the video monitor, with an accuracy in the position measurements of plus or minus one pixel, corresponding to less than ± 0.3 mm when the bigger inner cylinder was used, and less then ± 0.1 mm when the smaller inner cylinder was used. The VCR we used could run the video tape frame by frame with time interval 1/60 s, and was used in this mode to measure the instantaneous speed of the traveling patterns. The average speed of the pattern can be measured from so-called space-time graphs, such as that in Fig. 5.2. Space-time graphs were obtained by periodically recording a single video line through the pattern. The individual line images were then combined to make a single two-dimensional image, in which the y-axis represented time and the x axis position. For quantitative analysis of the interface shape, the interface height as a function of x, the position along the length of the cylinder, was extracted from video images by having the computer automatically trace along the path of darkest pixels from a given starting point.

In our results we shall often scale lengths by the effective radius R as expressed in Eq. (2.1), which characterizes the rate of change of gap width in the y direction as shown in Fig. 1.1. For the inner cylinders with radii 50.4 mm and 24.8 mm, the

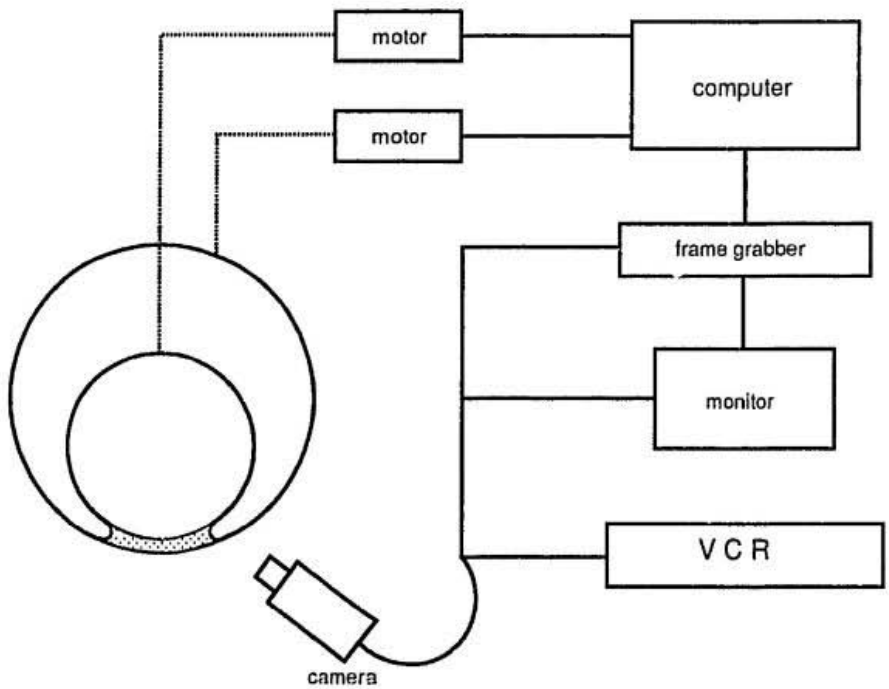

Figure 3.2: Block diagram of the experimental apparatus.

effective radii R are 206.8 mm and 39.96 mm, corresponding to $l_1/R = 0.98$ and 5.07, respectively. This means that for the first pair of cylinders, with $l_1/R = 0.98$, the system is actually rather short. As we will show, this shortness produced pronounced end effects, which altered the nature of the transition at the onset of the stationary pattern substantially compared with what would be expected for an infinite system.

Chapter 4

Experimental Results w.th One Cylinder Rotating

In this chapter, we describe the dynamical behaviour observed when only one of the cylinders rotates. The oil-air interface is a straight line at low cylinder rotation speeds. When the cylinder speed is increased to some critical value, the straight interface becomes unstable to a stationary fingering pattern. However, we find in our experiments that the nature of the transition from the straight interface to the stationary pattern state depends on which of the cylinders, inner or outer, is rotating, and also depends on the dimensionless length, l_1/R, of the cylinder. Here R is the effective radius of the apparatus defined in Eq. (2.1), and l_1 is the length of the inner cylinder. In section 4.1 we present experimental results obtained with an inner cylinder of radius $r_1 = 50.4$ mm. Results with the outer cylinder rotating are reported in section 4.1.1, and those with the inner cylinder rotating in section 4.1.2. Section 4.2 includes experimental results obtained when a smaller inner cylinder, with $r_1 = 24.85$ mm, was used. In section 4.3, we discuss our experimental results and compare them with theoretical calculations.

4.1 Experimental results with $r_1 = 50.4$ mm

In this section, we present the results of experiments done using a bigger inner cylinder with radius $r_1 = 50.4$ mm, for which the scaled length of the cylinder, l_1/R, is 0.98. The experimental results with the outer cylinder rotating are described in 4.1.1, and that with the inner cylinder rotating in 4.1.2. Experiments were done

using oil A if not specified.

4.1.1 Results with outer cylinder rotating

When the outer cylinder rotates with the inner cylinder fixed, the transition from straight interface to stationary pattern is always continuous, and no hysteresis was observed within the resolution of our experiment. Fig. 4.1 shows the development of the fingering pattern in this case. At low rotation rates, the oil-air interface was straight, as in Fig. 4.1(a). As Ca_o was increased, a low-amplitude ripple, sinusoidal in appearance, formed along the interface, as in Fig. 4.1(b) (Here $Ca_o = \mu v_o/\sigma$ is the outer cylinder capillary number). At onset the system accommodates approximately six fingers, with the wavelength independent of the layer thickness. Finite-size effects, consisting of a slight piling up of the fluid at each end of the apparatus, are visible in the figure. These end effects have a strong effect on the behaviour at the onset of the fingering pattern, especially in the case that the inner cylinder rotates, and will be discussed in detail below. The amplitude of the fingers (i.e., their length) grew rapidly as the rotation speed of the cylinder was increased just above onset (Fig. 4.1(c)), but then seemed to saturate at higher rotation rates. As the finger amplitude increased, the shape of the fingers changed. While they were roughly sinusoidal close to onset, at higher rotation rates the pattern consisted of narrow oil fingers separated by wider air spaces, as illustrated in Fig. 4.1(d). Fig. 4.2 is a plot of the finger amplitude as a function of capillary number, Ca_o, at two values of the gap thickness. The uncertainty in the amplitude is one unit. From our measurements, we find that the amplitude of the pattern for thinner layers is larger than that for thicker layers when the capillary number is well above onset.

As Ca_o is increased, the finger wavelength decreases and more fingers appear in the pattern. Fig. 4.3 is a plot of scaled pattern wavelength as function of capillary

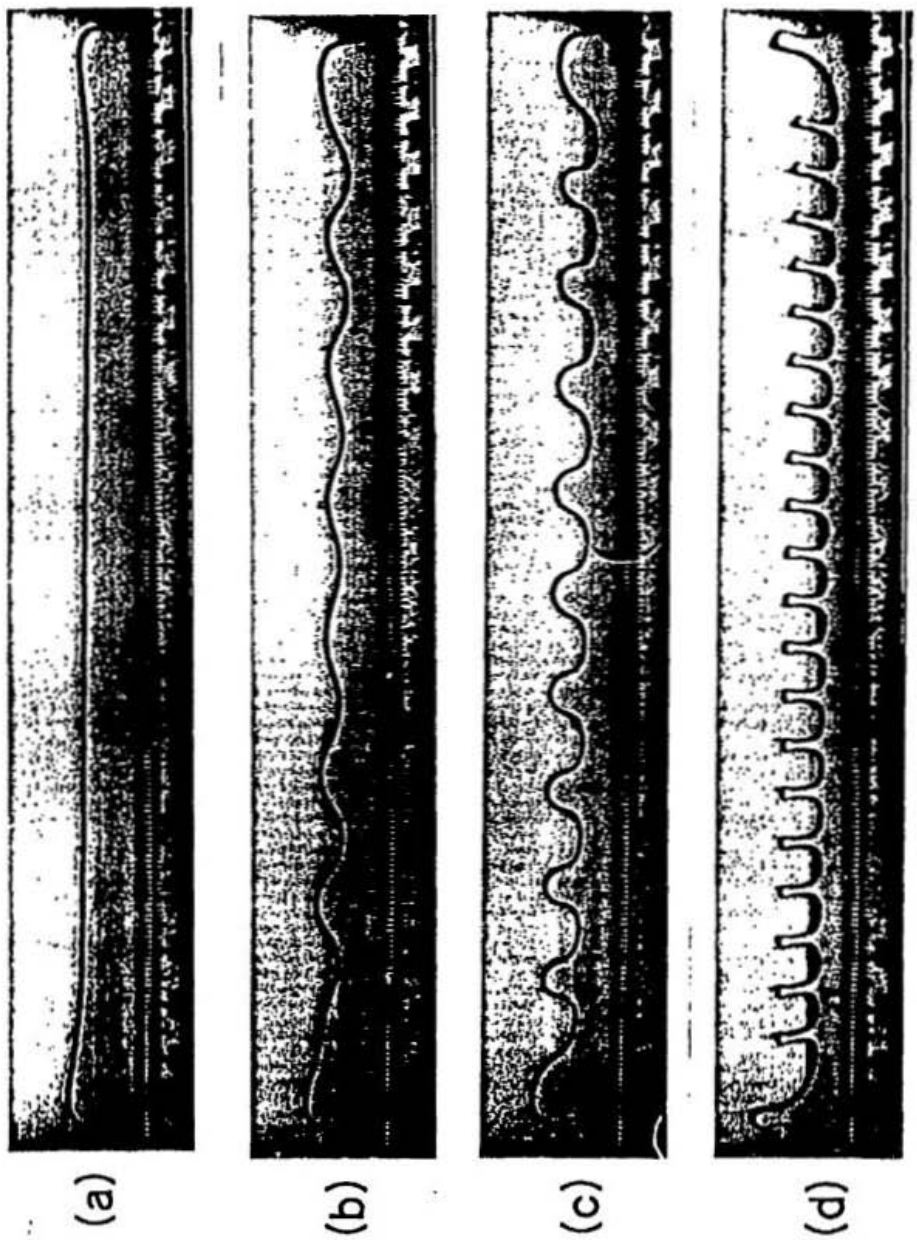

Figure 4.1: Development of the finger pattern formed when the inner cylinder is stationary while the outer one rotates. $b_0 = 0.5$ mm. (a) $Ca_o = 0.235$; (b) $Ca_o = 0.312$; (c) $Ca_o = 0.353$; (d) $Ca_o = 0.942$.

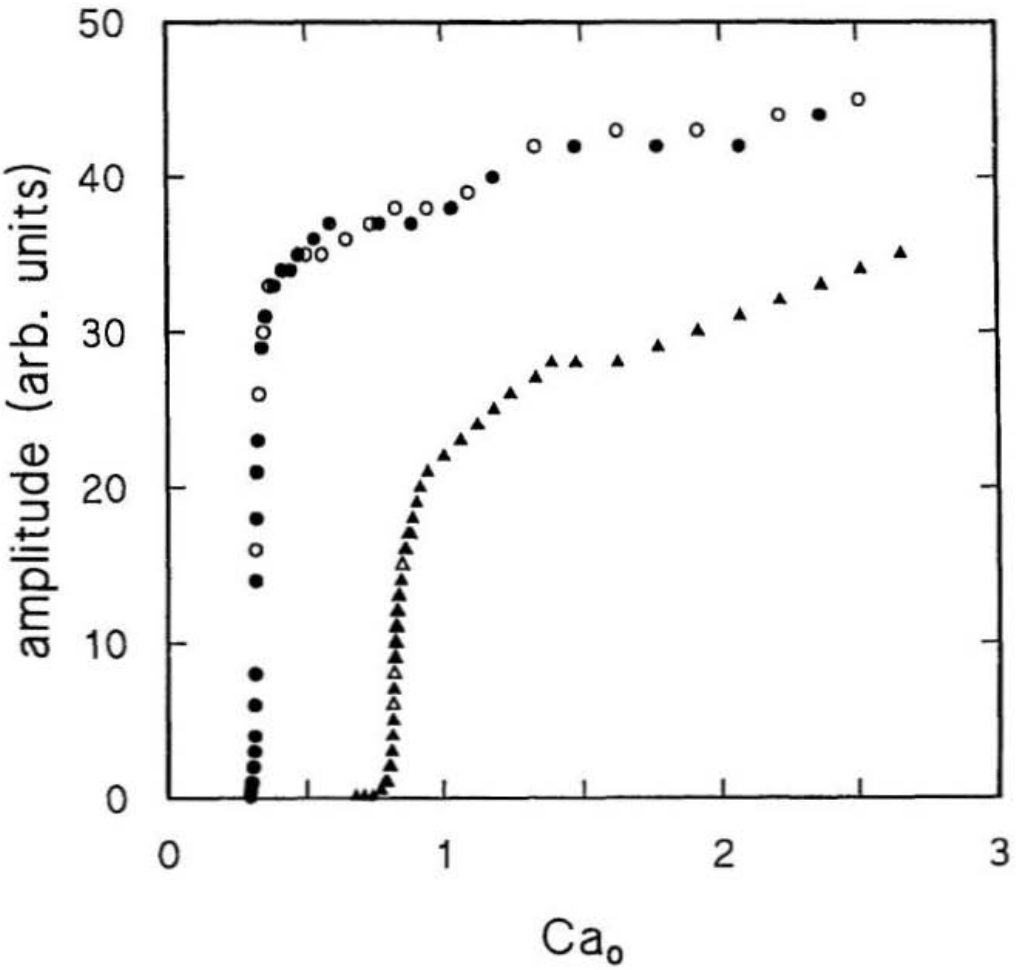

Figure 4.2: Finger amplitude as a function of capillary number, Ca_o, with the inner cylinder stationary. Open circles: $b_0 = 0.0024$, Ca_o increasing; solid circles: $b_0 = 0.0024$, Ca_o decreasing; open triangles: $b_0 = 0.0046$, Ca_o increasing; solid triangles: $b_0 = 0.0046$, Ca_o decreasing.

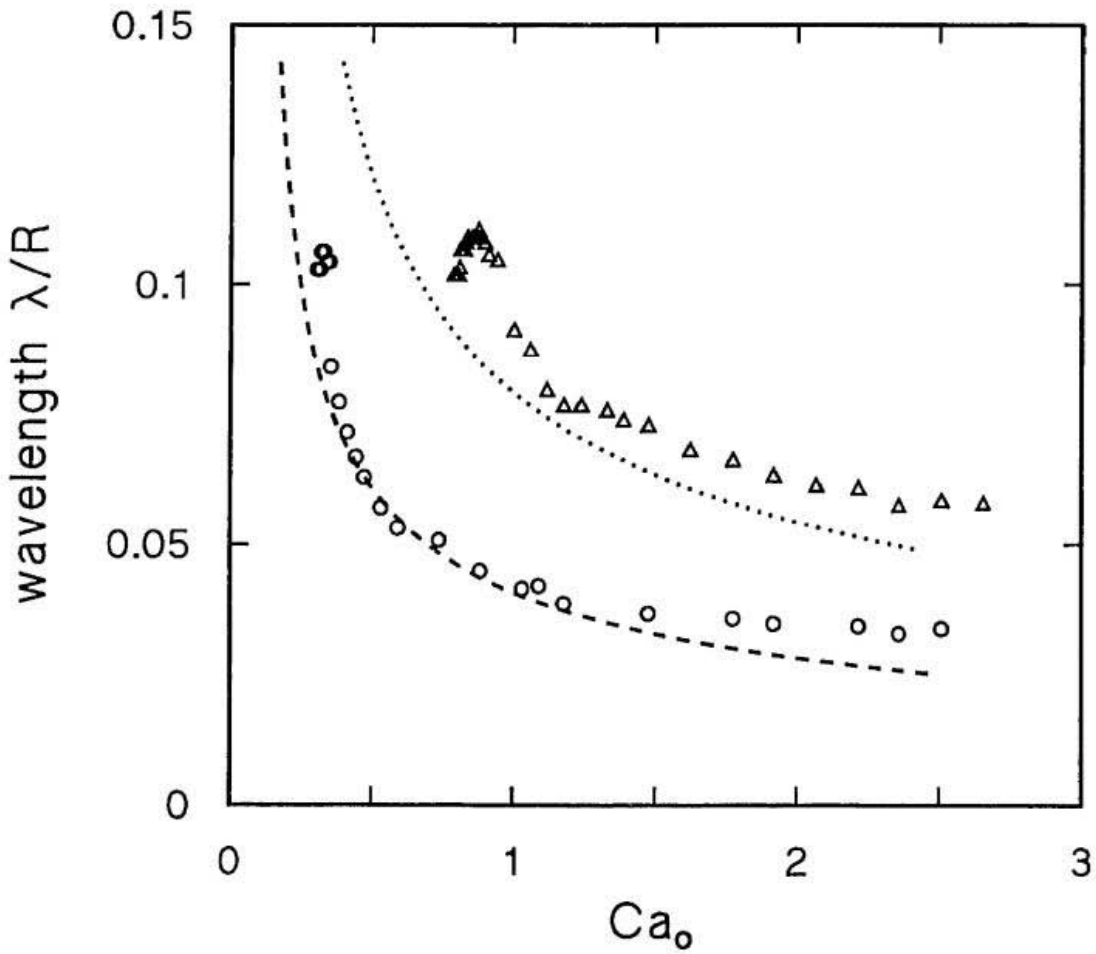

Figure 4.3: Pattern wavelength λ/R as a function of Ca_o, for the same two layer thicknesses as in Fig. 4.2. The curves are calculated linear stability boundaries. Circles: $b_0/R = 0.0024$; triangles: $b_0/R = 0.0046$.

number at the same two gap thickness as in Fig. 4.2. In this figure, part of the low-wavelength portion of the calculated linear stability boundary, shown in Fig. 2.1, is also plotted. The straight-interface state is stable on the low Ca_a side of the curves shown, and unstable on the high Ca_a side (although not shown here, the calculated stability boundary curves back to high Ca at long wavelength, as in Fig. 2.1). From Fig. 4.3, we see that the instability appears at values of Ca_a higher than the minimum of Ca_a on the theoretical curve, and at wavelengths shorter than that at that minimum. Close to the experimental onset the wavelength always increases slightly with Ca_a, then it decreases rather steeply before leveling out at higher rotation speeds. This initial increase in wavelength is in agreement with the experimental result of Cummins et al. [84], who suggested that it was caused by gravitational forces on the meniscus. Well above onset, the measured wavelengths follow very closely the wavelength at the calculated stability boundary, as also observed by Hakim et al. [73] and Michalland [14].

Up to two or three times the onset speed, the fingering pattern was stationary for relatively long periods of time — up to several hours. Further above onset, the pattern began to be perturbed by disturbances originating at the ends of the apparatus, which caused transient motion of the fingers near the boundaries to occur, and at speeds of order 10 times the onset speed the pattern was essentially disordered, with the finger amplitude varying in space and time, and the fingers moving continuously in a disordered fashion.

The data in Fig. 4.2 show some rounding close to onset. This we take to be due to imperfections in the experimental geometry, including both variations in gap thickness and the finite length of the cylinder. Above the rounded region, the growth of the finger amplitude is steep but continuous. If the transition were described by a Ginzburg-Landau equation, the amplitude would grow as $(Ca_a - Ca_c)^{1/2}$, where

Ca_c is the critical, or onset capillary number. However, fits of amplitude vs. Ca_o data to a simple power law of the form $A \sim (Ca_o - Ca_c)^x$, where A is the amplitude, gave exponents x in the range $0.1 - 0.25$, with the data for thinner layers in general giving the smaller exponents, and the data were not particularly well described by this functional form.

We also measured the capillary number Ca_c and the pattern wavelength at the onset of the fingering pattern for different gap widths. Here, Ca_c was defined as the capillary number at which the amplitude at the center of the pattern was two pixels on our video monitor. These results are shown as squares in Fig. 4.4 and Fig. 4.5. Fig. 4.4 is a plot of Ca_c vs. the scaled gap thickness b_0/R, and Fig. 4.5 is a plot of the scaled onset wavelength λ_c/R, vs. b_0/R. Also plotted in Figs. 4.4 and 4.5 are the onset capillary number and scaled wavelength for other experimental situations to be discussed below, and the result of linear stability analysis, shown as lines. From Fig. 4.4, we find that the onset capillary numbers in this case are close to the calculated ones only at very small gap width. Ca_c increases much faster with gap width than does the theoretical curve, the difference being about a factor of five for a gap width of 1 mm. In addition, the onset wavelengths are much lower than the theoretical predictions, as shown in Fig. 4.5. These features of our results can also be seen in Fig. 4.3.

4.1.2 Results with inner cylinder rotating

We now consider the case when the 50.4 mm radius inner cylinder rotates, with the outer cylinder fixed. The behaviour we observed is significantly different in this case from that described above, when the outer cylinder rotates with the inner cylinder fixed. In this case, a stationary pattern, traveling fingers and a disordered state were observed depending on the gap thickness and the inner cylinder capillary number,

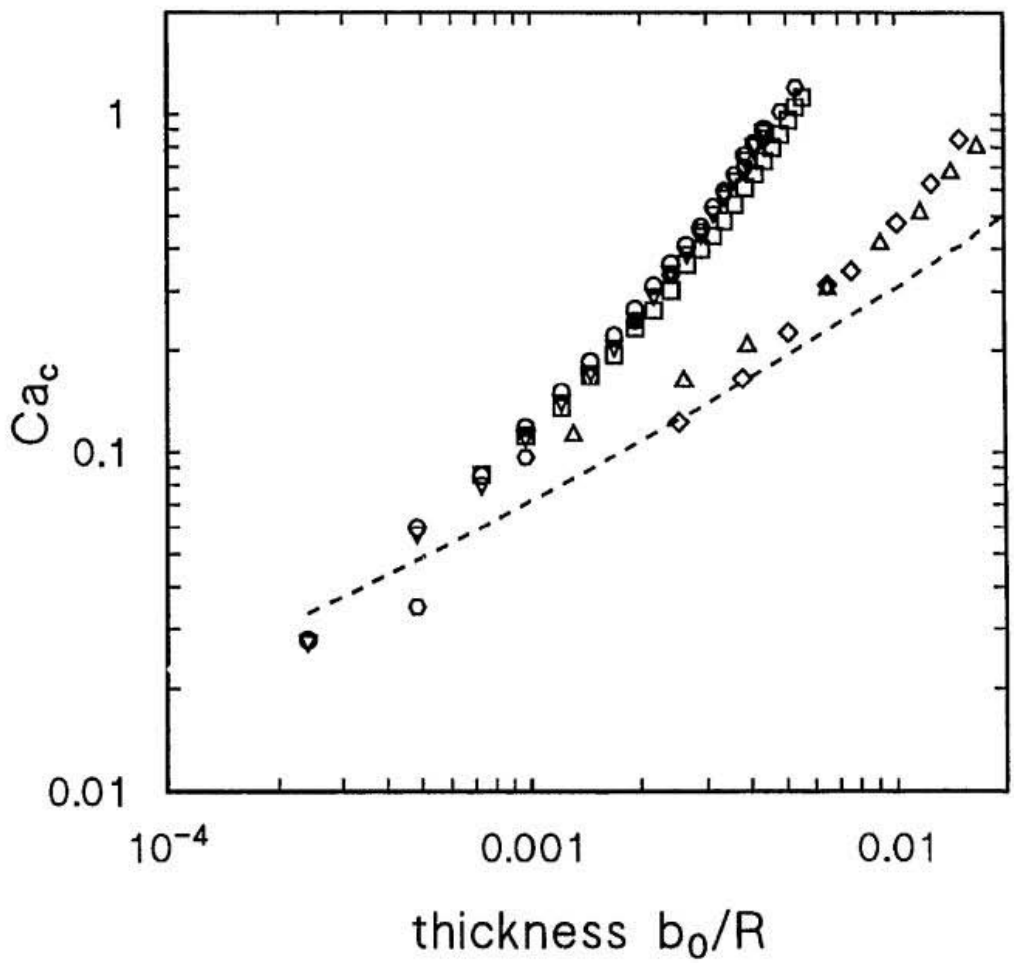

Figure 4.4: Onset capillary number Ca_c, as a function of the dimensionless gap thickness, b_0/R. Squares: outer cylinder rotating, bigger inner cylinder stationary, oil A; hexagons: bigger inner cylinder rotating, oil B; circles: bigger inner cylinder rotating, oil A, Ca_i increasing; upward-pointing triangles: bigger inner cylinder rotating, oil A, Ca_i decreasing; diamonds: outer cylinder rotating, oil A, small inner cylinder stationary; downward-pointing triangles: smaller inner cylinder rotating, oil A. The dashed line is the theoretical prediction discussed in the text.

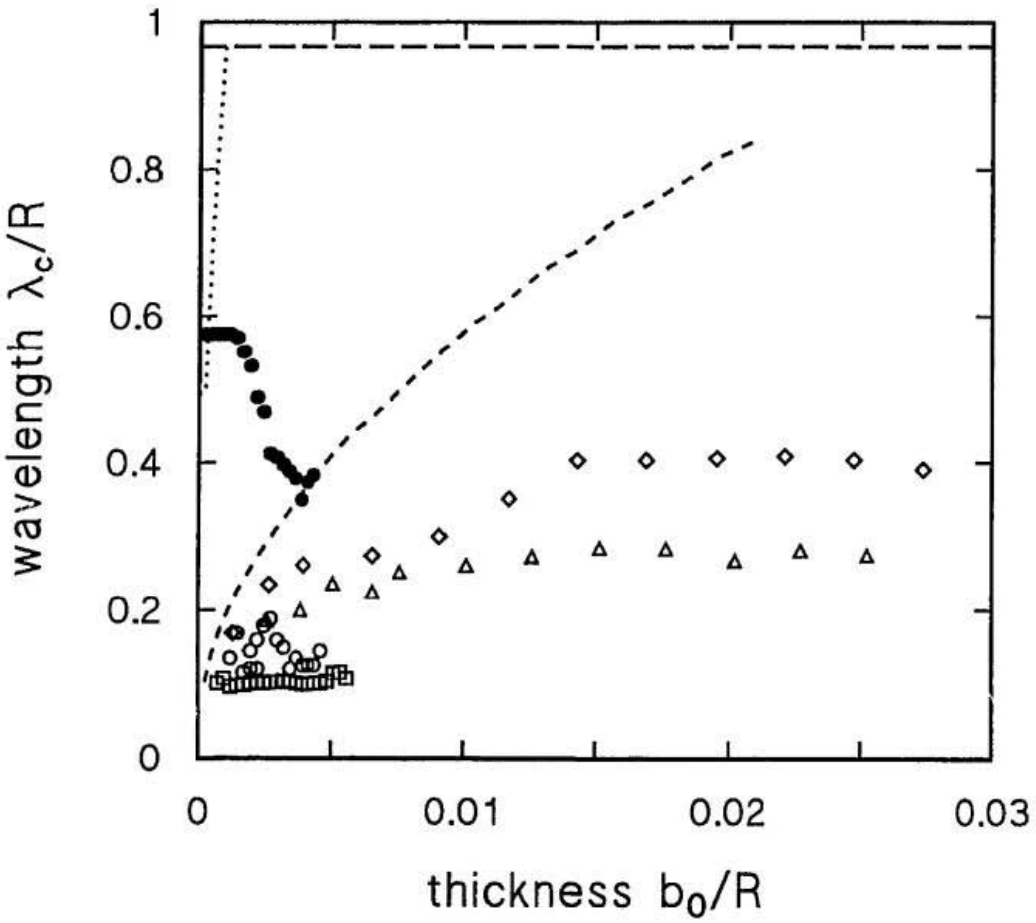

Figure 4.5: Dimensionless pattern wavelength at onset, λ_c/R, as a function of dimensionless gap thickness, b_0/R. Solid circles: "hole" separation at onset, bigger inner cylinder rotating; open circles: "ripple" wavelength, bigger inner cylinder rotating; squares: outer cylinder rotating, bigger inner one stationary; diamonds: outer cylinder rotating, smaller inner cylinder stationary; upward-pointing triangles: smaller inner cylinder rotating. The short-dashed and dotted lines are the theoretically predicted onset wavelengths for the short- and long-wavelength instabilities, as discussed in Chapter 2. The long-dashed line represents the length of the bigger inner cylinder. All experimental data are for oil A.

$Ca_i = \mu v_i/\sigma$. The observed behaviour is illustrated schematically in Fig. 4.6, which is the dynamical phase diagram for this bigger inner cylinder. As before, at very low values of the inner cylinder capillary number Ca_i, the oil-air interface was straight. As Ca_i increased, the fluid piled up near the ends of the cylinder, causing the meniscus to move forward there, and drop back in the center part of apparatus, as illustrated in Fig. 4.7(a). When the rotation speed was increased to a particular value, depressions or "holes" started to form at the points on the meniscus near each end where the curvature was greatest, as shown in Fig. 4.7(b). For thin oil layers ($b_0/R < 0.0034$) the amplitude of these holes grew continuously over a small range of rotation speed, then, at some critical value Ca_c, jumped discontinuously to a larger value, resulting in the pattern shown in Fig. 4.7(c). Typically the jump would occur at one end first, and at the other end at a very slightly higher rotation speed, but the initial jump could occur at either end of the appar .tus, and on occasion it happened at both ends essentially simultaneously. After this jump the hole amplitude again grew continuously for a small range of Ca_i, until a third hole suddenly formed near the middle of the gap, accompanied by another jump in amplitude. This process repeated as Ca_i was further increased (Fig. 4.7(d)), until there were approximately six holes (or five fingers) in the meniscus, after which time the further evolution of the the pattern was continuous within our experimental resolution. Close to onset, the pattern consisted of broad oil fingers separated by somewhat narrower air holes, as in Fig. 4.7(c) and (d). As v_i was increased, both the wavelength and the relative width of the oil fingers decreased (Fig. 4.7(e)). At higher speeds, the oil fingers were substantially narrower than the air regions, as when the outer cylinder rotated, but the amplitude in this case was significantly larger (Fig. 4.7(f)). On decreasing Ca_i, hysteresis and jumps in amplitude occurred associated with the disappearance of the last few fingers. Fig. 4.8 shows a narrow hysteresis loop close to onset, and the

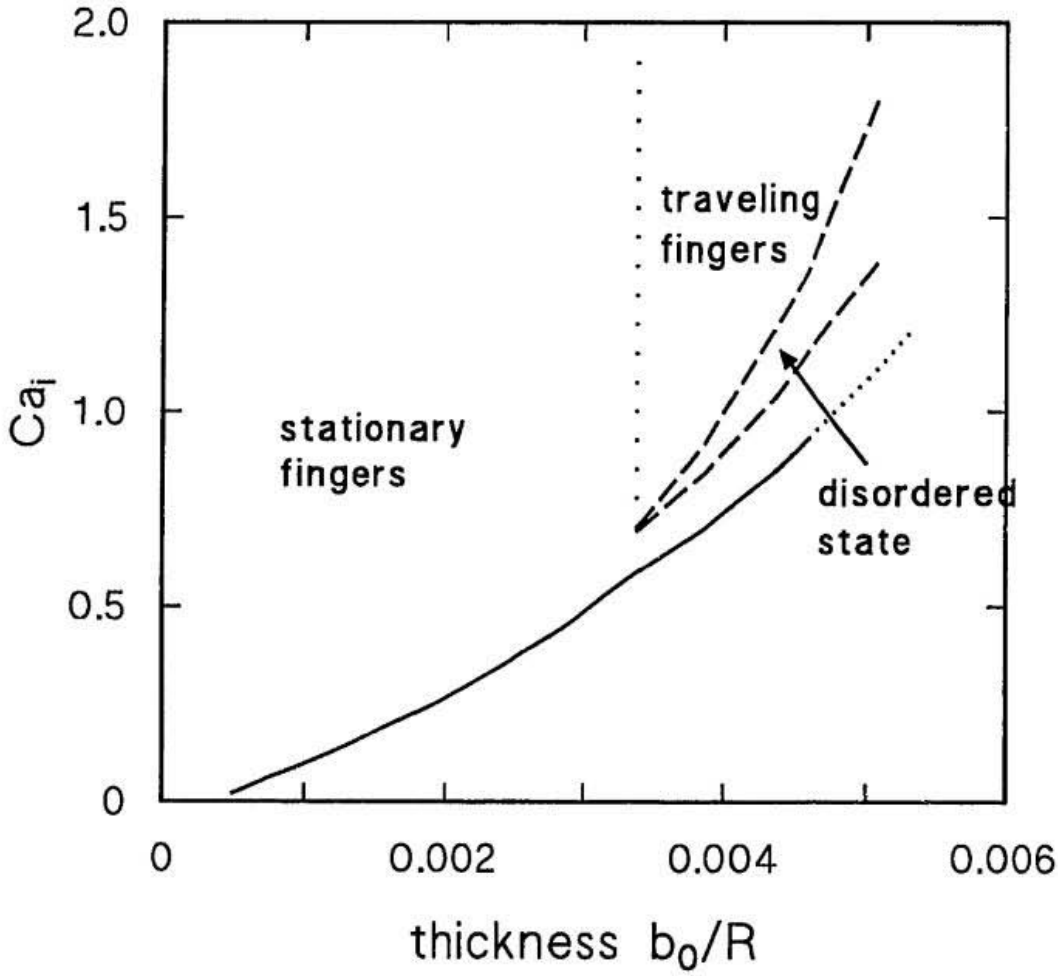

Figure 4.6: Phase diagram illustrating the behaviour observed when the bigger inner cylinder rotates while the outer cylinder remains fixed. The initial appearance of fingers is discontinuous for thin layers (solid line) and continuous for thicker layers (dotted line). The disordered state exists inside the region defined by the dashed lines, and above this region is the traveling finger state.

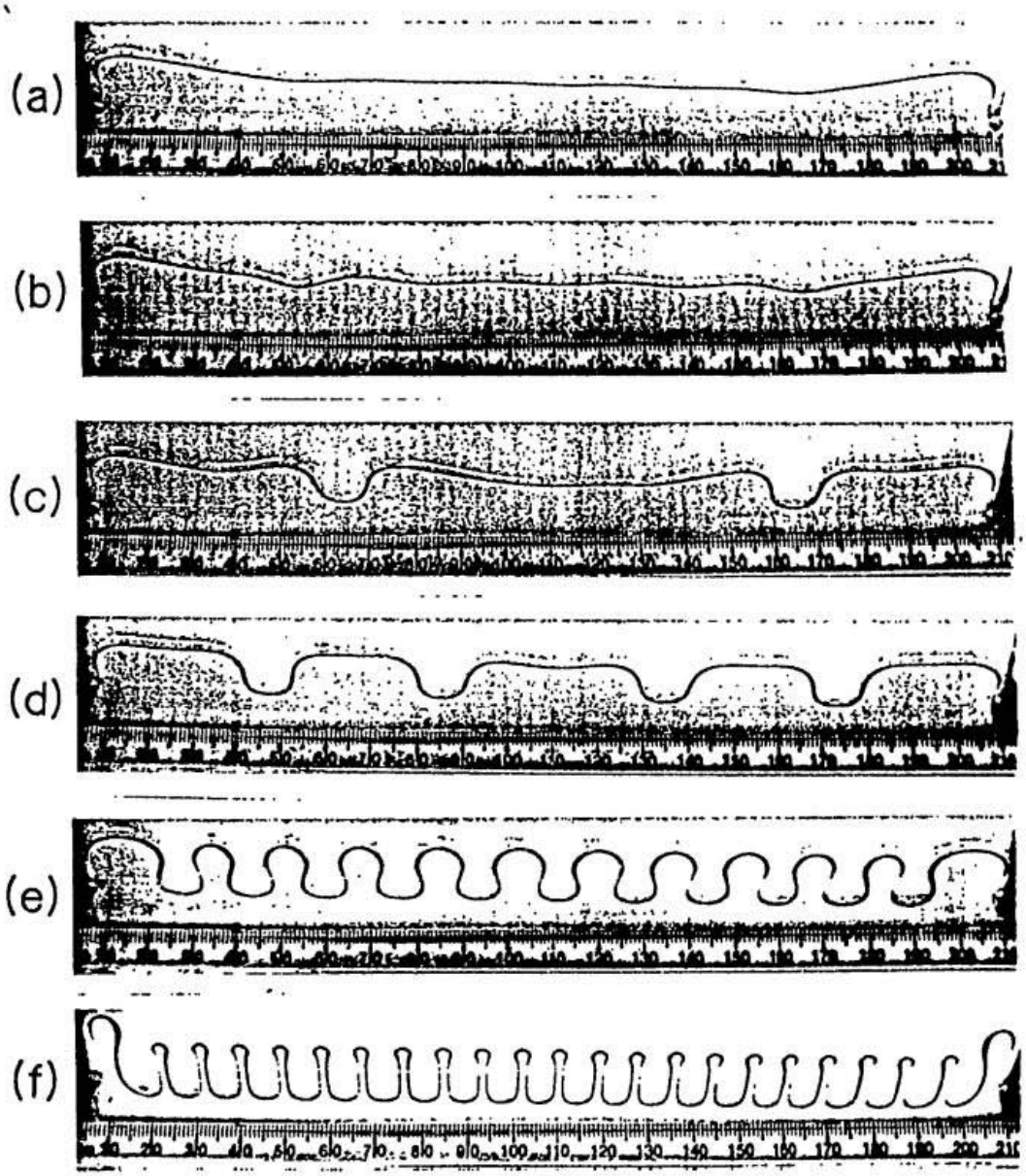

Figure 4.7: Development of the finger pattern formed when the outer cylinder is stationary while the bigger inner one rotates. $b_0/R = 0.0024$. (a) $Ca_i = 0.353$; (b) $Ca_i = 0.357$; (c) $Ca_i = 0.360$; (d) $Ca_i = 0.382$; (e) $Ca_i = 0.449$; (f) $Ca_i = 1.070$.

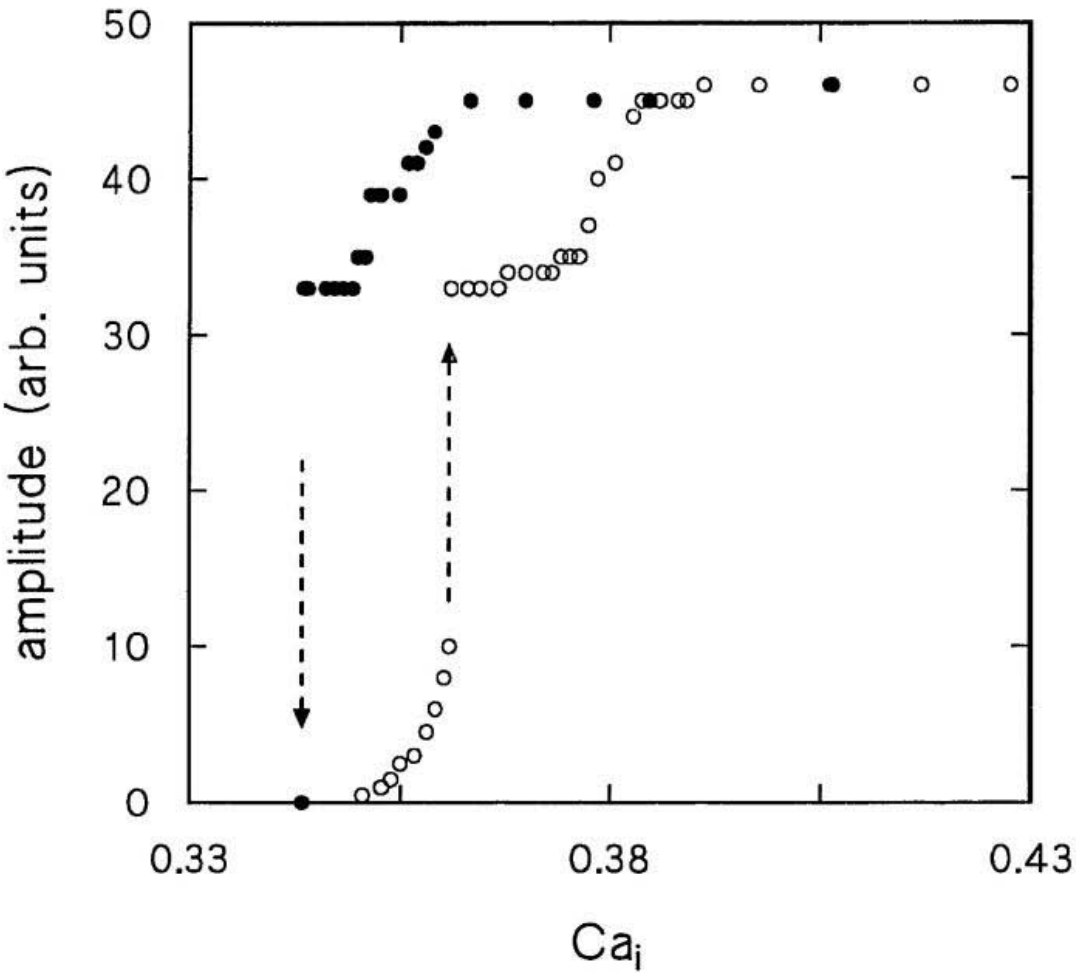

Figure 4.8: Finger amplitude as a function of Ca_i close to onset. $b_0/R = 0.0024$. Open circles: Ca_i increasing; solid circles: Ca_i decreasing. The hysteresis is defined by the difference between the capillary numbers at which the first hole appears and the last hole disappears.

discontinuous transition from the straight interface to the stationary fingering pattern. At each speed v_i, we waited up to several hours before recording the finger amplitude, and at the discontinuous jumps where the first hole appeared or the last hole disappeared, we waited more than 10 hours to ensure that the system had relaxed to a steady state. Close to the onset, the step in v_i between measurements was 0.08 mm/s, which corresponds to a step of 0.0022 in capillary number. At the high-Ca end of the hysteresis loop shown in Fig. 4.8, the pattern consisted of four fingers when Ca_i was increased, and eight fingers when Ca_i was decreased. Steps in amplitude can be seen corresponding to the appearance or disappearance of fingers over this range of Ca_i.

For layers with $b_0/R > 0.0034$, the behaviour was the same up to the point where there were roughly five fingers in the pattern. At higher rotation speeds, the stationary pattern then lost its left-right symmetry and the fingers began to drift along the length of the apparatus. The drift direction changed irregularly with time, as did the wavelength and relative width of the fingers. This disordered state is illustrated in Fig. 4.9(a), and Fig. 4.9(b) is a space-time plot of this state. This state persisted over a range of Ca_i. Above this range the pattern again became ordered, but consisting now of asymmetric traveling fingers as shown in Fig. 4.9(c), and in a space-time plot in Fig. 4.9(d).

For layers with $b_0/R > 0.0046$, the behaviour at the transition from the straight meniscus to the fingering state was similar to that described in the preceding paragraph, except that the amplitude of each finger (or hole) now grew continuously, and no amplitude jumps or hysteresis were observed at onset, as shown in Fig. 4.10. However, a hysteresis loop was observed above onset, when the pattern consisted of two fingers when Ca_i was increased and three fingers when Ca_i was decreased.

Fig. 4.11 is a plot of finger amplitude as a function of Ca_i for the same two layer

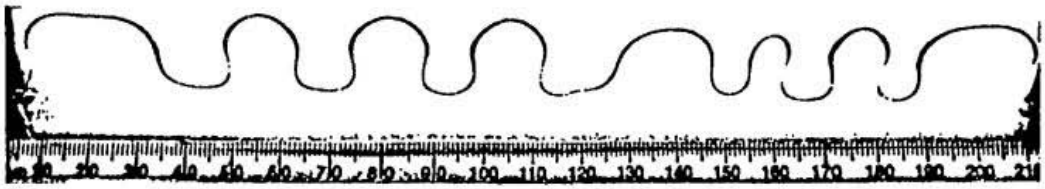

(a)

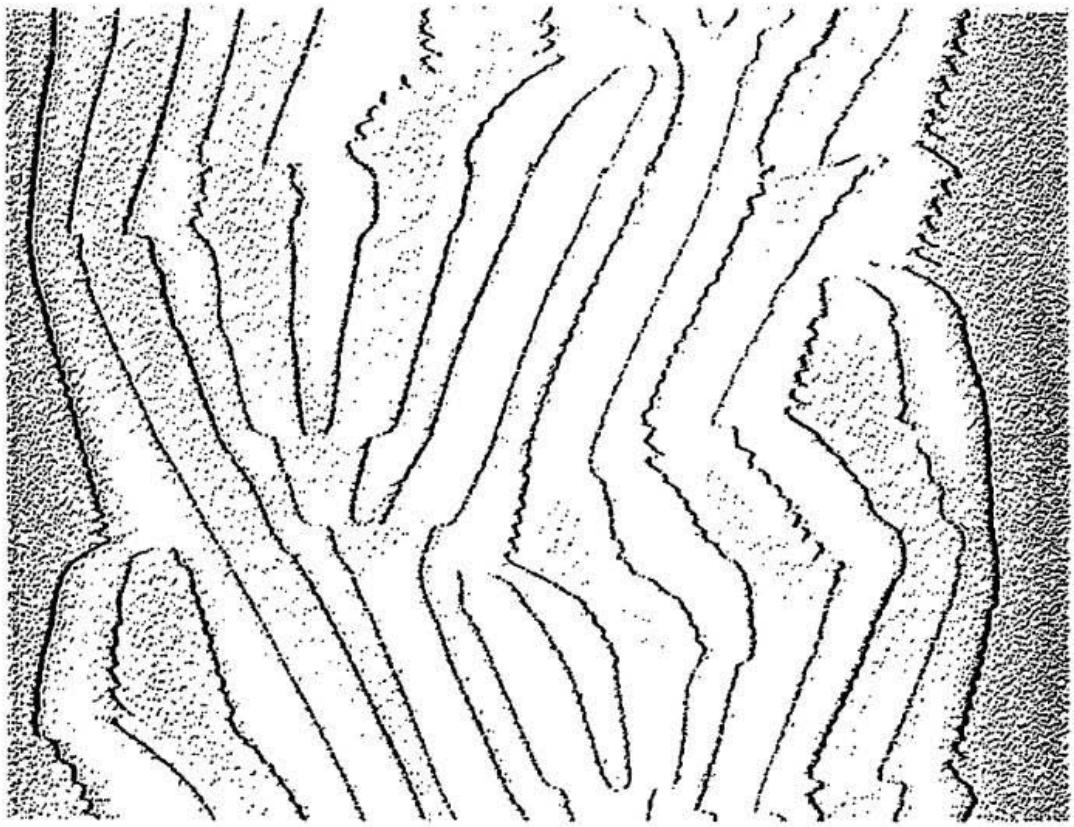

(b)

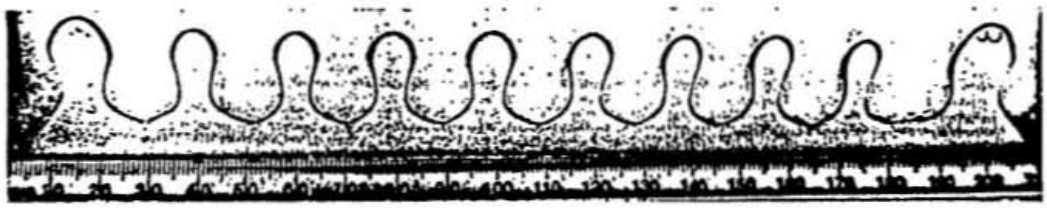

(c)

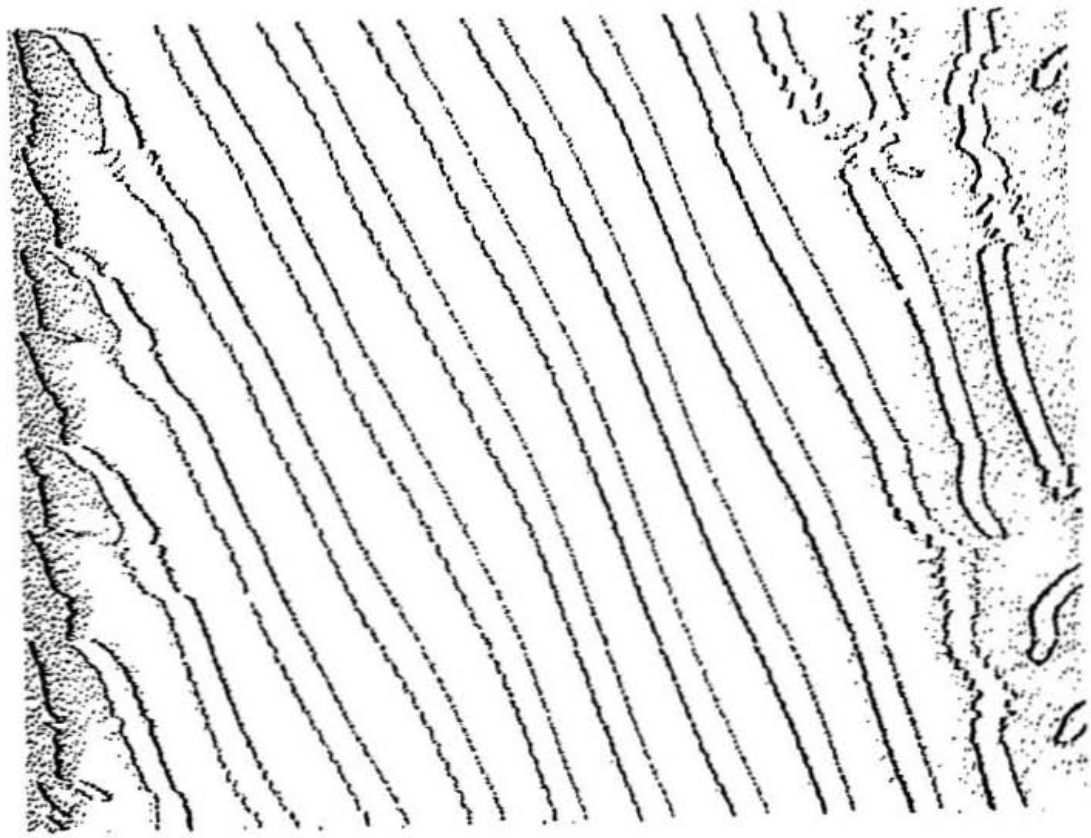

(d)

Figure 4.9: (a) A typical pattern observed in the disordered state with the bigger inner cylinder rotating. $b_0/R = 0.0041$, $Ca_i = 1.283$. (b) A space-time plot showing the pattern's motion in the same state. Time runs from top to bottom and the figure covers 48 s; $Ca_i = 1.027$. (c) Fingers in the traveling state that appears at speeds above the disordered state; $Ca_i = 1.497$. (d) A space-time plot of the same state for $Ca_i = 1.711$; here the figure covers 24 s.

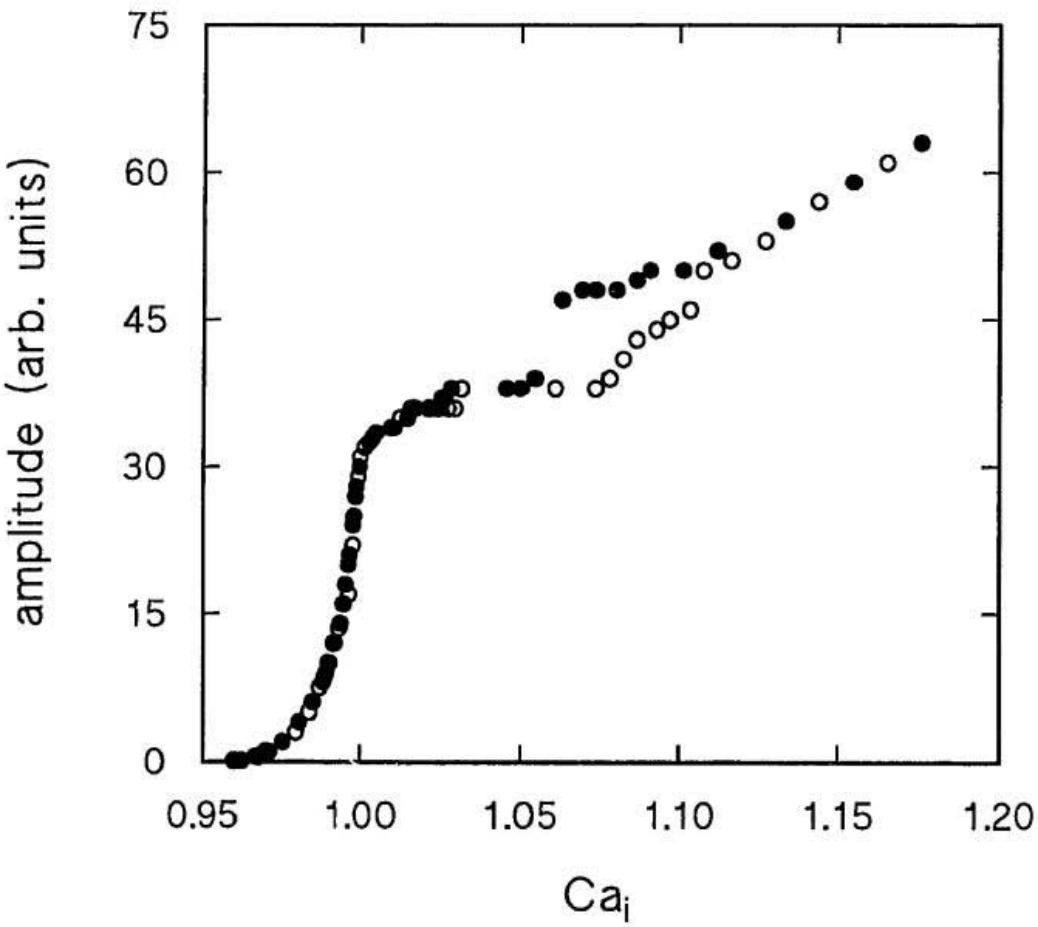

Figure 4.10: Finger amplitude as a function of Ca_i at onset at $b_0/R = 0.0046$, with the bigger inner cylinder used. Open circles: Ca_i increasing; solid circles: Ca_i decreasing.

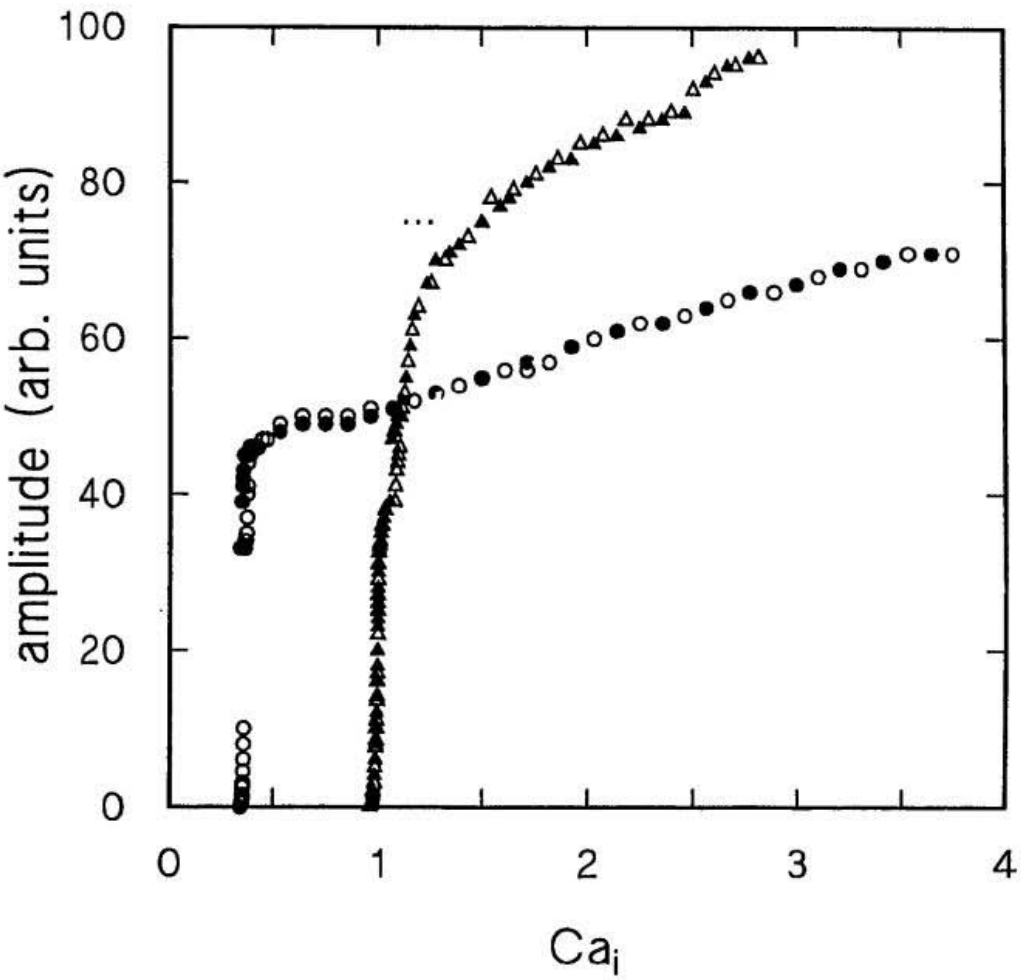

Figure 4.11: Finger amplitude as a function of Ca_i, for the same two cases as in Fig. 4.8 and 4.10, but over a larger range of Ca_i. Circles: $b_0/R = 0.0024$; triangles: $b_0/R = 0.0046$.

thicknesses as shown in Figs. 4.8 and 4.10. The range over which the disordered state described above exists for the thicker layer is indicated by the short dotted line in Fig. 4.11. Above this range, the pattern consisted of traveling fingers. For the thinner layer shown in Fig. 4.11, the pattern was always stationary. Note from Fig. 4.11 that the amplitude for the thicker layer well above onset is larger than that for the thinner layer. In contrast, for the case where the outer cylinder rotates, illustrated in Fig. 4.2, the amplitude for the thicker layer is always smaller. As with the outer cylinder data, the amplitude data were not well described by a simple power law, nor by fits to the Ginzburg-Landau equation for a backwards (discontinuous) bifurcation.

Fig. 4.12 is a plot of the width of the hysteresis loop, ΔCa, associated with the onset and final disappearance of the fingers. This width has a maximum for a gap width of $b_0/R = 0.0029$, dropping to zero for the thinnest gap we studied ($b_0/R = 0.00024$) as well as for $b_0/R \geq 0.0046$.

In addition to the large holes which appear at the meniscus, we also observed a small amplitude "ripple", sinusoidal in appearance. In layers with $0.00096 < b_0/R < 0.0019$ this ripple appeared at rotation speeds above those at which the holes appeared, but in thicker layers the ripple appeared first. Any possible growth of the ripple into larger amplitude fingers is apparently pre-empted by the growth of the holes as described above.

We measured the capillary number at the onset of the fingering pattern at different gap thicknesses, as shown in Fig. 4.4. Here the onset was defined as the capillary number at which the first jump in finger amplitude occurred when v_i was increased, shown as circles in Fig. 4.4, or at which the last hole suddenly disappeared as v_i was decreased, shown as downward-pointing triangles. These results are consistent with the data measured with the outer cylinder rotating, and in both cases the

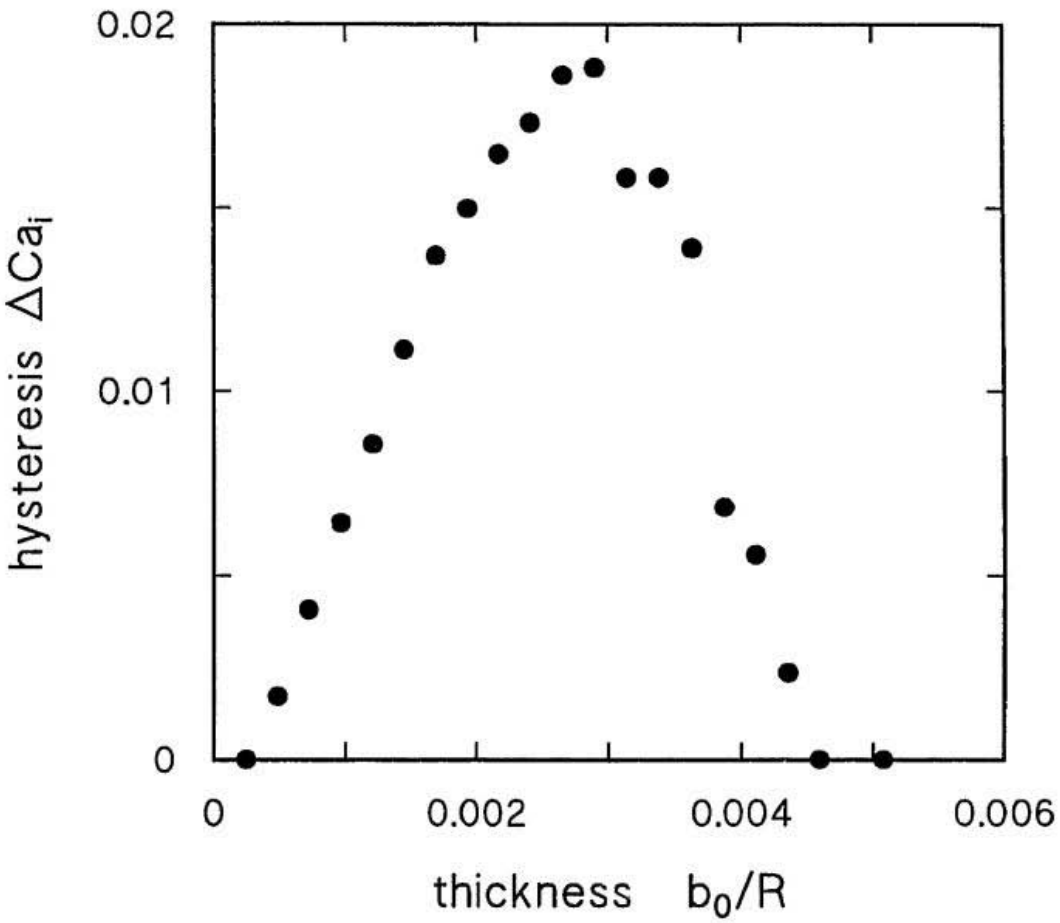

Figure 4.12: Width of the hysteresis loop associated with the initial appearance and final disappearance of the fingers with the bigger inner cylinder rotating, as a function of b_0/R.

measured values are substantially higher than the theoretical predictions of linear stability analysis.

The onset wavelengths are presented in Fig. 4.5, where the open circles represent the wavelength of the low-amplitude ripple, and the solid circles show the distance defined by the separation of the first two large-amplitude holes. The wavelength of the ripple shows no systematic variation — but a fair amount of scatter — as the gap width is changed. The spacing between the first two holes is constant for $b_0 \leq 0.3$ mm, then decreases with increasing gap thickness, appearing to level off again for large thickness. The distance between the first two holes is larger than half the system length when the gap is thin, and is apparently determined by the size of the system rather than any fundamental scale.

We also performed experiments using the more viscous oil B, and observed the same behaviour as described above when the inner cylinder rotated. The hysteresis was substantially smaller, although still present. When the outer cylinder rotated, the behaviour was the same as described in section 4.1.1. The measurements of the onset capillary number for this oil are also plotted in Fig. 4.4 as hexagons, and overlap the data for oil A essentially perfectly.

Fig. 4.13 is a plot of scaled wavelength as a function of capillary number for oil A, with the inner cylinder rotating at the same gap thicknesses as in Fig. 4.11. The gaps in the data just above onset correspond to sudden changes in wavelength that occur when a new hole forms. The onset is substantially delayed from the theoretical predictions, as in the case where the outer cylinder rotates. The short horizontal dotted line indicates the region where the pattern is disordered for the thicker layer. Above this gap the pattern consists of drifting asymmetric fingers. Well above onset, the wavelengths for the thinner layer, where the pattern is stationary, follow closely the calculated linear stability boundary, while for the thicker layer, where the

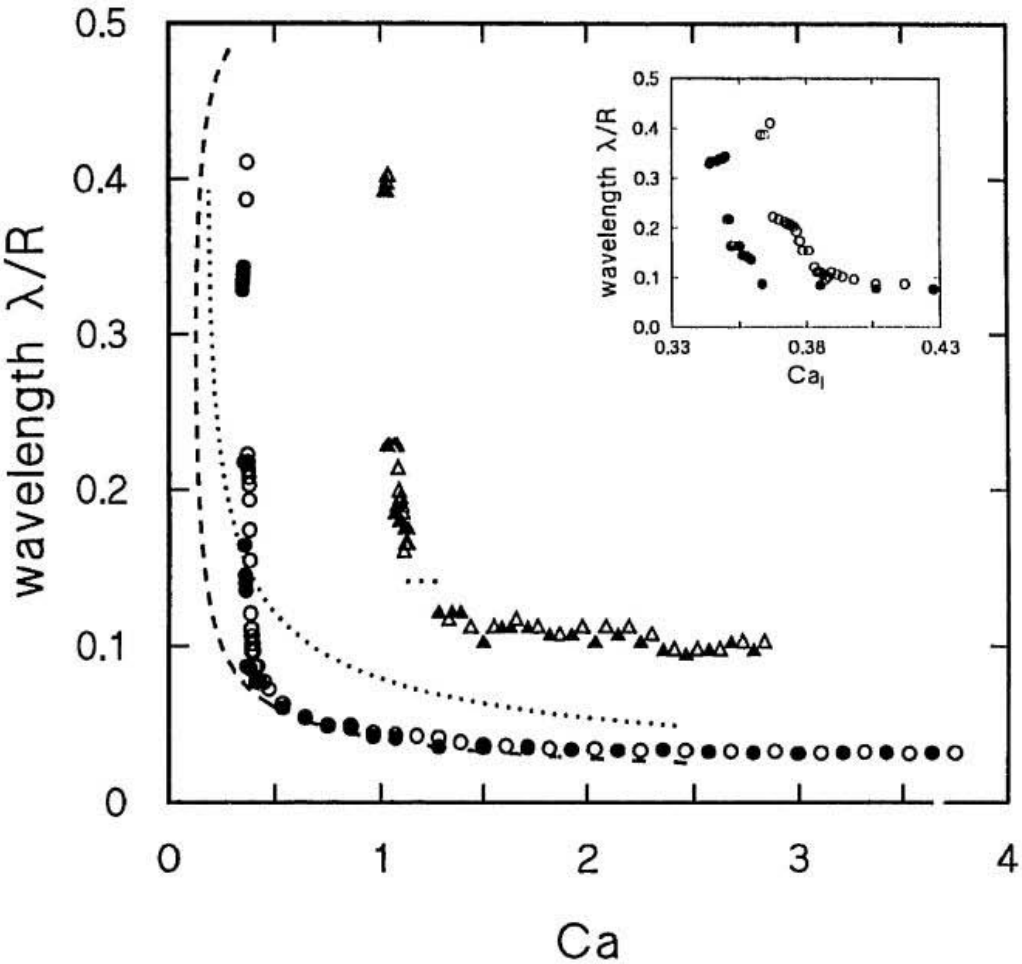

Figure 4.13: Pattern wavelength λ/R as a function of Ca_i, for the same cases as in Fig. 4.11. The inset shows the wavelength change close to the onset for $b_0/R = 0.0024$, where the hysteresis exists.

pattern is a traveling wave, the wavelengths remain about twice as high as the theoretical stability boundary.

From the above descriptions, we find that the transition at the onset of the stationary pattern is substantially different from the theoretical expectations. We believe that this is caused by boundary effects, since the scaled length for this inner cylinder is only 0.98. To test this hypothesis, we used a smaller inner cylinder, for which the scaled length is 5.07. The results are reported in the next section.

4.2 Experimental results with $r_1 = 24.85$ mm

In this section, results of experiments done with an inner cylinder with a radius $r_1 = 24.85$ mm, and scaled length $l_1/R = 5.07$, are presented. All experiments were done using oil A.

When this smaller inner cylinder was used, we found that the transition from the straight interface to the stationary pattern state was continuous, and no hysteresis was observed, no matter which cylinder, inner or outer, rotates. The stationary pattern was stable to higher rotation speeds than when the bigger inner cylinder was used. The disordered and traveling finger states described above, which exist for thicker layers when the bigger inner cylinder rotates, were not observed. Fig. 4.14(a) and (b) are plots of the scaled wavelength vs. capillary number, and the finger amplitude vs. capillary number, respectively, for the case that the outer cylinder rotates, while Fig. 4.15(a) and (b) are the corresponding plots for the inner cylinder rotating. In both cases, the amplitude of the finger grows rapidly as the rotation speed of the cylinder is increased, and then saturates at higher rotation rates. Well above onset, the thicker layer has larger finger amplitude than the thinner layer when the inner cylinder rotates, while when the outer cylinder rotates, the thinner layer has larger amplitude than the thicker layer. This behaviour is the

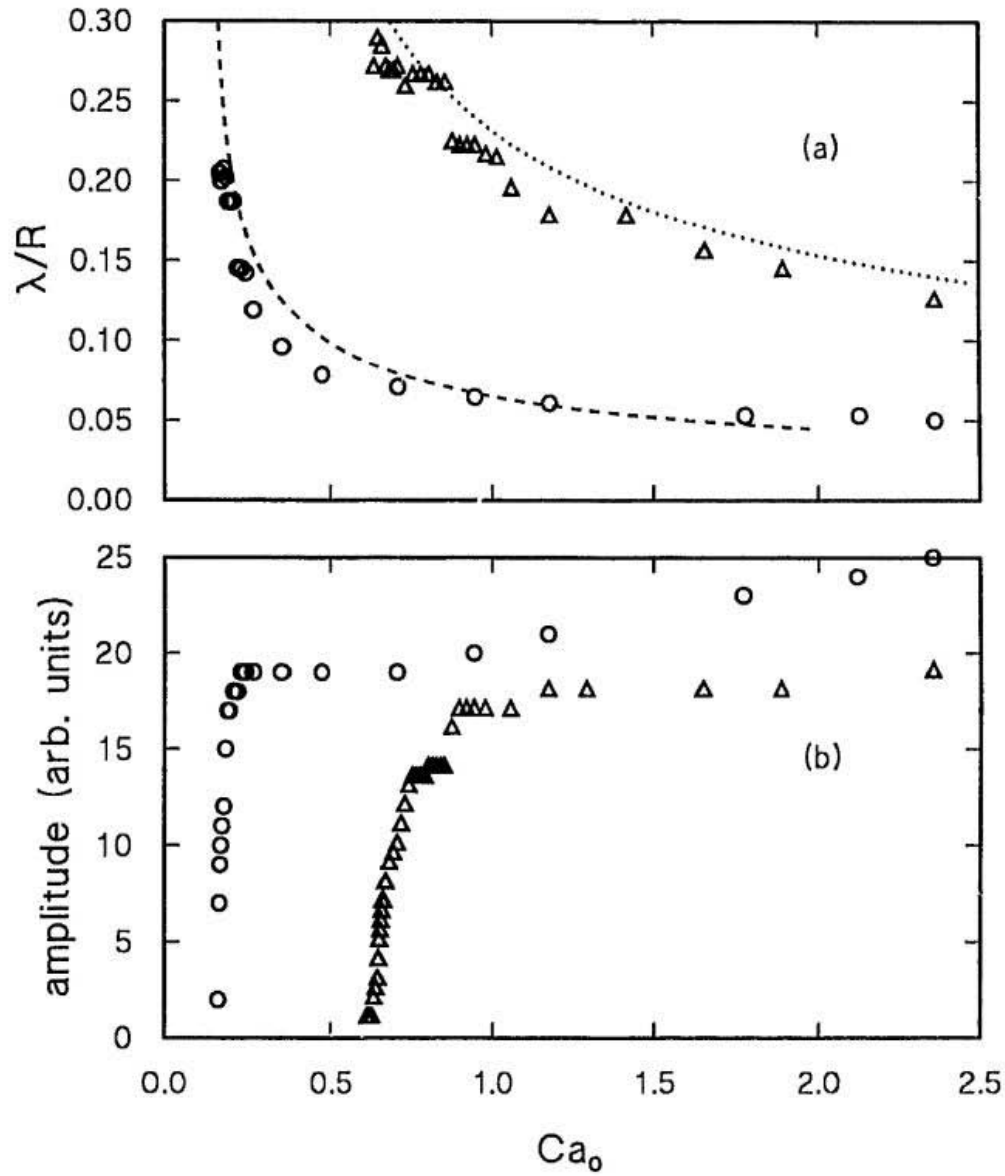

Figure 4.14: (a) Finger amplitude vs. Ca_o for two gap thicknesses with the smaller inner cylinder used. Circles: $b_0/R = 0.0038$; triangles: $b_0/R = 0.013$. (b) Pattern wavelength vs. Ca_o for the same cases as in (a). The dotted and dashed lines are calculated stability boundaries.

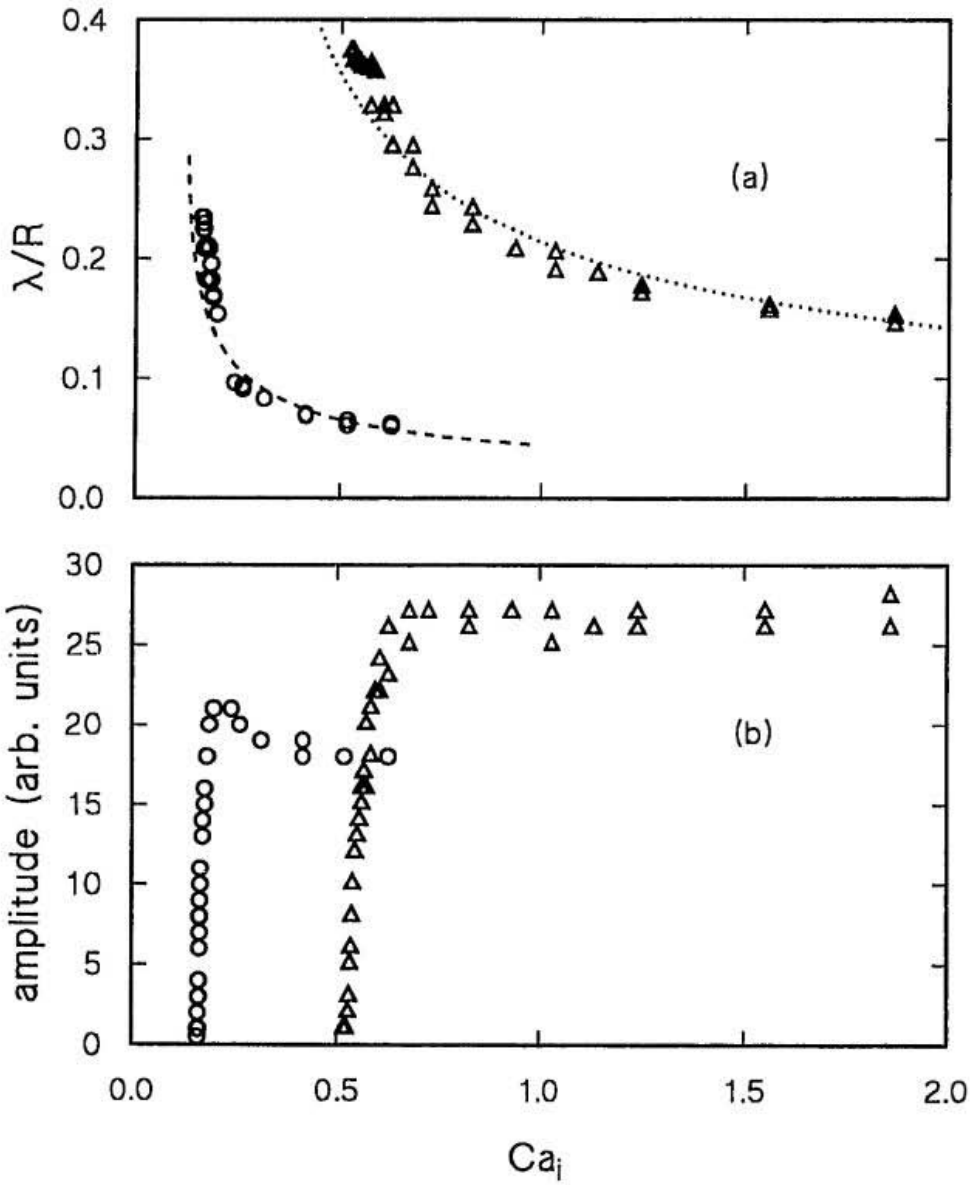

Figure 4.15: (a) Finger amplitude vs. Ca_i for two gap thicknesses with the smaller inner cylinder used. Circles: $b_0/R = 0.0025$; triangles: $b_0/R = 0.011$. (b) pattern wavelength vs. Ca_i for the same cases as in (a). The dotted and dashed lines are calculated stability boundaries.

same as that when bigger inner cylinder was used. When the cylinder speed is increased, the finger wavelength decreases as before. Comparing Figs. 4.14 (a), and 4.15(a) with Figs. 4.3 and 4.13, we can see that the wavelengths around onset for the smaller inner cylinder are closer to the theoretical calculations than when the bigger inner cylinder was used.

We also measured the onset capillary number and onset wavelength for this smaller inner cylinder. The results are presented in Figs. 4.4 and 4.5 as diamonds for the outer cylinder rotating, and by upward-pointing triangles for the inner cylinder rotating. The onset capillary numbers for both inner and outer cylinders rotating are consistent with each other as before. In this case, however, the results agree much more closely with the theoretical calculation, although the measured onset capillary numbers are still higher than the theoretical values when b_0/R is high. Similarly, the onset wavelengths for the smaller inner cylinder are closer to, although still lower than, the theoretical calculation than was the case when the bigger inner cylinder was used.

4.3 Discussion

We now compare our experimental results with other experimental results on coating systems. Fig. 4.16 is a graph originally from Ref. [69], to which we have added our results. For consistency with the way quantities are defined in Ref. [69], in Fig. 4.16 $Ca_c = \mu(v_1 + v_2)/2\sigma$ is plotted against $b_0/4R$, where v_1 and v_2 are the rotation speeds of the two cylinders. The data from other experiments, plotted in Fig. 4.16, were obtained with experimental systems consisting of two cylinders mounted either side by side or one above the other [60, 62, 69, 88, 89]. Also included in Fig. 4.16 are the experimental results of Hakim et al. [73] (shown as crosses) for an experimental system consisting of a single cylinder rotating above a plane surface, with $l_1/R = 6$.

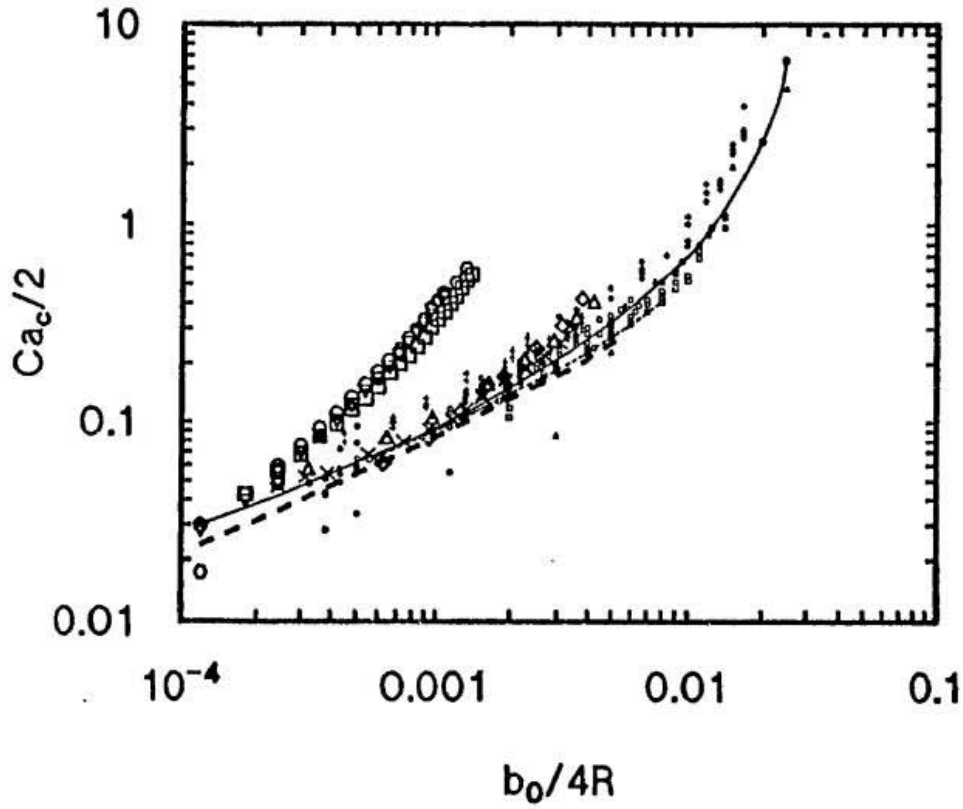

Figure 4.16: $Ca_c/2$ vs. $b_0/4R$ (units have been chosen for consistency with Ref. [69]). Data from this work are shown using the same symbols as in Fig. 4.4. Data from the work of Hakim et al. are presented as crosses. Data from previous work on coating systems are taken from Ref. [69], and represented by small symbols: squares: Ref.[60]; circles: Ref. [62]; triangles: Ref. [88]; pluses: Ref. [89]; diamonds: Ref. [69]; solid line: calculation by Coyle et al. [69]; thinner dashed line: calculation by Rushak [67]; thicker dashed line: this work.

The dimensionless lengths l/R for all of the previous experiments plotted in Fig. 4.16 range from 5.5 to 7.9, and no systematic change in Ca_c with l/R can be seen in these data. The solid curve in the figure is the theoretical result of Coyle et al. [69] calculated by a two-dimensional finite-element analysis of the symmetric film-splitting flow in a forward-roll-coating configuration. The short dashed curve is that calculated by Ruschak [67] by a stability analysis of the asymptotic equations for two-dimensional flow near the meniscus, using a nearly-rectilinear approximation, and the long-dashed curve is the theoretical result shown above in Fig. 4.5. Our experimental results with the smaller inner cylinder, with $l_1/R = 5.07$, agree with the other experimental results and the theoretical calculations quite well, suggesting that when the effective length is larger than about 5, boundary effects are not significant. In the case that $l/R = 0.98$, however, the onset of the fingering instability is substantially delayed over what is expected from both the theoretical and the other experimental results, suggesting that in this case boundary effects are quite important.

From the above comparison, we can conclude that end effects somehow stabilize the meniscus beyond the point at which fingering would occur in the infinitely long system and that the shorter the dimensionless length, the more the onset of fingering is delayed. This result has potential applications in the coating industry: the onset of instabilities which lead to uneven coating thickness could be delayed to higher coating speeds by constructing a coating system with a small value of l/R.

The effect of the finite cylinder length on the actual flow is different depending on which of the two cylinders rotates. This was observed when the bigger inner cylinder was used: the transition behaviour with the outer cylinder rotating was different from that with the inner cylinder rotating. Our outer cylinder is 8 mm longer than the inner cylinder, so there is a 4 mm space at each end, between the

ends of the two cylinders. The behavior of the oil in this space determines the boundary conditions at the ends of the meniscus, but a detailed analysis of the flow in this region is required before any definitive statements can be made.

The effect of the gravitational force on the flow is also different depending on which cylinder is rotating. When the cylinders rotate, viscous forces pull the oil up at the front meniscus, but the gravitational force drags it down. The drag force on the film coated on the outer cylinder is balanced partly by the normal force of the outer cylinder, therefore the gravitational effect on the film coated on the outer cylinder is smaller than that coated on the inner cylinder.

In our experiments, and also in those of Hakim et al. [73], the pattern wavelength above onset is quite close to that at the edge of the linear stability boundary. Normally one would expect the pattern to become unstable to the Eckhaus instability [43] before the wavelength reached the linear stability boundary. The Eckhaus instability has been observed in many other experiments [9,45-51,90]. Riley and Davis [91] and Proctor [92] have theoretically studied the Eckhaus instability in the case that the linear stability boundary is flatter than the usual parabolic shape near its minimum, as is the case in our experiment. They conclude that the flatter is the linear stability boundary, the closer the Eckhaus instability to the linear stability boundary, and the narrower the band of Eckhaus-unstable wavelengths.

Recently, Fourtune et al. [51] studied the Eckhaus instability in a system similar to ours. In their experiments, a single cylinder rotated under a horizontal glass plate. The interface between the air and the oil film pulled through the small gap between the cylinder and the plate exhibited a stationary pattern similar to that in our experiment. Fourtune et al. measured the range of the control parameter over which a pattern with a particular wave number was stable, that is, the stability boundary of the stationary pattern. Their results are very similar to those shown

in the inset to Fig. 4.13. This inset shows in more detail the pattern wavelength for increasing and decreasing v_i, close to onset. In this region of Ca, hysteresis exists as described in section 4.1.2. At a particular value of Ca, there are fewer fingers when Ca is increased than when Ca is decreased, or, in other words, the pattern has a longer wavelength when Ca is increased than when it is decreased. In their paper [51], Fourtune et al. identify the low wavelength boundary of the hysteresis loop with the the Eckhaus boundary, while at the long wavelength boundary the pattern wavelength changes via a propagative localized state of broken parity. In our experiment, in the range shown in the inset to Fig. 4.13, the wavelength jumps occurred when a hole appeared at the interface on increasing Ca_i or disappeared on decreasing Ca_i, as described above. When Ca_i was varied between hole appearances and disappearances, the wavelength changed smoothly. At the high-wavelength side of the boundary, propagative localized states of broken parity waves were observed when new fingers appeared as Ca_i was increased. When Ca_i was decreased, the disappearance of fingers occurred through the coalescence of two neighbouring fingers, as would be expected at an Eckhaus boundary. These results are consistent with those of Fourtune et al.

As described above, when the bigger inner cylinder rotates, with gap thickness $b_0/R > 0.0034$, the stationary pattern becomes unstable to a parity-breaking traveling wave. In this case, increasing a single control parameter drives the system through two successive instabilities, from the straight interface to the stationary pattern, and then from this stationary pattern to traveling finger state. In the case that the cylinders counter-rotate, two control parameters must be varied in order to reach a parity breaking transition, as will be discussed in the next chapter. Similar successive transitions involving only one control parameter have been observed in the directional solidification of liquid crystals [9, 10, 24] and lamellar eutectics

[18-20]. In our experiments, close to the onset of this parity breaking state, there is a small region in the control parameter where the drifting pattern is unstable. This is in agreement with the theoretical prediction described in section 2.3.2, that the parity-breaking state is not stable at onset. According to theoretical predictions [25-27], the drift speed of the parity-breaking wave should be proportional to the degree of asymmetry of the pattern. We have not studied the behaviour of the broken-parity state observed here in detail, however, a quantitative analysis of the parity-breaking state for counter-rotating cylinders will be presented in Chapter 5.

Chapter 5

Experimental Results with Cylinders Counter-Rotating

When the two cylinders in our experimental apparatus counter-rotate, a variety of dynamical states can occur, depending on the velocity of the cylinders. These include broken-parity traveling waves (TW), solitary waves (SW) and stationary fingering patterns (S) as shown in the phase diagram of Fig. 1.3. In this chapter we present the results of experiments on the broken-parity traveling wave state labeled TW in Fig. 1.3. In section 5.1, the dynamical behaviour of the traveling-wave state is described. In section 5.2, the results are analyzed and compared with theoretical expectations. The experiments reported here were done using the inner cylinder with radius $r_1 = 50.4$ mm, and oil A. The gap thickness was fixed at $b_0/R = 0.0024$.

5.1 Results

The experiments reported in this chapter were done in the parity-breaking state which lies in the area labeled TW in the second quadrant of the phase diagram shown in Fig. 1.3. In a typical experimental run, shown by the dashed straight line in Fig. 1.3, we set the outer cylinder's velocity to a value above the onset of the stationary fingering pattern, which for our geometry occurred at $v_{in} = 111.5 \pm 2.5$ mm/s. After allowing this pattern to stabilize, we then increased the inner cylinder velocity in small steps in the opposite direction, i.e., such that the cylinders were counter-rotating, allowing sufficient time between steps for the pattern to reach a steady state. In this case the control parameter is the inner cylinder rotation speed.

5.1.1 Uniform broken-parity waves

At values of the outer cylinder speed below 157 mm/s ($1.4v_{oc}$), a periodic pattern of traveling fingers, moving with constant speed, was observed. This state exists in the shaded region of Fig. 1.3.

Fig. 5.1 shows a sequence of interface patterns observed for a particular value of the outer cylinder rotation speed, v_o, as the inner cylinder's rotation speed, v_i, is increased in small steps from zero. Initially, with $v_i = 0$, the pattern is stationary and has left-right reflection symmetry, as in Fig. 5.1(a). When v_i is increased slightly above zero, the pattern of fingers at the interface loses its reflection symmetry, and begins to drift along the length of the apparatus. Initially, the drift is spatially disordered. The pattern contains source and sink defects, at which domains of fingers drifting in opposite directions meet. This disorder is transient in this region of v_o, and the interface quickly settles down to a spatially uniform pattern of asymmetric, drifting fingers. As v_i is further increased, the asymmetry of the fingers and the wavelength of the pattern both increase, as can be seen in Fig. 5.1, as does their phase velocity. Fig. 5.2 shows a space-time image corresponding to a left-moving pattern, which shows that the traveling speed of the pattern is uniform. Patterns with both signs of asymmetry (i.e., left-leaning and right-leaning) were observed, with the direction of drift depending on the sense of the asymmetry; those in Fig. 5.1 lean to the right and move to the left.

At still higher v_i, the pattern suddenly regains its reflection symmetry and stops drifting, as shown in Fig. 5.1(g). The traveling speed and asymmetry drop discontinuously to zero. This transition is hysteretic: if v_i is now decreased, the drifting pattern does not reappear until somewhat below the value of v_i at which it disappeared. The wavelength of the stationary pattern which reappears at higher v_i is always slightly larger than that at $v_i = 0$. At still higher v_i, the stationary fingers

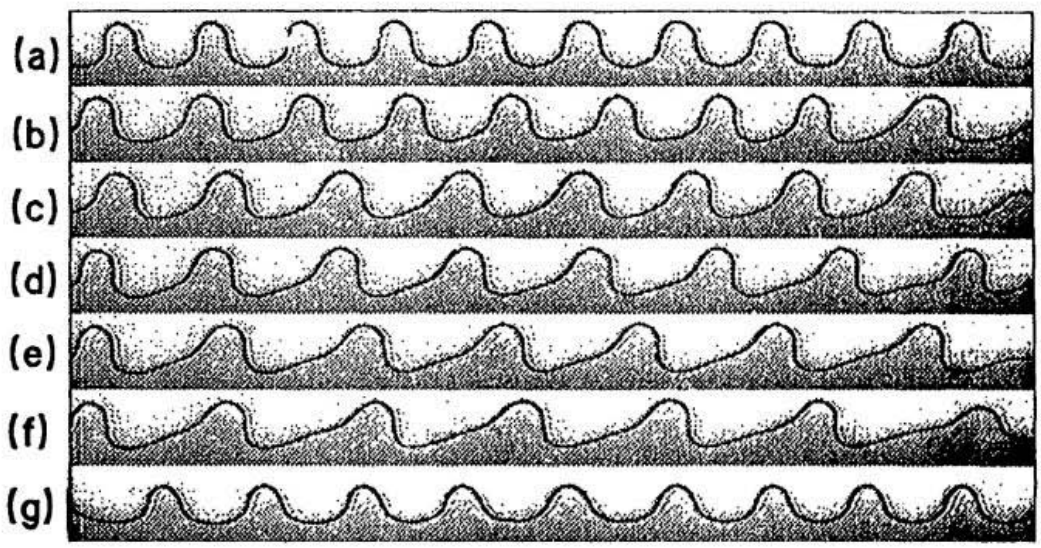

Figure 5.1: Patterns observed at the oil-air interface with $v_o = 139.4$ mm/s. (a) Stationary, symmetric fingers at $v_i = 0$; (b)-(f) asymmetric fingers drifting uniformly to the left at successively higher values of v_i: (b) $v_i = 6.3$ mm/s; (c) $v_i = 7.9$ mm/s; (d) $v_i = 9.5$ mm/s; (e) $v_i = 11.1$ mm/s; (f) $v_i = 12.7$ mm/s; (g) stationary, symmetric fingers at $v_i = 15.8$ mm/s.

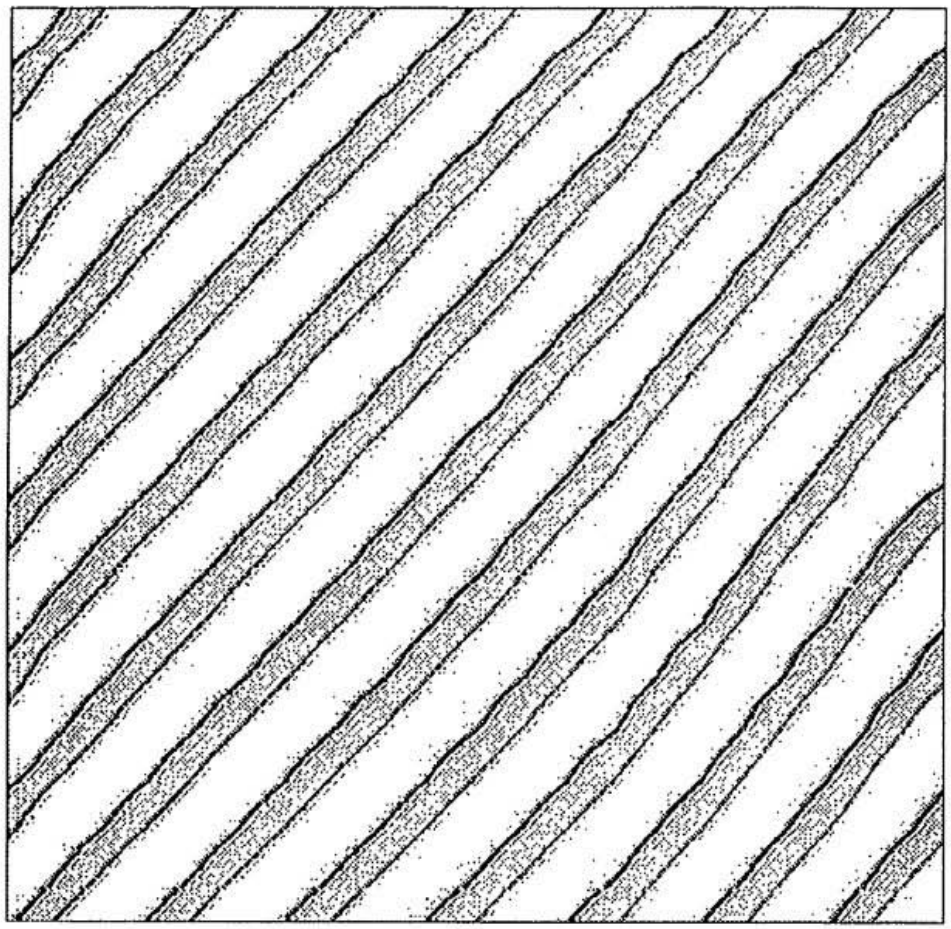

Figure 5.2: Space-time images of a uniform traveling pattern at $v_o = 143.8$ mm/s, $v_i = 9.5$ mm/s. Time runs from top to bottom and the figure covers 24 s. 134 mm of the pattern are shown.

lose stability and straight meniscus returns.

We measured the phase speed of the pattern, v_ϕ, from space-time images such as in Fig. 5.2, and v_ϕ^2 is plotted as a function of v_i in Fig. 5.3. Data for five values of v_o between 139 mm/s and 157 mm/s are shown, with the different symbols corresponding to different values of v_o. Within our experimental uncertainty, no dependence of the slope on v_o can be discerned, but the range of existence of the traveling-wave state increases linearly with increasing v_o. This is shown in the inset to Fig. 5.3, where we have plotted the maximum value of v_i at which the traveling patterns were observed, as a function of v_o. The data plotted in Fig. 5.3 cover the entire range of v_i over which the traveling-wave state exists. A fit of the data to a straight line gives

$$v_\phi^2 = (4.48 \pm 0.09)\,(v_i - (3.9 \pm 0.2))\,, \tag{5.1}$$

with v_ϕ and v_i in units of mm/s. In this case, the parity-breaking transition occurs at a critical rotation speed $v_i^* = 3.9 \pm 0.2$ mm/s. v_ϕ starts to grow continuously from zero at v_i^*, and v_ϕ^2 is linear in the control parameter v_i.

When v_i is increased, the wavelength of the pattern also increases. Fig. 5.4 is a plot of the pattern's wave number, q, as a function of v_i, for three values of v_o, and illustrates the steady decrease in q as the control parameter is increased through the traveling-wave state. At the transition back to the stationary pattern at higher v_i, the wave number jumps back up, but its value in the high-v_i stationary-finger state is always smaller than that in the $v_i = 0$ state. The lines in Fig. 5.4 simply connect the data points for each value of v_o and are intended only to guide the eye.

5.1.2 Nonuniform broken-parity waves

When the outer cylinder rotation speed is above 157 mm/s, the traveling patterns we observed were no longer spatially uniform, and their behaviour was rather more

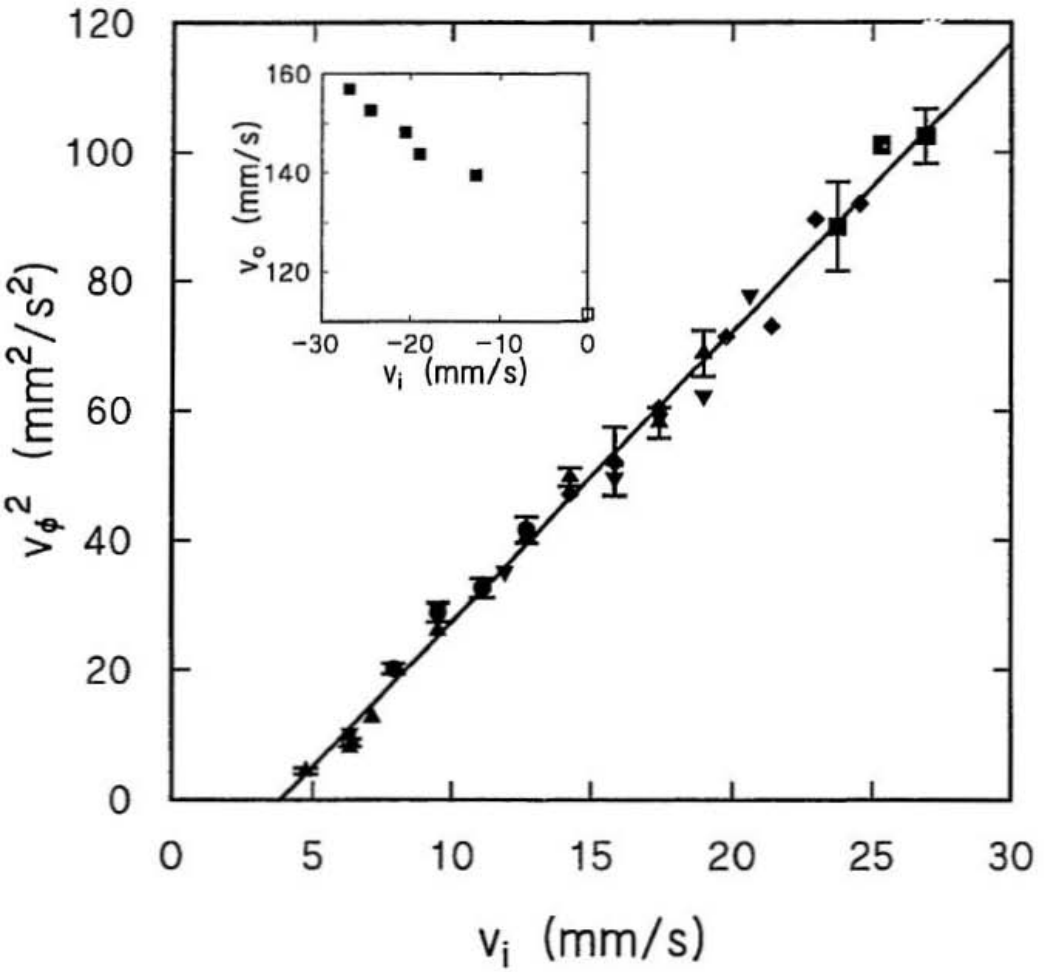

Figure 5.3: The square of the pattern's phase velocity, v_ϕ^2, as a function of v_i for several values of v_o of uniform traveling waves. Circles: v_o = 139.4 mm/s; upward-pointing triangles: v_o = 143.8 mm/s; downward-pointing triangles: v_o = 148.1 mm/s; diamonds: v_o = 152.5 mm/s; square: v_o = 156.9 mm/s. The line is a least-squares fit to the data.

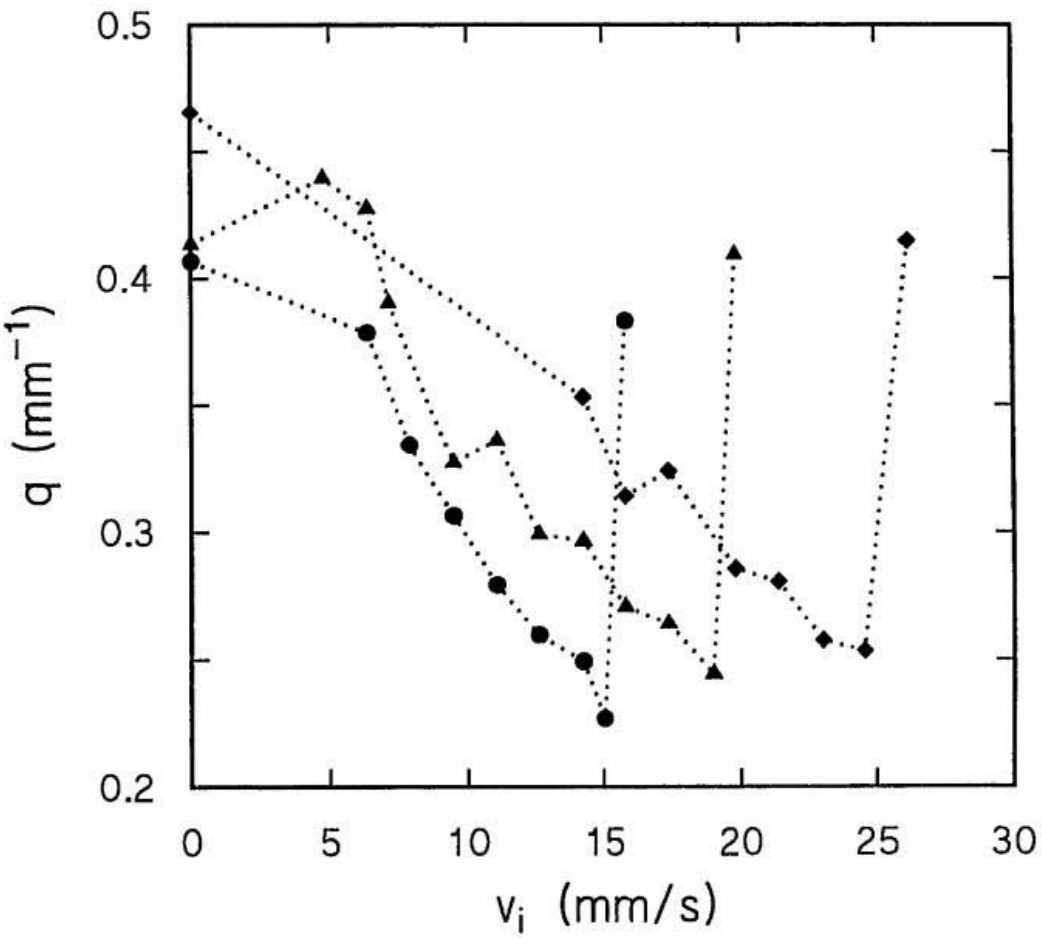

Figure 5.4: The uniform pattern's wave number as a function of v_i for three values of v_o; symbols are as in Fig. 5.3. The lines connecting the points are guides to the eye.

complicated than that of the uniform traveling waves seen at low v_o. As before, the stationary fingering pattern exists at $v_i = 0$. As soon as v_i becomes nonzero, the fingers of the stationary pattern lose their reflection symmetry and begin to drift. When v_i is very small, this traveling state is chaotic. However, unlike the case where v_o is low, this disordered drifting state never settles down. This observation agrees with the theoretical expectation discussed in section 2.3.2 above, that the traveling state is unstable at onset.

When v_i is further increased, a more ordered traveling-wave state develops. However, this pattern is never perfectly uniform, nor is it stable in time. Source or sink defects can remain in the pattern, typically near the end of the apparatus, but usually the traveling fingers appear at one end of the apparatus and disappear at the other. Fig. 5.5 shows a series of traveling patterns observed for v_o= 174 mm/s, as v_i is increased. At any given time, the wavelength of the pattern changes along its length, as can be seen in Fig. 5.5. When the fingers are moving away from a source defect, the pattern's wavelength increases along its direction of propagation, while if they are moving towards a sink defect, the wavelength decreases. Furthermore, this pattern only exists for, typically, a few minutes at a time, after which it again becomes disordered. After a few seconds, the disorder passes and the pattern returns to one like those in Fig. 5.5, and so on. Patterns moving in either direction can occur, and often the direction of propagation is reversed after the passage of a disordered burst.

As v_i is further increased, the pattern's average wavelength, phase speed and finger asymmetry all increase, as was found for the uniform traveling patterns at low v_o. The variation in wavelength along the pattern also becomes more pronounced, and the intermittent bursts of disorder more frequent. Patterns from this regime are illustrated in Fig. 5.5(b-d). A sudden transition occurs between Fig. 5.5(d) and

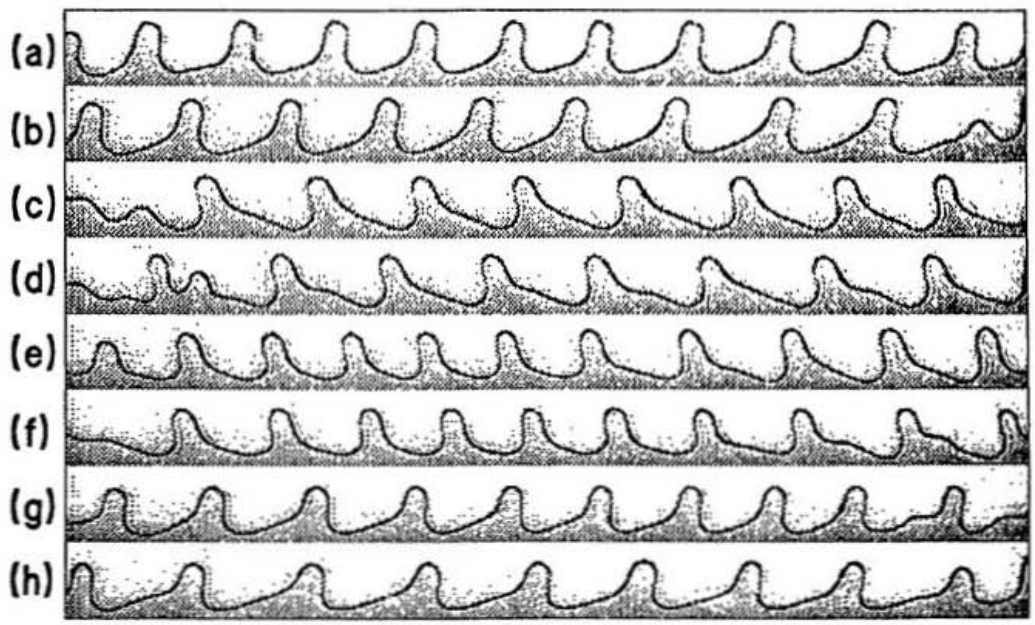

Figure 5.5: Nonuniform traveling-finger patterns at $v_o = 174.3$ mm/s. (a) $v_i = 6.33$ mm/s; (b) $v_i = 11.08$ mm/s; (c) $v_i = 12.67$ mm/s; (d) $v_i = 15.83$ mm/s; (e) $v_i = 17.42$ mm/s; (f) $v_i = 19.79$ mm/s; (g) $v_i = 23.75$ mm/s; (h) $v_i = 27.71$ mm/s. The images show 174 mm of the pattern's length.

(e), at which the pattern's average wavelength drops, and the phase speed and asymmetry of the fingers also decrease. As v_i is increased above this transition, the wavelength of the traveling pattern becomes more uniform and the the disordered periods appear less frequently, and the average wavelength, traveling speed, and asymmetry increase again, as shown in Fig. 5.5(f-h). Eventually, the solitary wave (SW) region of Fig. 1.3 is reached, in which localized patches of broken parity symmetry travel through a background of stationary fingers, then the stationary finger state, and, finally, the straight interface reappears.

Fig. 5.6 is a space-time image, showing the motion of a pattern traveling to the left, over a period of 24 seconds. For this pattern, v_o = 174 mm/s and v_i =23.8 mm/s, as in Fig. 5.5(g). This picture illustrates the increase in the wavelength and traveling speed of the fingers in the pattern as they move along the length of the apparatus.

The way in which the pattern's characteristics vary along the interface, at a fixed time, is illustrated in Fig. 5.7, for which v_o = 261.4 mm/s and v_i = 55.42 mm/s. The particular image from which the data were taken is shown in Fig. 5.7(a). The fingers propagate away from the source defect at the left side of the image, so most of the pattern is moving to the right. The local wavelength, defined as the distance between adjacent minima in the interface height, the asymmetry (see below) of each individual finger, and each finger's traveling speed, determined by simply measuring the distance a finger moved over a small number of video frames are shown as a function of position, in Fig. 5.7(b-d). The finger closest to the source is longer, as can be seen in Fig. 5.7(a), more asymmetric and faster moving than its neighbours. This reflects the mechanism by which new fingers appear at the source. Existing fingers move away from the defect. When the distance between the source and the nearest finger becomes too large, small ripples appear close to the defect,

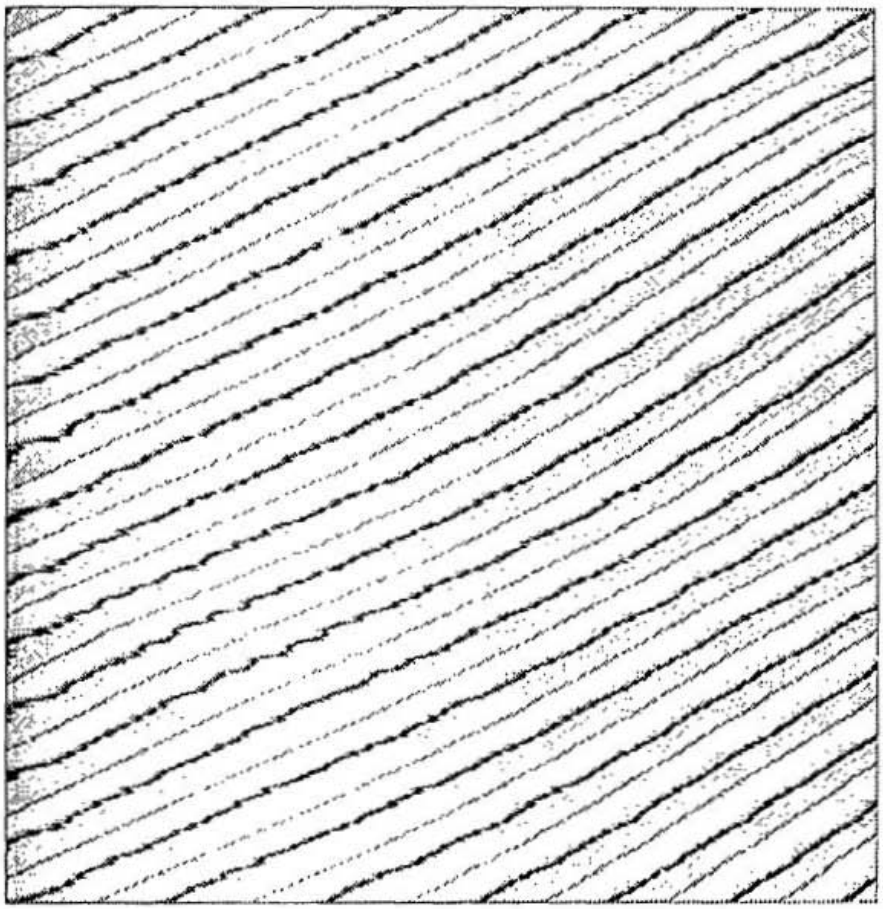

Figure 5.6: A space-time image of a nonuniform pattern traveling to the left at v_o = 174.3 mm/s, v_i = 23.75 mm/s. The speed and wavelength of the fingers increase as they move along the length of the apparatus. Time runs from top to bottom and the figure covers 24 s. 127 mm of the pattern are shown.

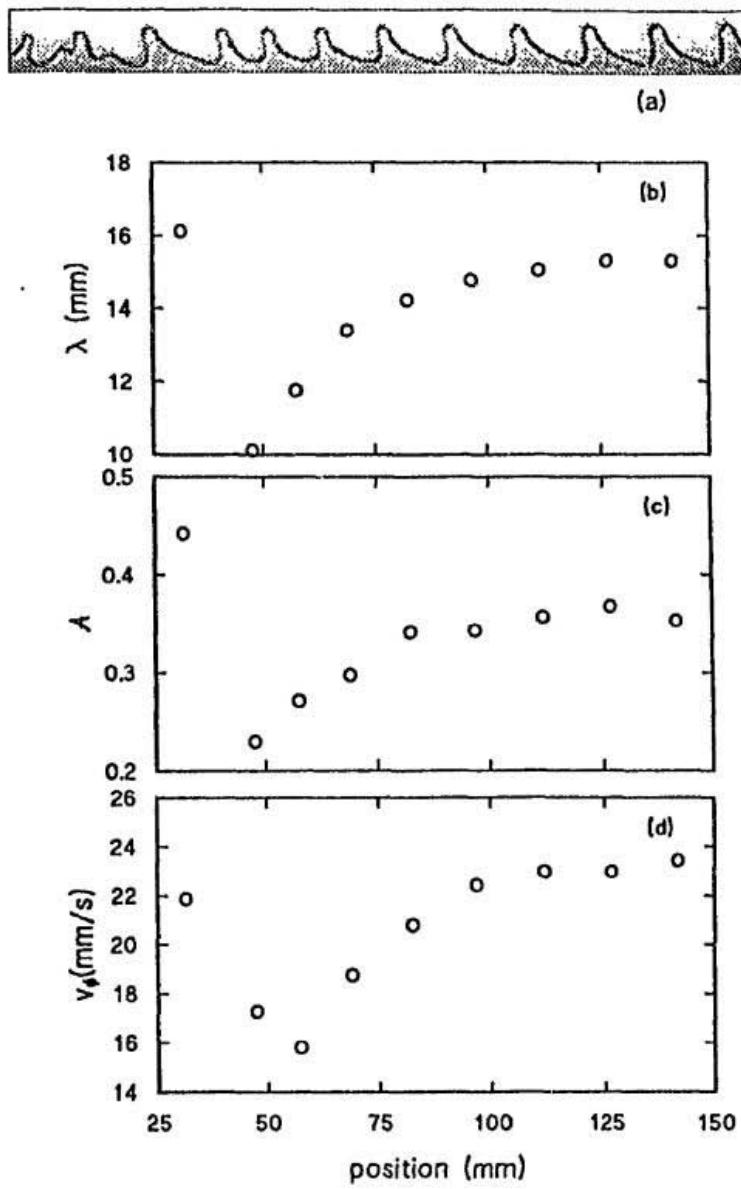

Figure 5.7: The variation of the local properties of a nonuniform traveling pattern, as a function of position, for $v_o = 261.4$ mm/s, $v_i = 55.42$ mm/s. (a) The pattern itself. (b) The local wavelength, λ. (c) The asymmetry of the fingers, $\mathcal{A}$. (d) The local traveling speed, v_ϕ.

which are reabsorbed if they are too close to its core; otherwise, they propagate away as a new finger. The new fingers initially move quickly, but slow down when they catch up with the rest of the drifting pattern. Once far enough (i.e., a few wavelengths) away from the source, the pattern's wavelength, speed and asymmetry all increase in a similar way, and appear to be saturating towards the end of the apparatus. Near a sink defect, the opposite behavior is observed: the pattern slows and becomes compressed, until a finger disappears into the sink. This behaviour is related to the Eckhaus instability of the pattern, which will be discussed below.

Fig. 5.8 is a plot of the square of the pattern's average phase speed against the control parameter, v_i, at $v_o = 174.3$ mm/s. v_ϕ^2 is linear in v_i at low v_i, in agreement with our results for the spatially uniform traveling pattern at low v_o: here the bifurcation to the broken-parity state occurs at $v_i = 0$ within our experimental resolution. The phase speed drops suddenly at a value of v_i between 15.83 mm/s and 17.42 mm/s. The drop in v_ϕ is accompanied by a drop in the pattern's wavelength as can be seen by comparing Fig. 5.5(d) ($v_i = 15.83$ mm/s) and Fig. 5.5(e) ($v_i = 17.42$ mm/s).

As v_o is increased, the wavelength-changing transition moves to higher values of v_i. It also becomes weaker and weaker, i.e., the magnitudes of the changes in average phase speed, wavelength, and asymmetry become smaller. At relatively high values of v_o, the transition disappears completely. At these high values of v_o, the transient bursts of disorder seen at lower v_o no longer occur, although defects can still exist in the pattern. Fig. 5.9 is a plot of v_ϕ^2 vs. v_i for $v_o = 436$ mm/s. In this case, the square of the phase speed increases linearly with v_i at low v_i, then smoothly decreases as the transition back to stationary fingers is approached. No sudden drop in v_ϕ is visible in the traveling-wave state.

The variation of wavelength along the pattern leads to the creation or annihila-

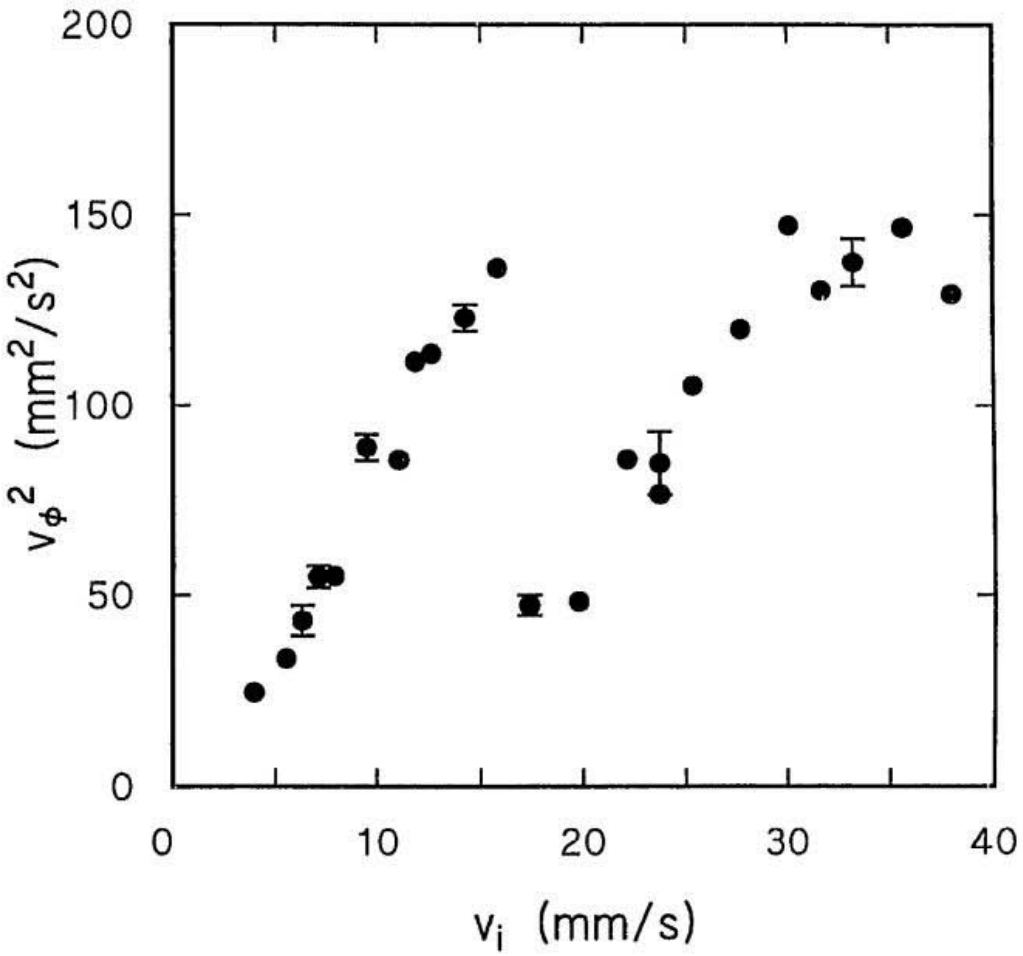

Figure 5.8: v_ϕ^2 as a function of v_i, for $v_o = 174.3$ mm/s.

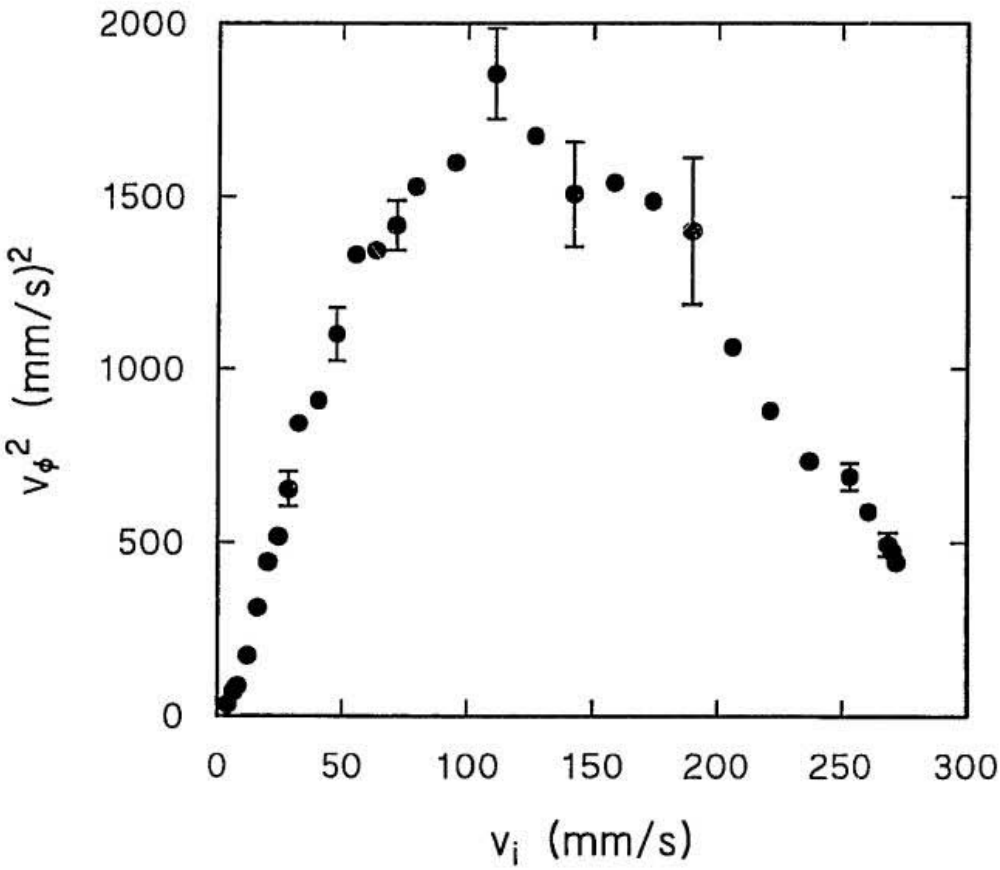

Figure 5.9: v_ϕ^2 as a function of v_i at $v_o = 435.7$ mm/s.

tion of fingers via the Eckhaus instability. As the fingers move away from a source, their local wavelength grows. When the wavelength becomes larger than a certain value, the fingers become unstable and ripples start to appear on the forward side (i.e., the less steeply sloped side) of the finger's base. Some of these can be seen in Fig. 5.5, for example at the right-hand side of Fig. 5.5(f). These ripples represent attempts to form of new fingers. Sometimes these attempts are unsuccessful: the ripple moves back towards, and is reabsorbed by, the parent finger. If the ripple initially develops far enough from the parent finger, however, it will grow and move away, forming a new, independent finger, and causing the local wavelength to decrease back into the stable range. New fingers develop at source defects in a similar way, as described above.

This process is illustrated in Figs. 5.10 and 5.11. Fig. 5.10 is a sequence of images of the interface for $v_o = 240$ mm/s and $v_i = 47.5$ mm/s. The pattern in this case is moving to the left. Initially (Fig. 5.10(a)), the fingers at the left-hand side of the front have a wavelength which is too large, and they are unstable. A new finger is trying to nucleate just in front of the finger labeled 1 in Fig. 5.10(a), but it is too close, and in Fig. 5.10(b) it is in the process of being reabsorbed by finger 1. Another attempt is made in Fig. 5.10(c), with the same result: the new finger is reabsorbed in Fig. 5.10(d). In Fig. 5.10(d), the finger labeled 2 has also become unstable, and a small ripple can be seen developing in front of that finger. Again the new finger is reabsorbed, as shown in Fig. 5.10(e) and (f). Finally, in Fig. 5.10(g), a new finger successfully forms; it can be seen moving away from its parent finger in Fig. 5.10(h-j). The time elapsed from the start to the end of Fig. 5.10 is 2.73 s.

Fig. 5.11 is a space-time representation of a similar sequence of events at $v_o = 174$ mm/s, $v_i = 22.2$ mm/s. The time from the top to the bottom of the figure is 13.5 s. As in the case discussed above, prior to the creation of the new finger, there are

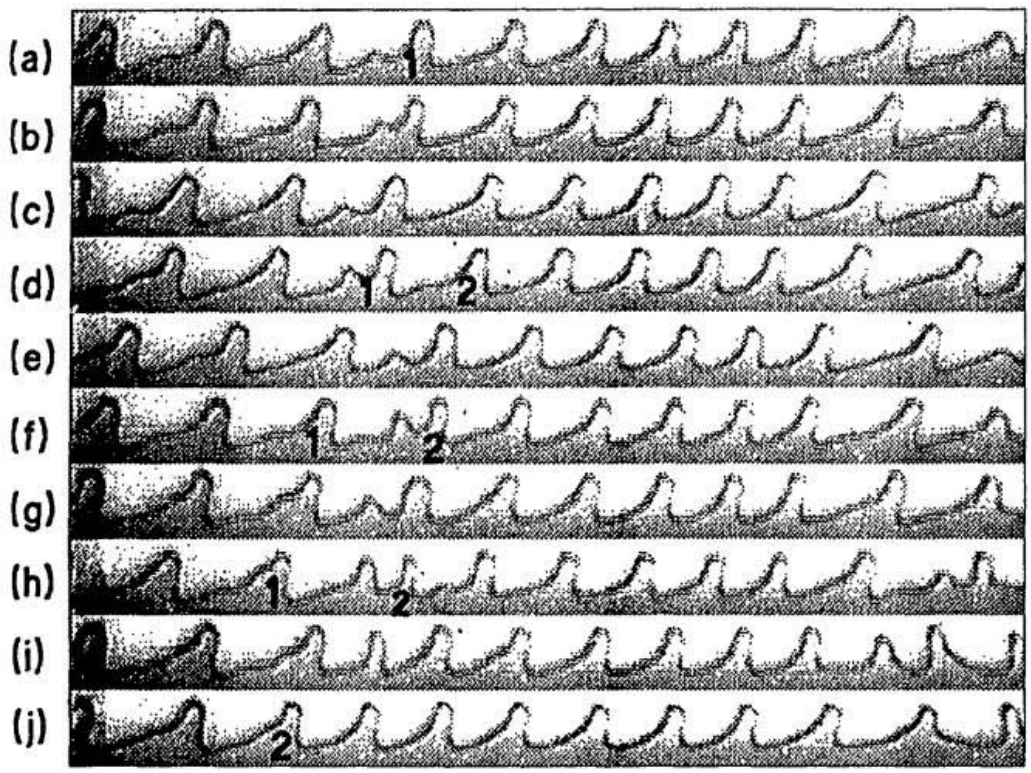

Figure 5.10: The formation of a new finger through Eckhaus instability. Here v_o = 239.6 mm/s and v_i = 47.50 mm/s. The images were recorded at times (a) 0 s; (b) 0.1 s; (c) 0.23 s; (d) 0.35 s; (e) 0.68 s; (f) 0.83 s; (g) 1.00 s; (h) 1.23 s; (i) 1.73 s; and (j) 2.73 s.

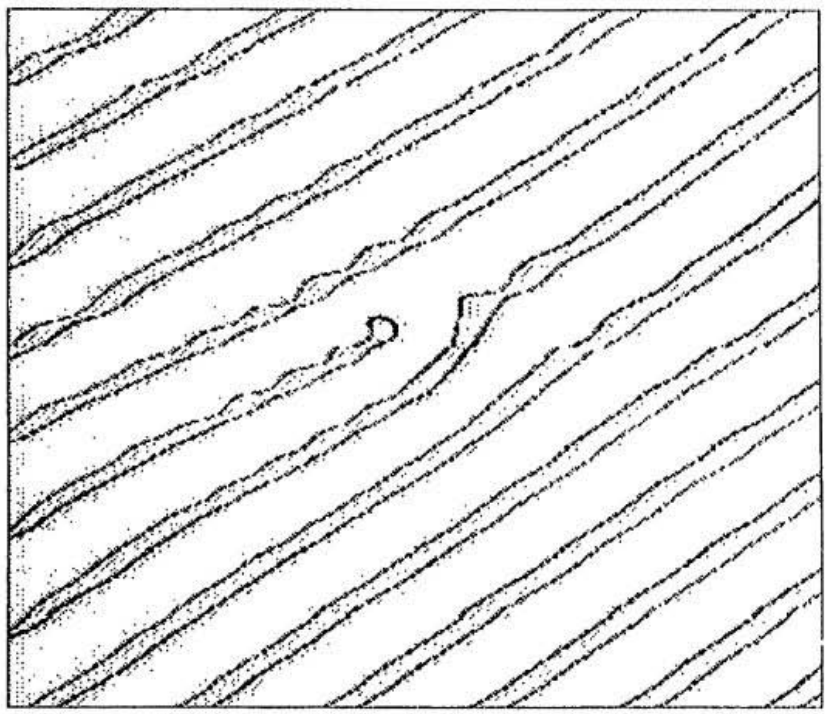

Figure 5.11: A space-time image of a drifting pattern showing the nucleation of a new finger. Here $v_o = 174$ mm/s, $v_i = 22.2$ mm/s. Time runs from the top down, and the total time is 13.5 s; 91.6 mm of the system length is shown.

several unsuccessful attempts, both on the eventual parent finger and its neighbors. These show up on the space-time picture as modulations in the widths of the fingers.

Observations of events such as these allow us to construct the Eckhaus stability boundary for broken-parity traveling waves in this system. We take the long-wavelength stability limit of the finger to be defined by the wavelength at which the ripples, which represent attempts to create new fingers, first appear. The short-wavelength limit is given by the shortest interfinger distance for which the two fingers do not recombine. The results of these measurements are shown in a plot of control parameter, v_i, against wavelength for three values of v_o in Fig. 5.12. The data points at $v_i = 0$ indicate the wave number of the stationary pattern there. Between $v_i = 0$ and the lowest v_i data point in the figure, the pattern was disordered and measurements of the Eckhaus boundary were not possible. The data for $v_o = 218$ mm/s (the circles) and $v_o = 261$ mm/s (the triangles) show a definite kink, most obvious on the low-wave-number side of the stability boundary. This kink coincides with the transition discussed above, at which the pattern's wavelength suddenly changes. The kink does not appear in data taken at high values of v_o (for example, the stars in Fig. 5.12), for which the transition does not occur. While the low-wavelength side of the boundary doesn't change much as v_o is varied, the high-wavelength side moves in and the stable region becomes more narrow as v_o is increased. The propagating pattern appears to select wavelengths near the long-wavelength stability boundary, and short wavelengths are only seen during creation or annihilation events.

5.2 Analysis and discussion

In this section, the experimental results on the broken-parity waves presented above will be analyzed and compared with theoretical predictions derived from both the symmetry arguments of Refs. [25-27], and the $q - 2q$ coupling model of Ref. [35].

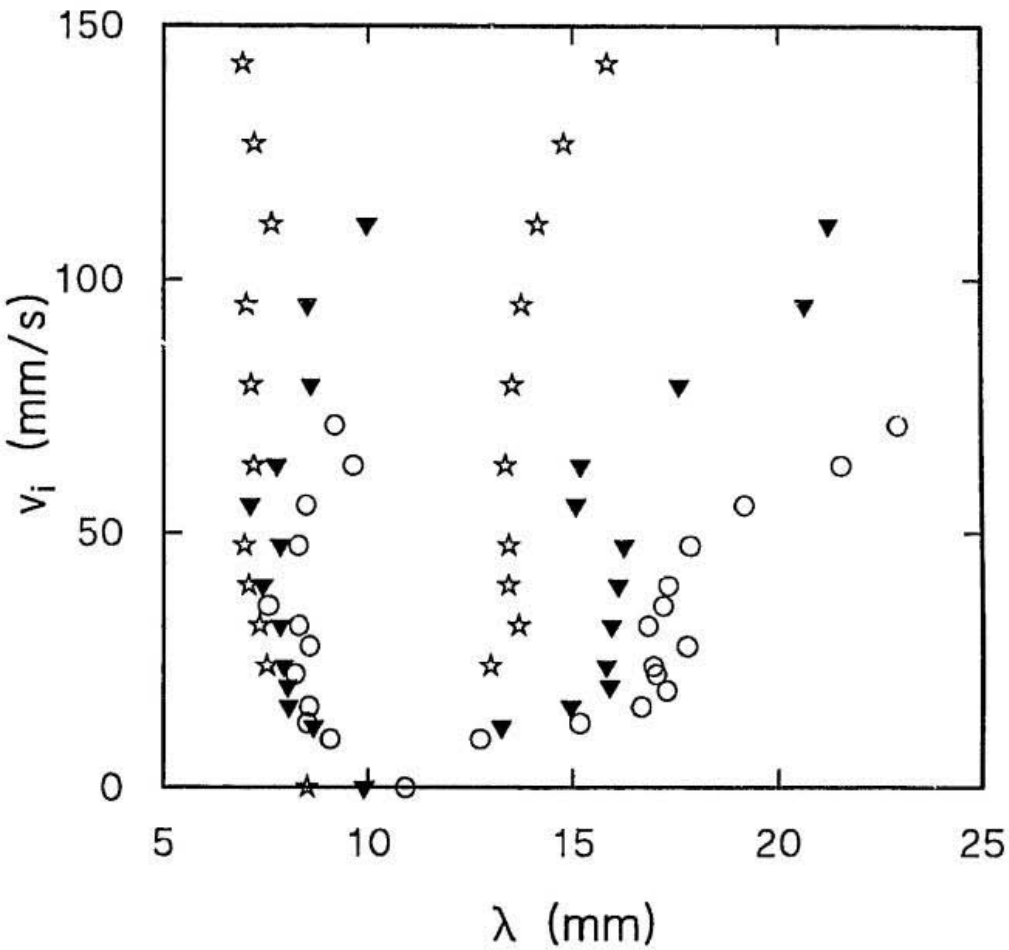

Figure 5.12: The measured Eckhaus stability boundary for traveling waves in our experiment, for three values of v_a. Outside the boundary the fingers become unstable, resulting in the creation of a new finger on the long-wavelength side, or in the loss of a finger on the short-wavelength side. Circles: $v_a = 218$ mm/s; triangles: $v_a = 261$ mm/s; stars: $v_a = 436$ mm/s.

The Eckhaus instability of the traveling waves we observed will be explained qualitatively using the complex Ginzburg-Landau equation.

5.2.1 Uniform traveling waves at low v_o

From the theory of Refs. [25, 26, 27], outlined in section 2.2.1 above, at a supercritical parity-breaking bifurcation from a stationary pattern to a uniform broken-parity state, the relationship among the asymmetry A, phase speed v_ϕ, and control parameter μ should be described by Eqs. (2.46) and (2.47):

$$A = \pm(\mu + c\phi_x)^{1/2}, \tag{5.2}$$

$$\phi_t = v_\phi = \omega A. \tag{5.3}$$

For the spatially uniform traveling wave state we observed at lower values of v_o, the patterns became more and more asymmetric as v_i was increased, as can be seen in Fig. 5.1. The increased asymmetry was accompanied by an increase in phase speed, as expected from Eq. (5.3). Also, since the phase speed should be linear in the asymmetry, the dependence of v_ϕ on v_i shown in Fig. 5.3 is roughly what one would expect from Eq. (5.2). To make the comparison more concrete, we must quantify the asymmetry of the pattern. According to Eq. (2.40), the function $U(x,t)$ giving the interface height as a function of position, x, is composed of symmetric and antisymmetric components. This function, expanded as a Fourier series at some particular time t, is

$$U(x) = \sum_{j=1}^{\infty} a_j \cos jqx + \sum_{j=1}^{\infty} b_j \sin jqx, \tag{5.4}$$

where q is the fundamental wave number of the pattern. There is a degree of freedom available to us through the definition of the point $x = 0$ (i.e., the point of zero phase). Since a pattern described by a perfect cosine wave should be perfectly

symmetric, we choose our zero point so that the coefficient $b_1 = 0$. Thus we consider the pattern to be of the form

$$U(x) = a_1 \cos qx + \sum_{j=2}^{\infty} a_j \cos jqx + \sum_{j=2}^{\infty} b_j \sin jqx. \tag{5.5}$$

For a symmetric pattern, all of the b_j should be equal to zero, while nonzero b_js imply a degree of asymmetry. The total power in the Fourier spectrum, which is independent of the above choice of phase, is equal to $\sum(a_j^2 + b_j^2)$. We define the asymmetry parameter $\mathcal{A}$ as

$$\mathcal{A} = \sqrt{\frac{\sum b_j^2}{\sum(a_j^2 + b_j^2)}}, \tag{5.6}$$

i.e., as the square root of the fraction of the total power contained in the antisymmetric terms. This parameter is linearly proportional to the asymmetry A of Eq. (2.40) for small asymmetries. This can be understood by considering an interface with $U(x) = a_1 \cos x + a_2 \cos 2x + b_2 \sin 2x$. For this interface, the asymmetry as defined by Eq. (5.6) is $\mathcal{A} = |b_2|/(a_1^2 + a_2^2 + b_2^2)^{1/2}$, which is proportional to the asymmetry $A = b_2$ defined by Eq. (2.40), as long as b_2 is small. Note that, because of the way $\mathcal{A}$ is defined, it can never be negative, and the sign of the asymmetry, if desired, has to be put in by hand.

The interface function $U(x)$ was obtained by having the computer automatically trace along the path of darkest pixels of a video image, from a given starting point. Each individual finger in the pattern was then Fourier transformed and the coefficients a_j and b_j of Eq. (5.4) were obtained. To locate the point $x = 0$ such that the coefficient $b_1 = 0$, we apply the translation

$$qx = qx' + \phi, \tag{5.7}$$

in Eq. (5.4), where $\tan\phi = b_1/a_1$. After this translation, the interface equation $U(x')$ can be described by Eq. (5.5) with the coefficients equal to

$$a_j' = a_j \cos j\phi + b_j \sin j\phi, \tag{5.8}$$

$$b'_j = -a_j \sin j\phi + b_j \cos j\phi, \tag{5.9}$$

and $b'_1 = 0$. After dropping the primes on x', a'_j and b'_j, we get Eq. (5.5), and can then calculate $\mathcal{A}$ using Eq. (5.6).

Sample results of this procedure are shown in Fig. 5.13. Each measurement has been averaged over roughly five fingers in the center part of the pattern. The fingers were in general quite anharmonic in shape, and we used up to 40 spatial modes to describe the interface to single-pixel accuracy. Fig. 5.13(a) shows the first ten Fourier sine and cosine coefficients for the stationary symmetric pattern of Fig. 5.1(a). In this case, the b_j are all close to zero and the asymmetry parameter is $\mathcal{A} = 0.02 \pm 0.03$. Fig. 5.13(b) shows the same coefficients for the propagating pattern of Fig. 5.1(c). Here the pattern is clearly asymmetric. As expected, the contributions of the sine terms to $U(x)$ are significant in this case, with the $2q$ component being strongest. This pattern has $\mathcal{A} = 0.35 \pm 0.03$. We performed this analysis on all of the patterns represented in the data of Fig. 5.3. Fig. 5.14 is a plot of $\mathcal{A}^2$ vs. v_i, and shows that $\mathcal{A}^2$ grows linearly from zero above a critical velocity.

Eq. (5.2), however, also includes a term $\epsilon\phi_x$. We performed a least-squares fit to the data of Fig. 5.14, using Eq. (5.2) as a fitting function, with $\mu = v_i - v_i^*$, and using our measurements of the pattern's wavenumber to determine ϕ_x. The fit gave $\epsilon = 0.2 \pm 1.6$, i.e., ϵ was equal to zero within our uncertainty. Using $\epsilon = 0.2$, we found that the term $\epsilon\phi_x$ contributed roughly 2% to the right-hand side of Eq. (2.46), much less than the uncertainty in $\mathcal{A}$. We therefore neglect this term, and fit the asymmetry data to a square root law in the rotation speed v_i. We find $v_i^* = 3.9 \pm 0.7$ mm/s, in agreement with the value found from the data of Fig. 5.3, and

$$\mathcal{A}^2 = (0.0129 \pm 0.0007)\,(v_i - (3.9 \pm 0.7))\,, \tag{5.10}$$

with v_i in units of mm/s. Thus the asymmetry increases continuously from zero with a square root dependence on the experimental control parameter v_i, as expected at

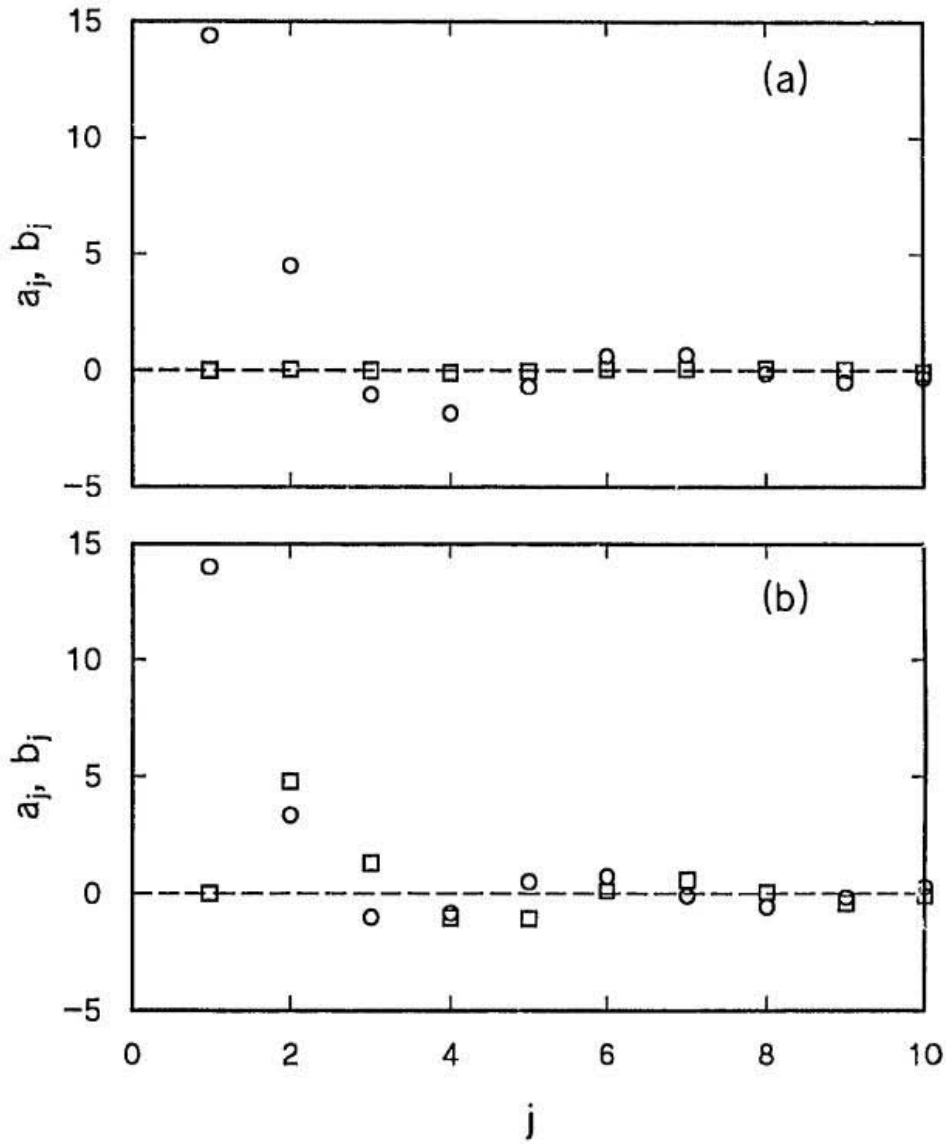

Figure 5.13: Fourier amplitudes obtained from Fourier transforms of (a) the stationary pattern of Fig. 5.1(a), and (b) the drifting pattern of Fig. 5.1(e). The circles and squares indicate the amplitudes of the even and odd contributions, respectively.

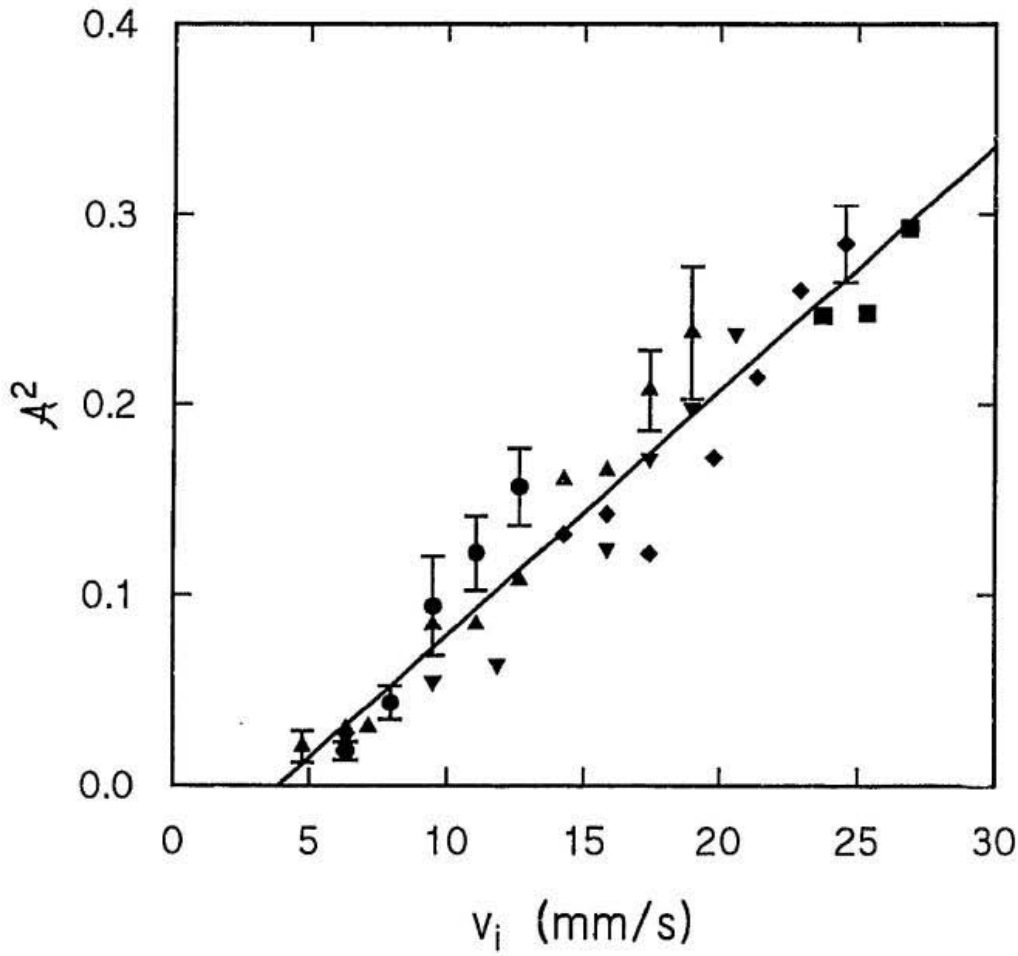

Figure 5.14: The square of the asymmetry parameter, $\mathcal{A}^2$, as a function of v_i, for the same patterns as in Fig. 5.3. The symbols are as defined in Fig. 5.3, and the line is a fit to the data.

a supercritical bifurcation.

Fig. 5.15 is a plot of phase speed as a function of $\mathcal{A}$. v_ϕ is linear in $\mathcal{A}$ over the entire range of existence of the traveling-wave state. Fitting of the data gives

$$v_\phi = (0.5 \pm 0.3) + (17.4 \pm 0.8)\mathcal{A}, \tag{5.11}$$

with v_ϕ in units of mm/s. The intercept in Eq. (5.11) may not be significantly different from zero, but we note that an intercept could arise due to a nonzero ϕ_{xx} term in Eq. (2.44) if the pattern were not perfectly uniform as a result of, for example, small imperfections in the experimental apparatus.

These results agree with the theoretical expectations for a supercritical parity-breaking bifurcation. The pattern's asymmetry increases with a square root dependence on the control parameter, and the pattern's phase speed is linear in the asymmetry.

We now consider our results in terms of the $q - 2q$-coupling model, in which interactions between spatial modes in the pattern with wave numbers q and $2q$ lead to the parity-breaking bifurcation. In this context it is useful to investigate the behavior of the spatial modes of the pattern as the control parameter is increased. Fig. 5.16 presents this data for $v_o = 143.8$ mm/s. Fig. 5.16(a) is a plot of the Fourier amplitudes of the first four even components of the pattern, i.e., a_1, a_2, a_3, and a_4 as a function of v_i, and Fig. 5.16(b) is a plot of the Fourier amplitudes of the odd components, b_2, b_3, and b_4 (recall that b_1 is set equal to zero). Finally, Fig. 5.16(c) shows the total amplitude of each mode, $(a_j^2 + b_j^2)^{1/2}$ for $j = 1, 2, 3, 4$. In all cases the amplitudes have been normalized by the quantity P, where $P^2 = \Sigma(a_i^2 + b_i^2)$ is the total power in the pattern's spatial Fourier spectrum. Some general trends can be seen. As v_i is increased, the power of the fundamental decreases, but the power in at least the second and third harmonics increases. In the case of the second harmonic in particular, it can be seen that a phase shift develops relative to the fundamental:

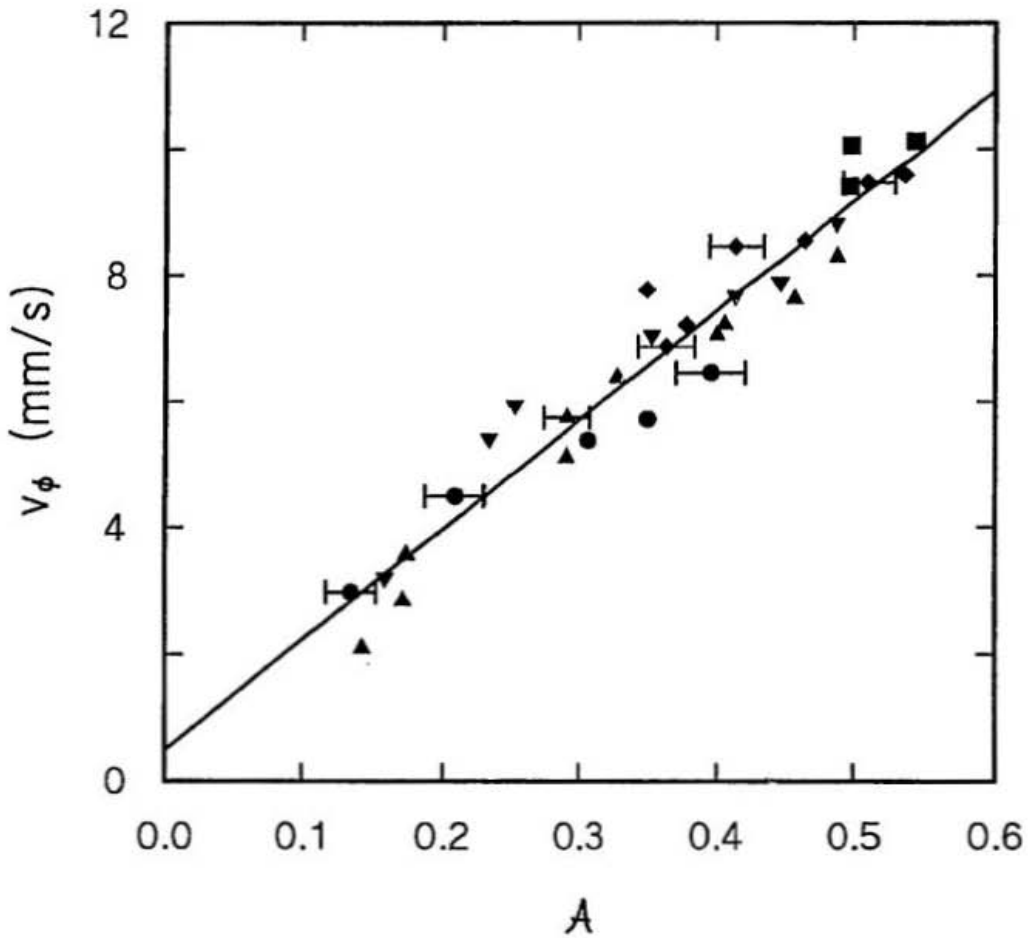

Figure 5.15: The pattern's phase velocity as a function of its asymmetry for uniform traveling waves. The symbols are as defined in Fig. 5.3, and the line is a fit to the data.

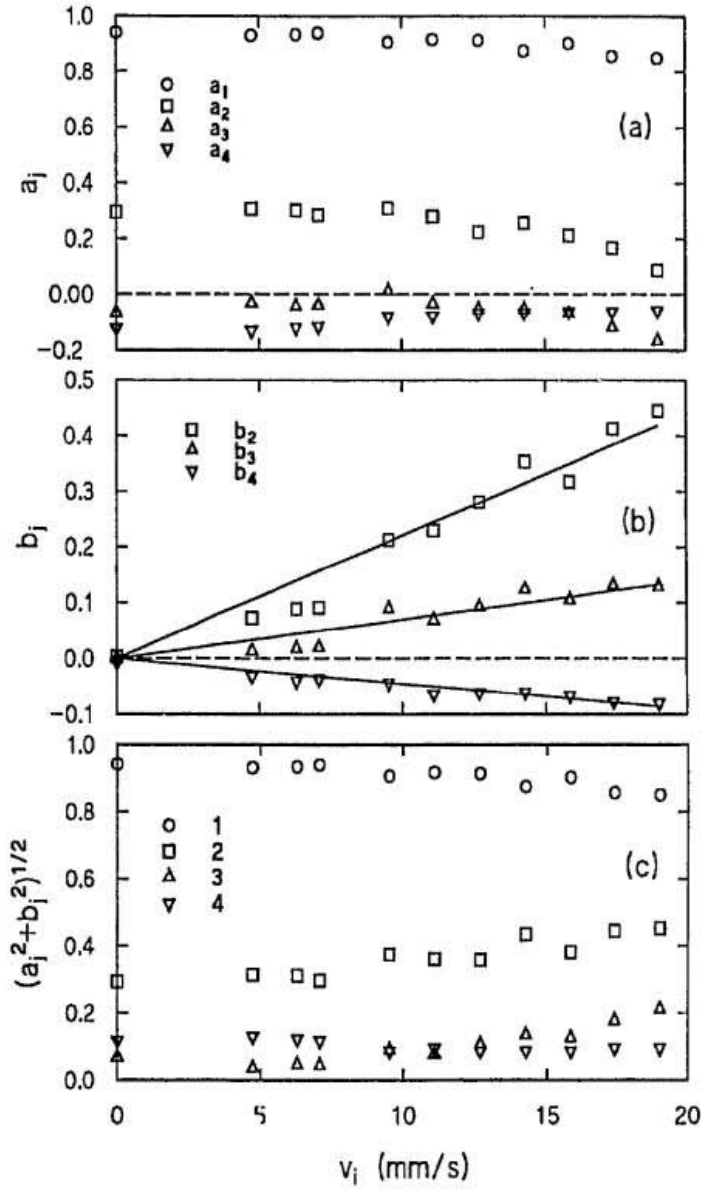

Figure 5.16: The first few Fourier sine and cosine amplitudes of the pattern as a function of the control parameter, a_i. All amplitudes have been normalized by the square root of the total spectral power in the pattern. (a) Cosine amplitudes, a_j; (b) sine amplitudes, b_j; (c) total mode amplitudes.

the amplitude of the $\cos(2qx)$ term steadily decreases while that of the $\sin(2qx)$ term increases. The amplitudes of the first three sine terms in the Fourier series increase linearly with v_i; the slopes of lines through the origin and fitted to the three data sets shown in Fig. 5.16(b) are, 0.0220 ± 0.0009, 0.0070 ± 0.0005, and -0.0045 ± 0.0002 for the second, third and fourth harmonics, respectively, in units of $(\mathrm{mm/s})^{-1}$.

According to Ref. [35], in a uniform traveling-wave state, the amplitude of the first harmonic (R) of the pattern and that of the second harmonic (S) are such that $R^2 = 2S^2$, as described in Eq. (2.55) in Chapter 2. The (normalized) amplitude of the second harmonic, $(a_2^2+b_2^2)^{1/2}$, is plotted against that of the first, a_1, in Fig. 5.17. The two amplitudes do not have the predicted constant ratio. Rather the growth of the $2q$ mode is accompanied by a linear decrease in the strength of the q mode.

The order parameter of the parity-breaking in the $q-2q$ model is the phase mismatch, $\Sigma = 2\phi - \theta$, as defined in section 2.2.2. Here ϕ is the phase of the q mode and θ the phase of the $2q$ mode. In our analysis, we fix $\phi = 0$ by our choice of origin. Neglecting the effects of higher spatial modes, the order parameter in our case will thus simply be equal to

$$\theta = \tan^{-1}(b_2/a_2), \tag{5.12}$$

since the algebraic sign of the order parameter is unimportant. In the $q-2q$ model, the parity-breaking bifurcation is supercritical [35], and so the order parameter should grow like the square root of the control parameter near the onset. Our data for θ are plotted in Fig. 5.18, as a function of our control parameter v_i. Within the experimental scatter, the relationship is linear, but the best straight-line fit to the data passes through $\theta = 0$ at a value of v_i somewhat lower than v_i^*. From our data, we cannot rule out a square root growth of the order parameter very close to the parity-breaking bifurcation (i.e., closer to the bifurcation than our closest data

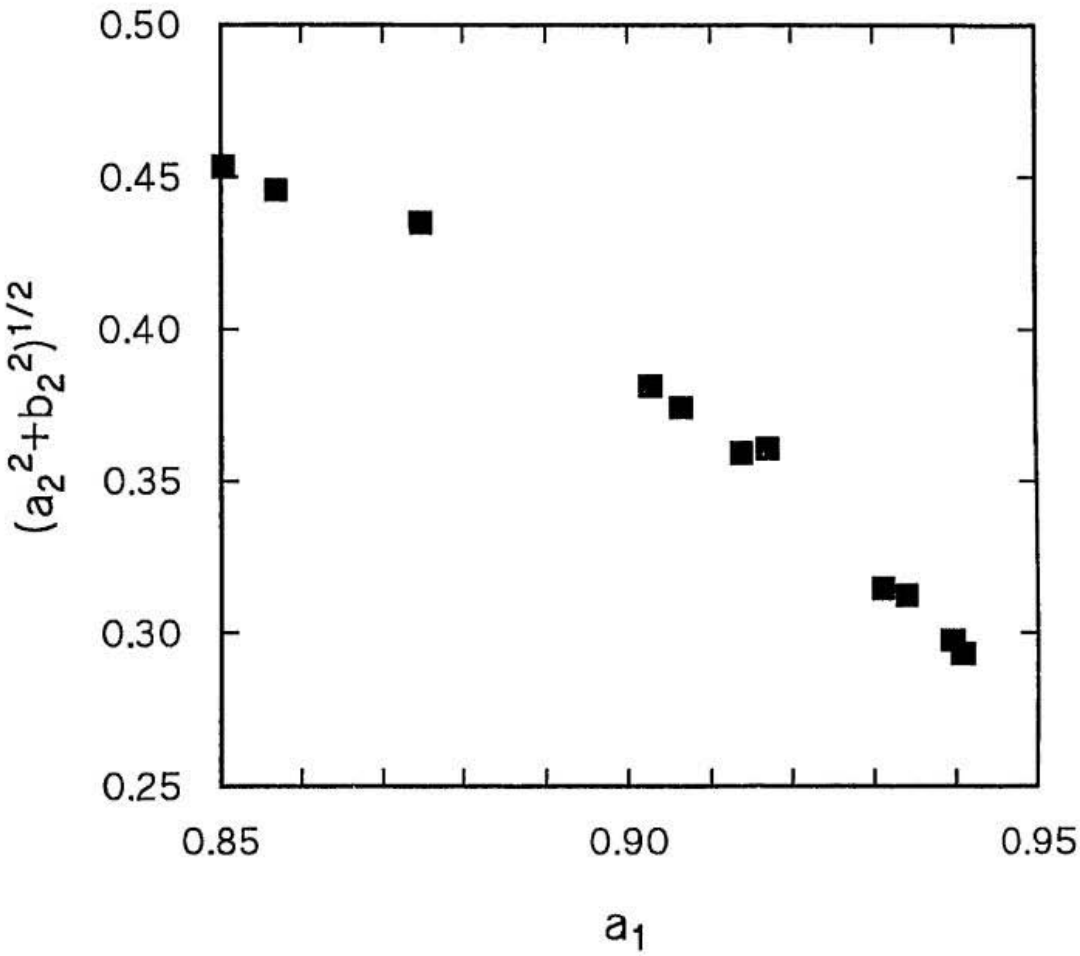

Figure 5.17: The total amplitude of the second spatial harmonic, $(a_2^2+b_2^2)^{1/2}$, plotted against that of the fundamental, a_1. The amplitudes are normalized as in Fig. 5.16. An increase in the strength of the second harmonic is accompanied by a decrease in that of the fundamental.

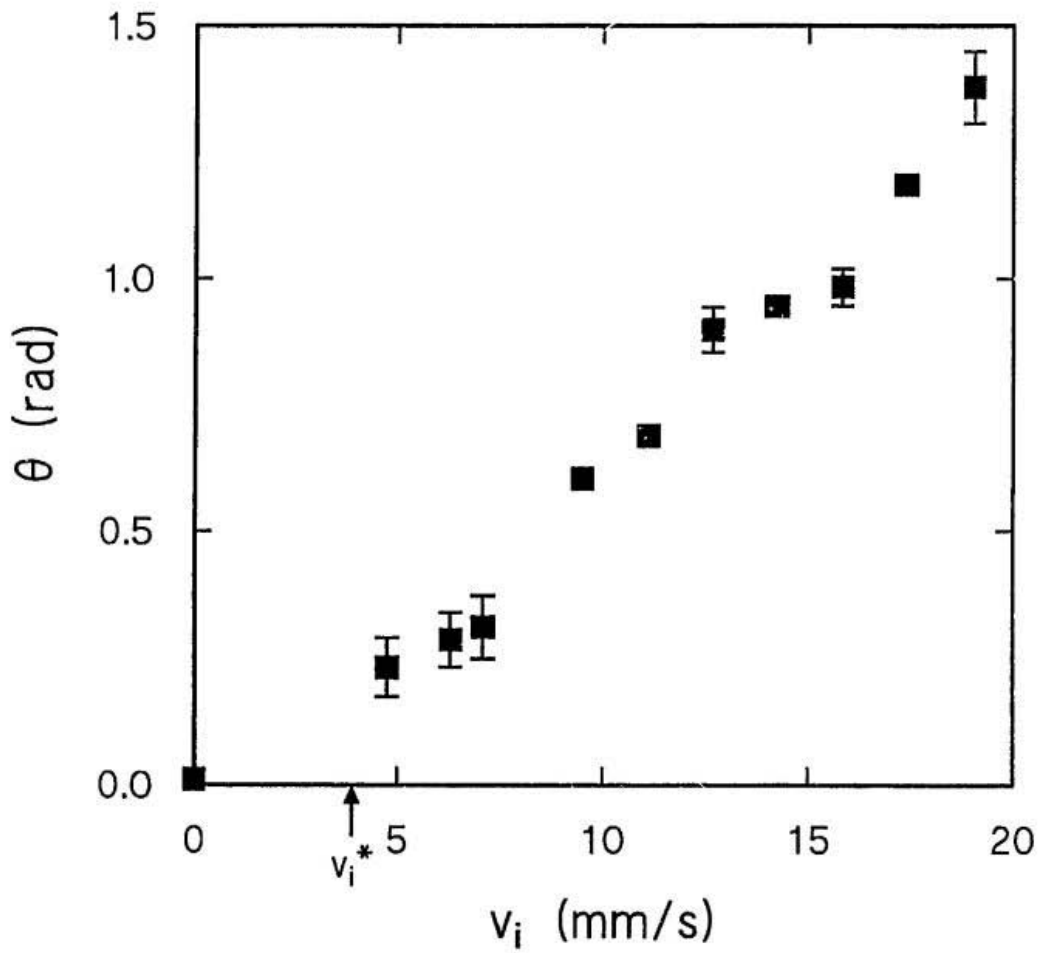

Figure 5.18: The phase mismatch angle θ as a function of the control parameter v_i. The $q - 2q$ model predicts a square-root relationship.

point), which would imply an onset closer to v_i^*, but nor do we see any evidence for this in our data.

Finally, the relationship between phase speed and order parameter is $v_\phi = S \sin \Sigma / q$, from Eq. (2.57). Putting this in terms of the quantities extracted from the analysis of our data, we get for the pattern's phase velocity

$$v_\phi = \frac{S}{q} \sin \Sigma = \frac{(a_2^2 + b_2^2)^{1/2}}{2q} \sin \theta = b_2 / 2q, \tag{5.13}$$

since $S = (a_2^2 + b_2^2)^{1/2}/2$. We have plotted the phase speed as a function of b_2/q in Fig. 5.19; as before b_2 has been normalized by the quantity P. Bearing in mind that the data should go through the origin, we do not find the expected linear relationship. Rather, v_ϕ grows more slowly than linearly with b_2/q. Actually, if we neglect the variation in wavenumber with v_i, then, since $v_\phi \propto v_i^{1/2}$, while b_2 was found to grow linearly with v_i, we expect to find $v_\phi \propto b_2^{1/2}$. Indeed, the data in Fig. 5.19 are well described by a square root function.

It is clear that the predictions of the $q - 2q$ model are contradicted by our experimental results. It is possible that our disagreement with the model comes about because there are more than just two modes with significant strength in our patterns. As Fig. 5.16(c) shows, the third and fourth harmonics have amplitudes on the order of 10-20% of the fundamental. Cummins et al. [84] argued that their results on the sequence of bifurcations observed in their experiments on this system could not be explained using only two modes, but that at least three coupled modes were necessary. Our results are consistent with this.

Another possibility is that the $q - 2q$ model in fact does apply to our system, but only very close to the bifurcation. In the experimentally accessible region above the transition, corrections to this mode — presumably incorporating the effects of more spatial modes, as above — would have to be considered. If this were the case, one would expect the linear growth of θ with v_i, shown in Fig. 5.18, to turn in to a

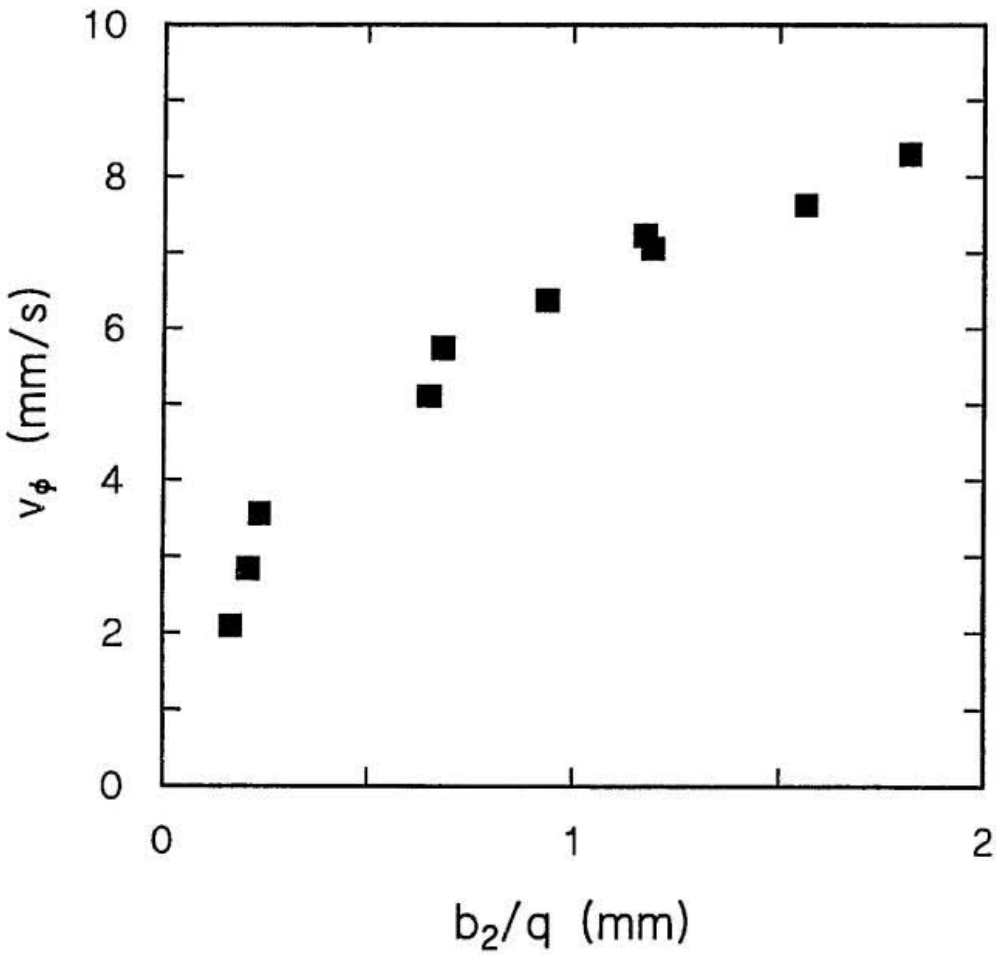

Figure 5.19: The pattern's phase velocity plotted against the quantity b_2/q.

square root behaviour close to the transition, and we cannot rule this out from our data.

Finally, it is conceivable that our parity-breaking bifurcation could result from a completely different, and as yet uninvestigated, mechanism, unrelated to mode-coupling. In this case, since the theory based on symmetry arguments [25, 26, 27] makes no assumptions about the cause of the parity breaking, its predictions would still be valid, but those specific to the $q - 2q$ model would not. It is worth emphasizing, however, that $q - 2q$ coupling has been used to explain the parity-breaking instabilities observed in the directional cooling of nematics [37, 38] and in Taylor vortex flow [39]. A bifurcation analysis of the equations of motion for the printer's instability would help to resolve this issue.

5.2.2 Nonuniform traveling-wave state

The analysis above is focussed on the uniform traveling wave, which exists when v_a is relatively low. When v_a is above 157 mm/s, nonuniform patterns are observed, as shown in Fig. 5.5. At relatively high values of v_a, the fingers of the pattern lean over sufficiently far that $U(x)$ is not single valued, as can be seen in Fig. 5.5, and so can not be directly Fourier transformed. To determine the asymmetry of a multiple-valued pattern, an extra step must be added to the procedure described in the previous section. Consider the parameter l, which measures the length of the curve defined by the interface. In contrast to $U(x)$, the function $U(l)$, i.e., the height of the finger as a function of the distance measured along the interface, is always single-valued. An example is shown in Fig. 5.20(c) which shows the function $U(l)$, transformed from a multiple-valued function $U(x)$ for Fig. 5.5(c). We then write

$$U(l) = \sum_{j=1}^{\infty} a'_j \cos jq'l + \sum_{j=1}^{\infty} b'_j \sin jq'l, \tag{5.14}$$

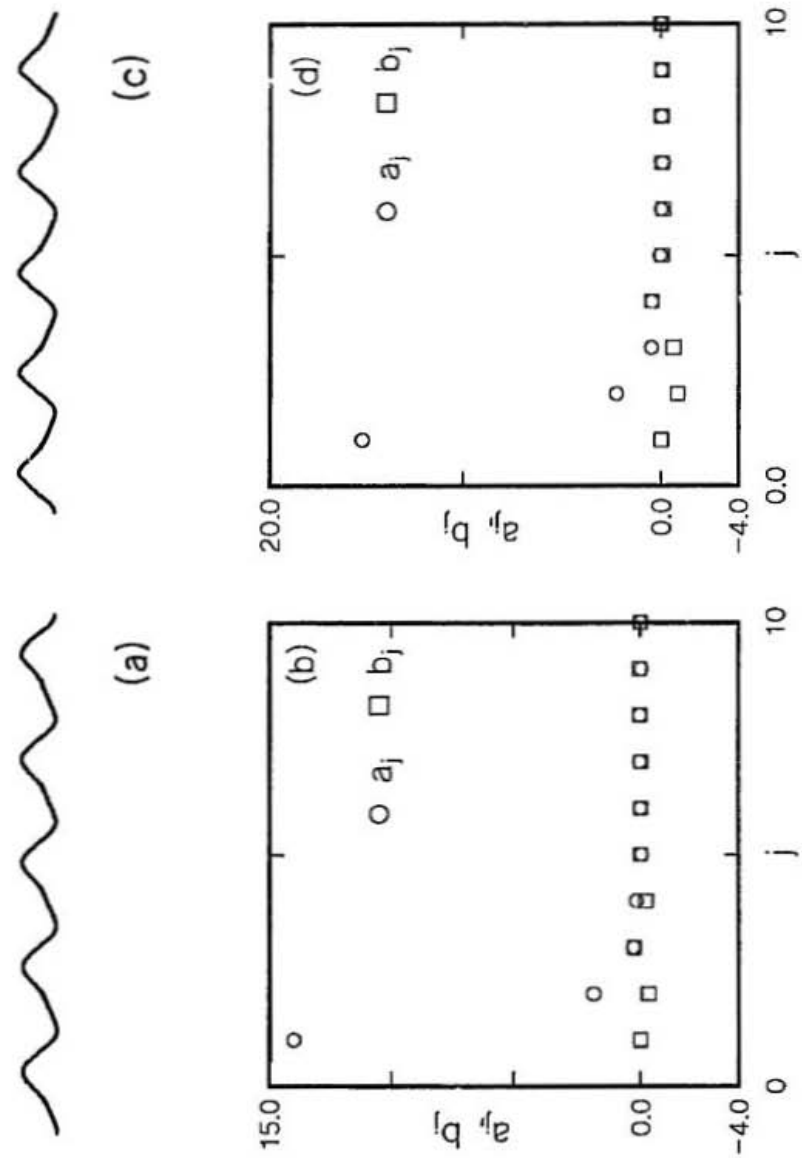

Figure 5.20: (a) The pattern of Figure 5.1(e) transformed into a function $U(l)$ of the length along the interface. (b) The Fourier amplitudes of the transformed pattern. (c) The multiple-valued interface pattern of Figure 5.5(c) transformed as in (a). (d) The Fourier amplitudes of the transformed pattern.

with q' being a new wavenumber given by

$$q' = \int_0^q \sqrt{\frac{d^2U(x)}{dx^2} + 1}\ dx. \tag{5.15}$$

As in the single-valued case, we set the coefficient b_1' equal to zero. We then define a modified asymmetry parameter $\mathcal{A}'$, in analogy to Eq. (5.6), by

$$\mathcal{A}' = \sqrt{\frac{\sum b_j'^2}{\sum (a_j'^2 + b_j'^2)}}. \tag{5.16}$$

Fig. 5.20 shows the results of using this procedure on the single-valued pattern shown in Fig. 5.1(c), and also on the multiple-valued pattern shown in Fig. 5.5(c). Fig. 5.20(a) and (b) show the transformed function $U(l)$ and its Fourier amplitudes for the single-valued pattern, which has $\mathcal{A}' = 0.18 \pm 0.02$. Fig. 5.20(c) and (d) show the same results for the multiple-valued function, which has $\mathcal{A}' = 0.17 \pm 0.02$. The Fourier amplitudes calculated from $U(x)$ for the single-valued pattern have been shown in Fig. 5.13(b), and give an asymmetry $\mathcal{A} = 0.35 \pm 0.03$.

To determine the relationship between $\mathcal{A}'$ and $\mathcal{A}$, we calculated both $\mathcal{A}$ and $\mathcal{A}'$ for all of the data shown in Fig. 5.14. The results are shown in Fig. 5.21. We fit the data to a power law, $\mathcal{A} = a\mathcal{A}'^n$, and found $a = 1.01 \pm 0.03$, and $n = 0.62 \pm 0.02$. Using this relationship, we can get the asymmetry $\mathcal{A}$ from measurements of $\mathcal{A}'$ for multiple-valued patterns.

We also modeled the interface by an equation

$$U(x) = a_1 \cos x + a_2 \cos 2x + b_2 \sin 2x, \tag{5.17}$$

with a_1 chosen to be 15, and a_2 to be 3, 4, and 5. These values are around those of the corresponding Fourier coefficients obtained from the patterns. We then calculated the two asymmetry parameters, $\mathcal{A}$ and $\mathcal{A}'$ of this model pattern, with values of b_2 from 1 to 30. Fig. 5.22 is the plot of the result, which is similar in general appearance to Fig. 5.21.

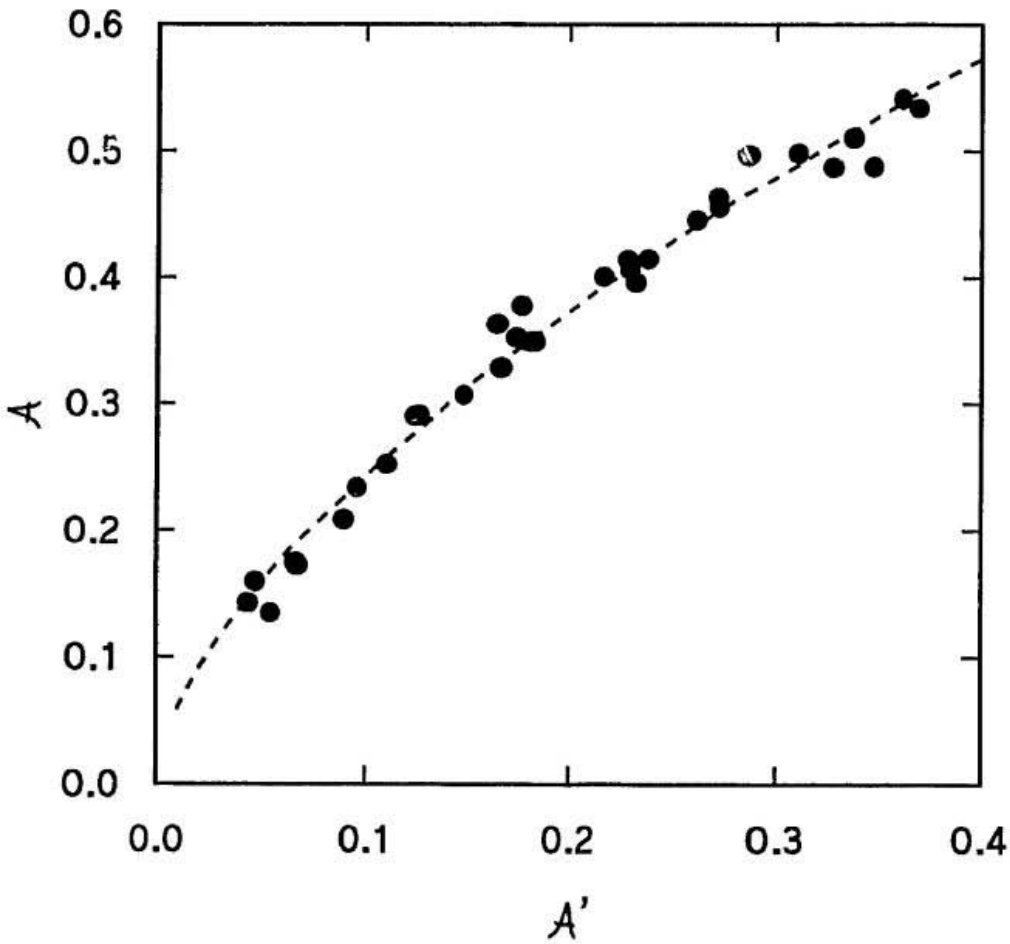

Figure 5.21: A plot of the two asymmetry parameters, $\mathcal{A}'$ vs. $\mathcal{A}$, determined from single-valued patterns at relatively low value of v_o. The line is a fit and with $\mathcal{A} = 1.01\mathcal{A}'^{0.62}$.

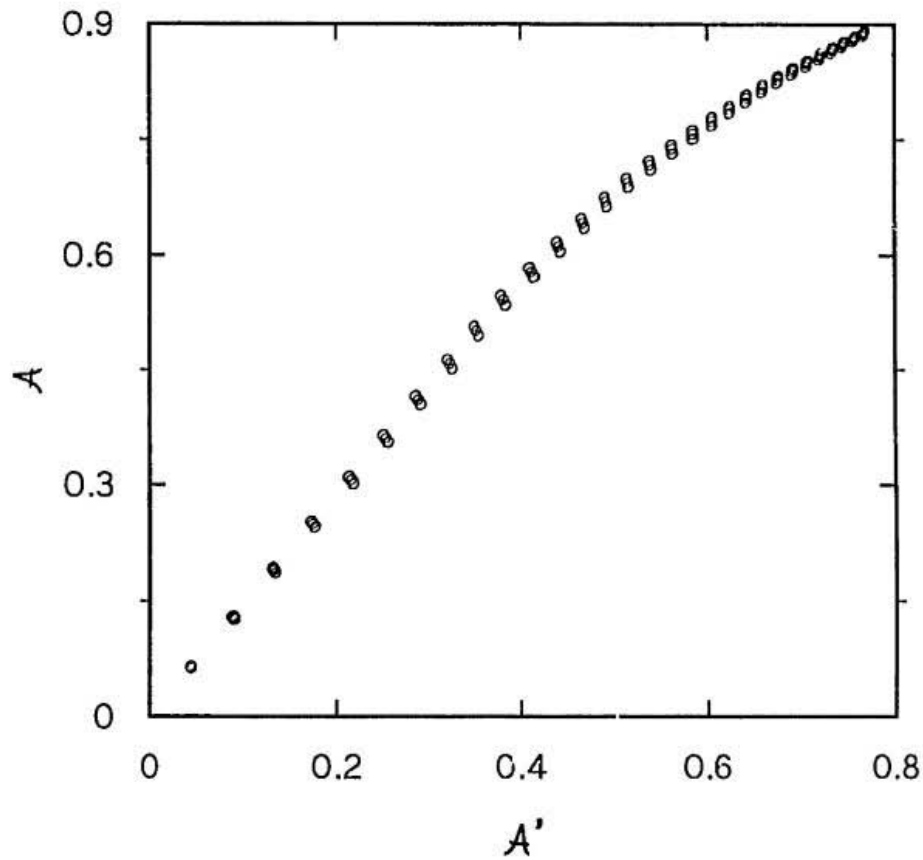

Figure 5.22: A plot of the two asymmetry parameters, $\mathcal{A}'$ vs. $\mathcal{A}$, calculated from simulated interface patterns as discussed in the text. The data sets from top to bottom have $a_2 = 3$, $a_2 = 4$, and $a_2 = 5$.

In the following, we will present our results in terms of the parameter $\mathcal{A}$ for consistency with the previous section. In Fig. 5.23, we plot the averaged asymmetry $\mathcal{A}$ as a function of control parameter v_i for the same case as in Fig. 5.8. As can be seen, the asymmetry drops at the same point at which the phase speed drops. Thus in a plot of v_ϕ vs. $\mathcal{A}$, Fig. 5.24, no sign of this transition is seen: the data from above and below the jump fall on the same continuous curve. v_ϕ is linear in $\mathcal{A}$ at low asymmetry, as found for the spatially uniform patterns, but in contrast to what was found in that case, the linearity no longer persists over the whole range of existence of the traveling state.

We also measured the instantaneous speed, the asymmetry and the wavelength of each individual finger for the nonuniform traveling pattern. Fig. 5.25(a) is a plot of phase speed vs. asymmetry for the individual fingers in the pattern shown in Fig. 5.7(a), as well as for fingers from patterns with two other values of the cylinder speeds. The fingers in the pattern display a linear dependence of phase speed on asymmetry, as did the uniform traveling waves. Straight-line fits to these data sets have intercepts equal to zero within error, indicating that, even for these patterns where the wavelength is not constant, the ϕ_{xx} term in Eq. (2.44) is small. The slope of the the v_ϕ vs $\mathcal{A}$ graph is the parameter ω of Eq. (2.44). In Fig. 5.25(b), ω is plotted as a function of v_o. It includes a point from the data plotted in Fig. 5.15, for the uniform traveling-wave case. Fig. 5.25(b) indicates that ω is proportional to $v_o - v_{o_c}$, where v_{o_c} is the value of v_o at which the stationary finger pattern appears when $v_i = 0$. A fit to the data, shown in the figure as a dashed line, gives $\omega = (0.40 \pm 0.03)(v_o - v_{o_c})$, with $v_{o_c} = 108.7 \pm 9.4$ mm/s from the fitting, in agreement with the measured value of $v_{o_c} = 111.5 \pm 2.5$ mm/s.

The range of v_i over which the uniform traveling-wave state is unstable is proportional to ω as described in Eq. (2.99), and ω increases linearly with v_o. One

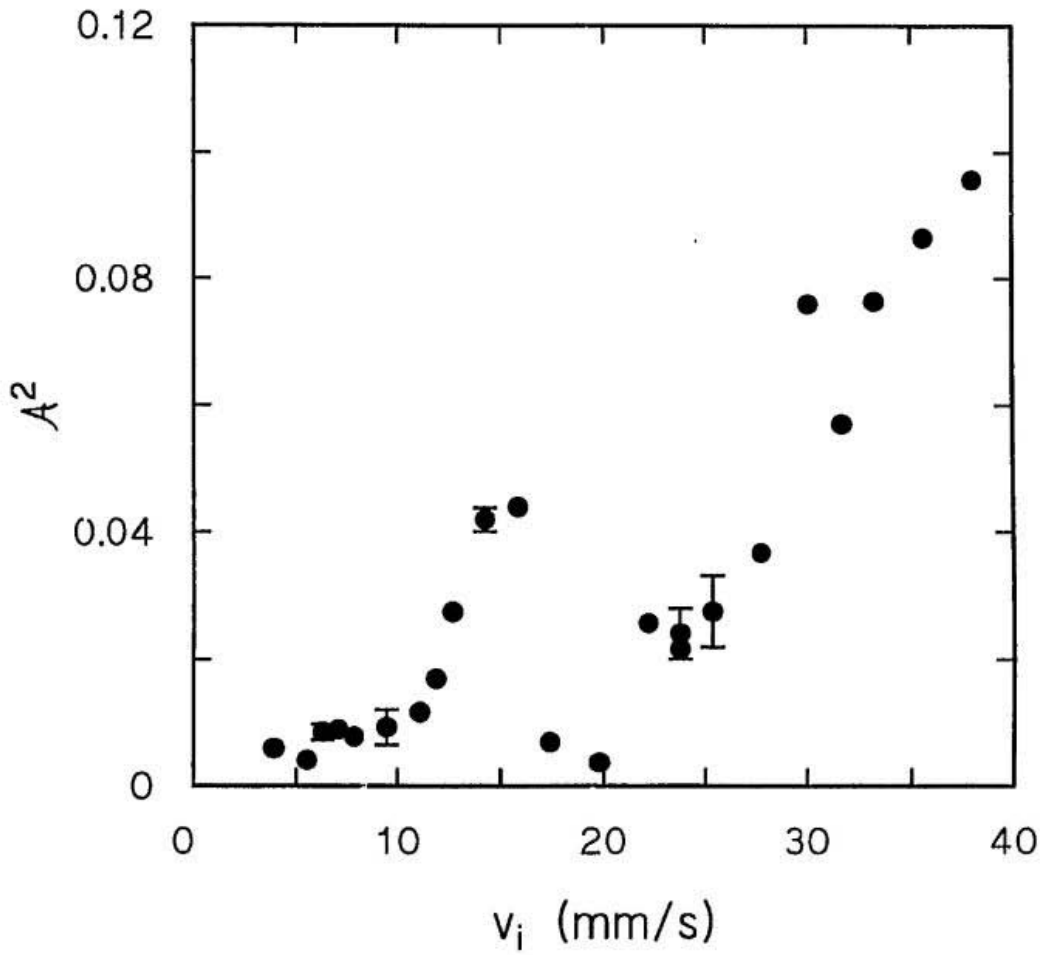

Figure 5.23: $\mathcal{A}^2$ plotted against v_i at $v_o = 174.3$ mm/s.

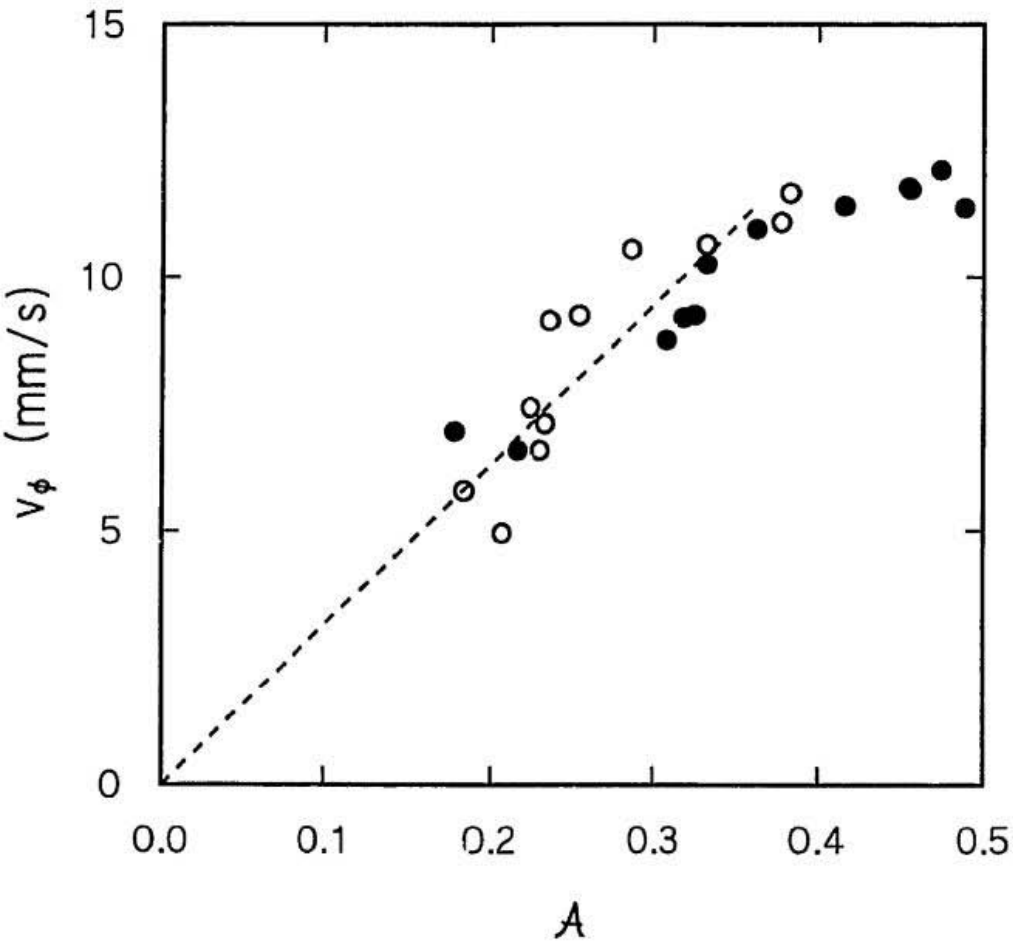

Figure 5.24: Traveling speed, v_ϕ, as a function of asymmetry at $v_o = 174.3$ mm/s. The open and solid symbols indicate data from below and above the transition at $v_i \approx 16$ mm/s, respectively.

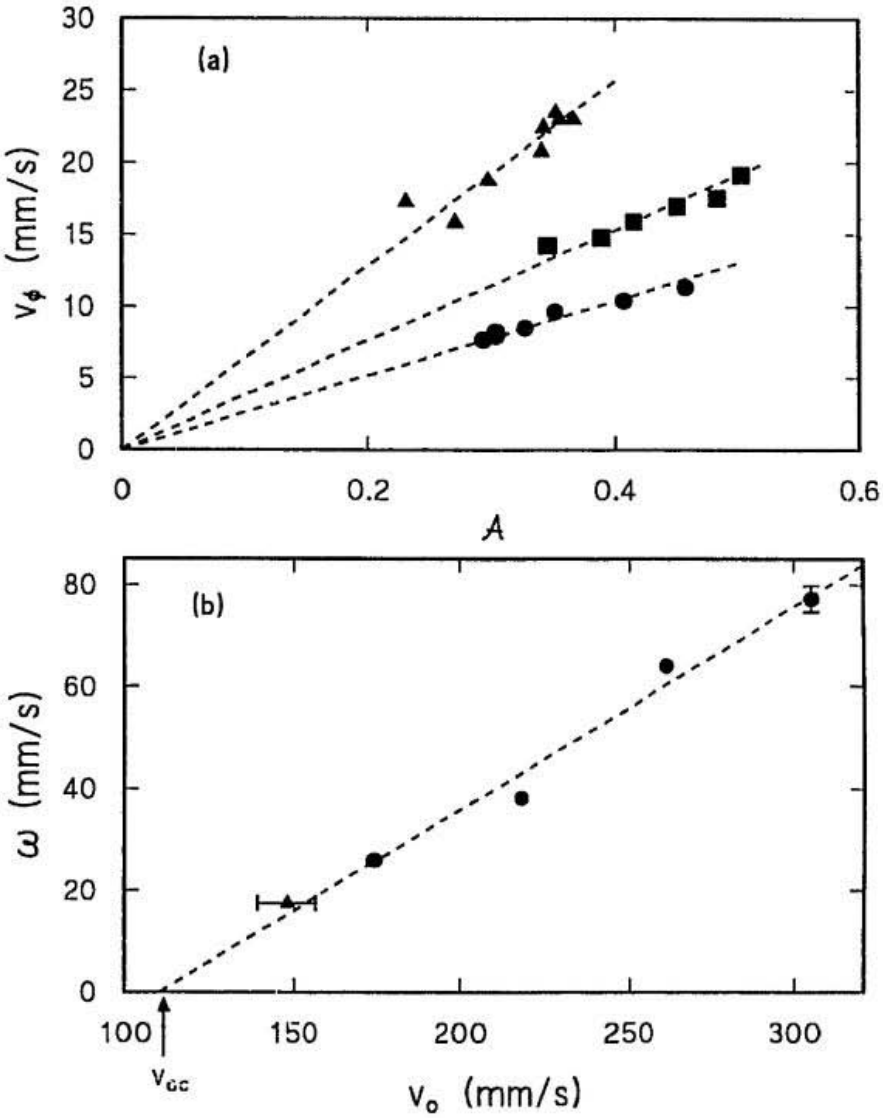

Figure 5.25: (a) The phase speed plotted against asymmetry for each finger in three nonuniform pattern at different cylinder speeds. Circles: v_o = 174.3 mm/s, v_i = 23.75 mm/s; squares: v_o = 217.8 mm/, v_i = 55.42 mm/s; triangles: v_o = 261.4 mm/s, v_i = 55.42 mm/s. The data shown as triangles are from the pattern of Fig. 5.7. The slopes of the lines through the data give the parameter ω of Eq. (2.44). (b) ω as a function of v_o. The circles are from (a), and the triangle from Fig. 5.15. The arrow indicates v_{oc}, the onset value for the stationary fingering pattern.

would therefore expect that this range of v_i should increase with v_o, as long as ϵ does not decrease too quickly as v_o is increased. This agrees with our experimental observations. At low values of v_o, the disordered traveling state was not observed in our experiments. This may be a result of the fact that ω would be very small at this low value of v_o, so that the range of existence of the disordered state is too small to be observed.

The temporal coexistence of the disordered state with the nonuniform traveling pattern reported above is also interesting. The intermittent appearances of the disordered pattern are related to the wavelength-changing transition we observed

the disorder appears more frequently near the transition -- but the nature of the relationship is not understood. Despite their nonuniformity, and their intermittent disruption by the disordered bursts, aspects of the behaviour derived in the context of spatially-uniform broken-parity waves remain valid for our patterns. At low v_i, the pattern's average phase speed, v_ϕ, grows as the square root of v_i, and the asymmetry, though noisier, is also proportional to $v_i^{1/2}$, as shown in Figs. 5.8 and 5.23. Fig. 5.24 shows that v_ϕ is proportional to $\mathcal{A}$ at low speed. The linear relationship between v_ϕ and $\mathcal{A}$ also holds for the individual fingers in the nonuniform pattern at a given time, as was illustrated in Fig. 5.25(a). These results are all in agreement with the theoretical and experimental results for uniform patterns.

Cummins et al. [84] described a series of transitions in fingering patterns in an experiment very similar to ours. Their experiments were performed in the fourth quadrant of Fig. 1.3. Fig. 5.26 is the phase diagram of their experiment in this quadrant. They fixed v_o at a small negative value, then increased v_i. Beyond the parity-breaking transition, the wavelength of their pattern decreased. They then saw a transition (from "Small" to "Large" in Fig. 5.26) at which the wavelength of their pattern increased by roughly a factor of two, before decreasing again as v_i was

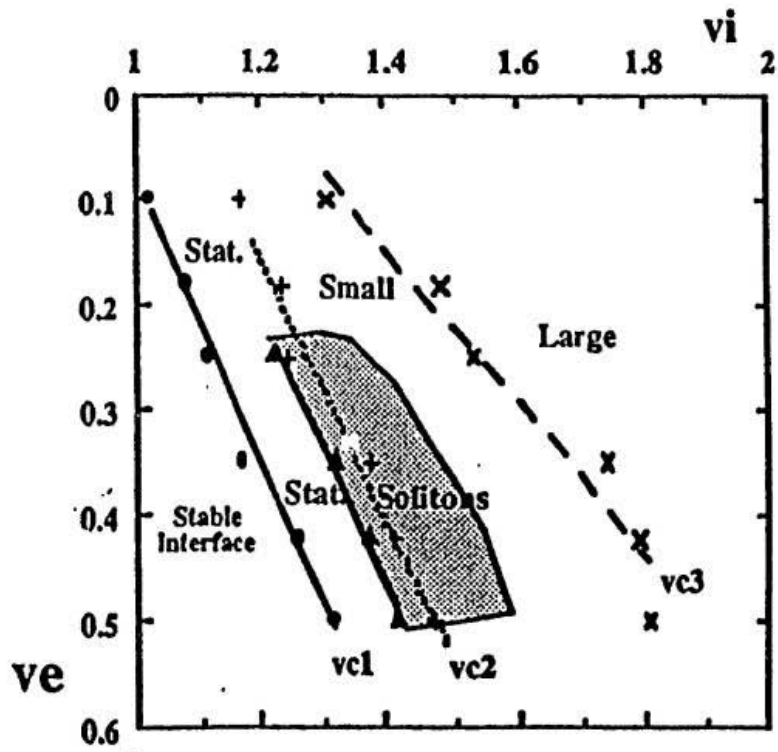

Figure 5.26: Partial phase diagram from Ref. [84]. Stat.: stationary finger state; Small: short-wavelength traveling waves; Large: long-wavelength traveling waves.

further increased. According to Fig. 5.26, this wavelength-changing transition exists in a limited range of v_i. If v_i is fixed at a value within this range, and v_o increased in counter-rotating direction, one should observe a wavelength drop, as in our experiments. In this case our results are consistent with theirs. In another set of experiments, they fixed v_i at a value beyond this wavelength-changing transition. They observed that, as v_o is decreased below zero, the phase speed of the pattern increased linearly with the square root of v_o to a maximum, and then decreased. Our results are consistent with this, as shown in Fig. 5.9.

Cummins et al. [84] also note that the short-wavelength fingers they observe before the wavelength-changing transition had well-defined wavelengths, but some scatter in velocity. In contrast, the long-wavelength fingers observed above the transition had considerable scatter in their wavelength, but well defined velocities. We observed a systematic variation in both wavelength and velocity with position in the pattern, rather than random scatter, and, as shown in Fig. 5.7, the variations are coupled. An important point is that for the long-wavelength fingers in Ref. [84] as well as for our patterns, the wavelength selection is not perfect, and in both cases a range of wavelengths is observed. Goldstein et al. [26, 27] have discussed the behavior of broken-parity traveling waves near spatiotemporal defects. They studied a generalization of the coupled equations, Eqs. (2.43) and (2.44), in which ϕ is the phase of a complex field, and reconstructed the patterns near source and sink defects using their model far above onset. Their results are shown in Fig. 5.27. As can be seen in Fig. 5.27, the mechanism by which fingers vanish at a sink defect in their model is very similar to that of the Eckhaus instability. At the defect, the broken-parity order parameter approaches zero, which causes distortions of the pattern. Close to a sink, the pattern is compressed and its phase speed is smaller relative to the uniform, propagating pattern far from the defect. Near a source, the

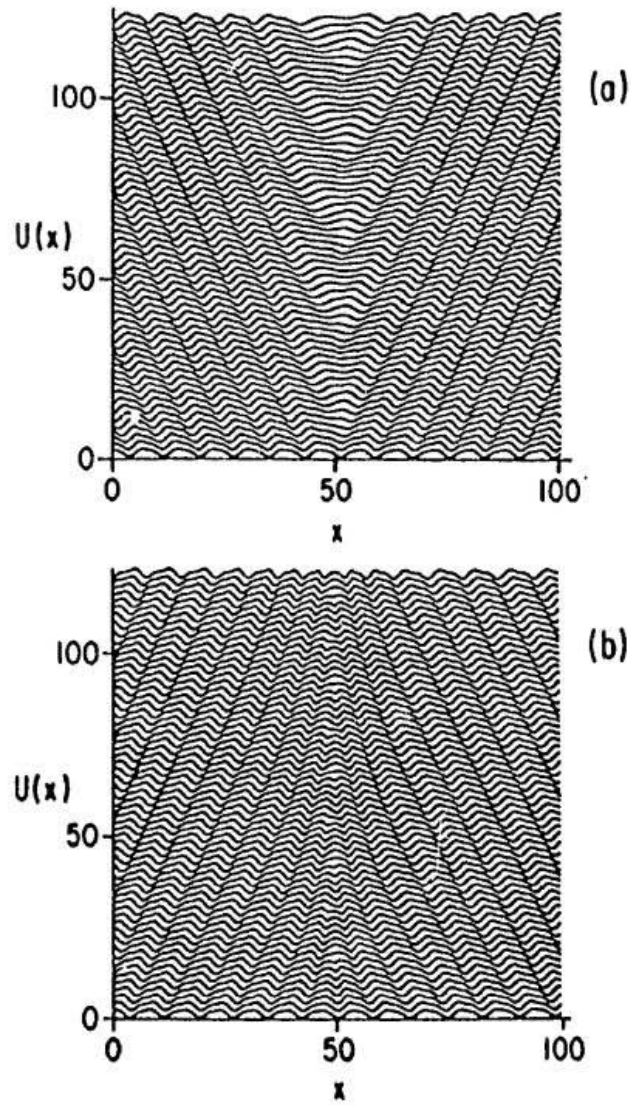

Figure 5.27: Two types of spatiotemporal grain boundaries for traveling waves from Ref. [27]. (a) A source of traveling waves; (b) a sink. Time runs from bottom to top.

pattern is stretched and travels faster. This behaviour is in accord with what we observed close to source and sink defects, as described above, although our patterns are not uniform away from the defects in this parameter range.

Previous experiments on the Eckhaus instability in traveling-wave systems [54, 56, 57, 58] mentioned in Chapter 1 were done by manipulating the system so as to attain a state with an average wavelength outside of the Eckhaus-stable band. The evolution of the pattern was then studied. The Eckhaus instability is a phase instability, and at least initially, manifests itself as a spatial modulation of the pattern's local wavenumber, with the pattern amplitude remaining constant. As the instability develops, amplitude variations eventually appear, and, at the point in space-time at which the pattern gains or loses a pattern unit, the amplitude must go to zero.

The situation in our experiment is rather different. Here, we do not prepare the system in any particular initial state. Rather, the system selects a spatially nonuniform state of its own accord, and the dynamics of this state lead to the occurrence of an instability when the pattern's wavelength evolves out of a stable wavelength band. This instability results in the birth or death of fingers, so as to bring the wavelength back inside the stable band. This adjustment of wave number by the creation or annihilation of pattern units is characteristic of the Eckhaus instability. We have assumed that the wavelength at which new fingers first attempt to develop corresponds to the long-wavelength boundary of the Eckhaus-stable wavelength band, and that the minimum wavelength below which adjacent fingers merge corresponds to the short-wavelength boundary. Our measured Eckhaus instability boundary is roughly parabolic at low v_i, which is qualitatively in agreement with the theoretical expectation based on the analysis using the complex Ginzburg-Landau equation described in section 2.3.1. However, the nonuniformity of the wavelength

along our patterns suggests that the pattern is already subject to a phase instability, independent of the creation or annihilation of fingers.

From the above results, we find that the behaviour of our system is in agreement with the theoretical expectations based on symmetry arguments. The phase speed of the traveling wave is linear in the asymmetry of the pattern, which is the order parameter of the the parity-breaking bifurcation. This linearity has been observed both in uniform and nonuniform traveling waves. At relatively low v_a, the parity-breaking transition is supercritical, and both the phase speed and the degree of asymmetry of the traveling pattern grow as the square root of the experimental control parameter. Our results are not, however, in agreement with the predictions specific to a model of the parity-breaking transition involving the coupling between modes with wave numbers q and $2q$, possibly because of the importance of other spatial modes in our pattern. At relatively high v_a, the phenomenology of our system is quite complex. The pattern is unstable at the onset of parity breaking, as predicted theoretically. Above onset, the pattern is nonuniform and subject to intermittent bursts of disorder. The pattern is also subject to the Eckhaus instability, which limits the band of wave numbers within which the individual traveling fingers are stable. There are several features of our results which warrant further investigation, including the nature of the transient disordered bursts and their connection with the wavelength-changing transition discussed above. A complete understanding of this system will also require further theoretical study.

Chapter 6

Conclusions

We have presented experimental results on the dynamical behaviour of a driven fluid-air interface in the system called the printer's instability. While a variety of dynamical states can occur in this system, this thesis has focused on two: the stationary fingering state observed when one cylinder rotates, and the traveling-wave which occurs when the cylinders counter-rotate.

The behaviour near onset of the stationary finger pattern observed when only one cylinder rotates depends on the size of the cylinders, and on which of cylinders is rotating. The bifurcation to stationary fingers is imperfect but continuous when the outer cylinder or the smaller inner cylinder rotates, and discontinuous when the bigger inner cylinder rotates. By comparing our results with theoretical expectations, and with previous experimental results, we find that finite-size effects can substantially delay the onset of the fingering instability, and shorten the onset wavelength. This result has potential applications in the coating industry. A traveling-wave state was observed with the bigger inner cylinder rotating. Here, as a single control parameter was increased, the oil-air interface first bifurcated to a stationary fingering pattern, then to a traveling pattern.

Our studies of the parity-breaking traveling-wave state, with the cylinders counter-rotating, show that the phase speed of the traveling wave is linear in the degree of asymmetry of the pattern. This linearity was observed both in uniform and nonuniform traveling waves. At relatively low v_o, the uniform traveling pattern appears via a supercritical parity-breaking transition, and both the asymmetry and the phase

speed of the pattern increase with the square root of the control parameter. These results are in good agreement with recent theoretical expectations on the basis of general symmetry arguments [25-27]. At higher ϵ_o, the phenomenology of our system is quite complex. The pattern is unstable at the onset of parity-breaking, as predicted theoretically. Above onset, the pattern is nonuniform and intermittent with bursts of disorder. A wavelength-changing transition is observed as ϵ_i is increased above onset. The traveling pattern is also subject to the Eckhaus instability, which limits the band of wave numbers within which the individual traveling fingers are stable.

We also compared our results on the traveling-wave state with the predictions of a specific model of the parity-breaking bifurcation, involving the resonant coupling between spatial modes with wave numbers q and $2q$. However, our results do not agree with these predictions, possibly because of the importance of higher spatial modes in our pattern.

There are several of our results which warrant further investigation. These include the traveling-wave state observed with one cylinder rotating, as well as the nature of the transient disordered bursts observed when the cylinders counter-rotate, and their connection with the wavelength-changing transition. A complete understanding of this system will also require further theoretical study

Bibliography

[1] M. C. Cross and P. C. Hohenberg, *Rev. Mod. Phys.* **65**, 851 (1993).

[2] F. H. Busse, in *Hydrodynamic Instabilities and the Transition to Turbulence*, ed. H. L. Swinny and J. P. Gollub (Springer, Berlin, 1985), p. 97.

[3] G. Ahlers, in *Lectures in the Science of Complexity*, ed. D. L. Stein (Addison, Reading, 1989) p. 175.

[4] Paul Manneville, *Dissipative Structures and Weak Turbulence*, (Academic, Boston, 1990).

[5] M. Dubois and P. Bergé, *J. Fluid Mech* **85**, 64 (1978).

[6] R. C. Di Prima and H. L. Swinney, in *Hydrodynamic Instabilities and the Transition to Turbulence*, ed. H. L. Swinney and J. P. Gollub (Springer, 1985) p. 91.

[7] I. Mutabazi, J. Hegseth, and C. D. Andereck, *Phys. Rev. A* **38**, 4752 (1988).

[8] I. Mutabazi and C. D. Andereck, *Phys. Rev. Lett.* **70**, 1429 (1993).

[9] A. J. Simon, J. Bechhoefer and A. Libchaber, *Phys. Rev. Lett.* **61**, 2574 (1988).

[10] J.-M. Flesselles, A. J. Simon and A. J. Libchaber, *Adv. Phys.* **40**, 1 (1991).

[11] F. Daviaud, M. Bonetti and M. Dubois, *Phys. Rev. A* **42**, 3388 (1990).

[12] M. Rabaud, S. Michalland and Y. Couder, *Phys. Rev. Lett.* **64**, 184 (1990).

[13] Y. Couder, S. Michalland, M. Raband and H. Thomé, in *Nonlinear Evolution of Spatio-Temporal Structures in Dissipative Continuous Systems*, ed. F. H. Busse and L. Kramer (Plenum, New York, 1990) p. 487.

[14] S. Michalland, Ph. D. Thesis, Université de Paris VI, 1992, (unpublished).

[15] L. Pan and J. R. de Bruyn, *Phys. Rev. Lett.* **70**, 1791 (1993).

[16] L. Pan and J. R. de Bruyn, to be published in *Spatio-Temporal patterns in Nonequilibrium Complex Systems*, ed. P. Cladis and P. Palffy-Muhoray.

[17] L. Pan and J. R. de Bruyn, *Phys. Rev. E* (to be published).

[18] G. Faivre, S. de Cheveigné, C. Gunaratne, and P. Kurowsky, *Europhys. Lett.* **63**, 154 (1989).

[19] G. Faivre and J. Mergy, *Phys. Rev. A* **46**, 963 (1992).

[20] G. Faivre and J. Mergy, *Phys. Rev. A* **45**, 7320 (1992).

[21] S. Douady, S. Fauve, and O. Thual, *Europhys. Lett.* **10**, 309 (1989).

[22] M. Dubois, F. Daviaud and M. Bonetti, in *Nonlinear Evolution of Spatio-Temporal Structures in Dissipative Continuous Systems*, ed. F. H. Busse and L. Kramer (Plenum, New York, 1990) p. 1.

[23] M. Raband and V. Hakim, in *Instabilities and Nonequilibrium Structures III*, ed. E. Tirapegui and W. Zeller (Kluwer, Dordrecht, 1991), p. 217.

[24] J. T. Gleeson, P. L. Finn, and P. E. Cladis, *Phys. Rev. Lett.* **66**, 236 (1991).

[25] P. Coullet, R. E. Goldstein, and G. H. Gunaratne, *Phys. Rev. Lett* **63**, 1954 (1989).

[26] R. E. Goldstein, G. H. Gunaratne, and L. Gil, *Phys. Rev. A* **41**, 5731 (1991).

[27] R. E. Goldstein, G. H. Gunaratne, L. Gil, and P. Coullet, *Phys. Rev. A* **43**, 6700 (1991).

[28] B. Malomed and M. I. Tribelsky, *Physica* (Amsterdam) **14D**, 67 (1984).

[29] G. Dangelmayer, *Dyn. Stab. Syst.* **1**, 159 (1986).

[30] C. A. Jones and M. R. E. Proctor, *Phys. Lett. A* **121**, 224 (1987).

[31] M. R. E. Proctor and C. A. Jones, *J. Fluid Mech.* **188**, 301 (1988).

[32] D. Armbruster, J. Guckenheimer, and P. Holmes, *Physica (Amsterdam)* **29D**, 257 (1988).

[33] D. Armbruster, J. Guckenheimer, and P. Holmes, *SIAM J. Appl. Math.* **49**, 676 (1989).

[34] S. Fauve, S. Douady, and O. Thual, *Phys. Rev. Lett.* **65**, 385 (1990).

[35] S. Fauve, S. Douady, and O. Thual, *J. Phys. (Paris) II* **1**, 311 (1991).

[36] H. Levine and W.-J. Rappel, *Phys. Rev. A* **42**, 7475 (1991).

[37] H. Levine, W.-J. Rappel, and H. Riecke, *Phys. Rev. A* **43**, 1122 (1991).

[38] W.-J. Rappel and H. Riecke, *Phys. Rev. A* **45**, 846 (1992).

[39] H. Riecke and H.-G. Paap, *Phys. Rev. A* **45** (1992).

[40] B. Caroli, B. Caroli, and S. Fauve, *J. Phys. (Paris) I* **2**, 281 (1992).

[41] K. Kassner and C. Misbah, *Phys. Rev. Lett.* **65**, 1458 (1990).

[42] P. Coullet and G. Iooss, *Phys. Rev. Lett.* **64**, 866 (1990).

[43] W. Eckhaus, *Studies in Nonlinear Stability* (Springer, Berlin, 1965).

[44] L. Kramer and W. Zimmermann, *Physica* , **16D**, 221 (1985).

[45] M. Lowe and J. P. Gollub, *Phys. Rev. Lett.*, **55**, 2575 (1986).

[46] S. Rasenat, E. Braun, and V. Steinberg, *Phys. Rev. A*, **43**, 5728 (1991).

[47] M. A. Dominguez-Lerma, D. S. Cannell, and G. Ahlers, *Phys. Rev. A*, **34**, 4956 (1986).

[48] G. Ahlers, D. S. Cannell, M. A. Dominguez-Lerma, and R. Heinrichs, *Physica D*, **23**, 202 (1986).

[49] H. Riecke and H.-G. Paap, *Phys. Rev. A*, **33**, 547 (1986).

[50] L. Ning, G. Ahlers, and D. S. Cannell, *Phys. Rev. Lett.* **64**, 1235 (1990).

[51] L. Fourtune, W.-J. Rappel, and M. Rabaud, unpublished.

[52] W. van Saarloos and P. C. Hohenberg, *Physica* **56D**, 303 (1992).

[53] H. R. Brand and R. J. Deissler, *Phys. Rev. A*, **45**, 3732 (1992).

[54] B. Janiaud, A. Pumir, D. Bensimon, V. Croquette, H. Richter, and L. Kramer, *Physica* **55D**, 269 (1992).

[55] B. Janiaud, E. Guyon, D. Bensimon, and V. Croquette, in *Nonlinear Evolution of Spatio-temporal Structures in Dissipative Continuous Systems*, ed. F. H. Busse and L. Kramer (Plenum, New York, 1990), p. 45.

[56] G. W. Baxter, K. D. Eaton, and C. M. Surko, *Phys. Rev. A* **46**, R1735 (1992).

[57] P. Kolodner, *Phys. Rev. A* **46**, R1739 (1992).

[58] P. Kolodner, *Phys. Rev. A* **46**, 6431 (1992).

[59] J. R. A. Pearson, *J. Fluid Mech.* **7**, 481 (1960).

[60] E. Pitts and J. Greiller, *J. Fluid Mech.* **11**, 33 (1961).

[61] G. Taylor, *J. Fluid Mech.* **16**, 595 (1963).

[62] C. C. Mill and G. R. South, *J. Fluid Mech.* **28**, 523, (1967).

[63] M. D. Savage, *J. Fluid. Mech.* **80**, 743 (1977).

[64] M. D. Savage, *J. Fluid Mech.* **80**, 757 (1977).

[65] M. D. Savage, *J. Fluid Mech.* **117**, 443 (1982).

[66] H. Benkreira, M. F. Edwards, and W. L. Wilkinson, *Chem. Eng. Sci.* **36**, 429 (1981).

[67] K. J. Ruschak, *Ann. Rev. Fluid Mech.* **17**, 65 (1985).

[68] D. J. Coyle and C. W. Macosko, *J. Fluid Mech.* **171**, 183 (1986).

[69] D. J. Coyle, C. W. Macosko, and L. E. Scriven, *J. Fluid Mech.* **216**, 437 (1990).

[70] D. A. Reinelt (unpublished).

[71] C. K. Aidun, *Tappi J.* **74(3)**, 213 (1991).

[72] P. G. Saffman and G. I. Taylor, *Proc. Roy. Soc. London A* **245**, 312 (1958).

[73] V. Hakim, M. Rabaud, H. Thomé, and Y. Couder, in *New Trends in Nonlinear Dynamics and Pattern-Formation Phenomena*, ed. P. Coullet and P. Huerre (Plenum, New York, 1990) p. 327.

[74] M. Rabaud, Y. Couder, and S. Michalland. *Eur. J. Mech. B/Fluids* **10**, 253 (1991).

[75] J. Beechhoefer, A. Simon, A. Libchaber, and P. Oswald, *Phys. Rev. A* **40**, 2042 (1989).

[76] H. E. Cline, *Metall. Trans.* **15**, 1013 (1984)

[77] S. Michalland and M. Rabaud, *Physica* **61D**, 197 (1992).

[78] S. Michalland, M. Rabaud, and Y. Couder, *Europhys. Lett.* **22**, 17 (1993).

[79] M. Decré, E. Gailly, J. Buchlin, and M. Rabaud, to be published in *Spatio-Temporal patterns in Nonequilibrium Complex Systems*, ed. P. Cladis and P. Palffy-Muhoray.

[80] K. Kaneko, *Prog. Theor. Phys.* **74**, 1033 (1985).

[81] H. Chaté and P. Manneville, *Phys. Rev. Lett.*, **58**, 112 (1987).

[82] S. Ciliberto and P. Bigazzi, *Phys. Rev. Lett.* **60**, 286 (1988).

[83] F. Daviaud, M. Dubois, and P. Bergé, *Europhys. Lett.* **9**, 441 (1989).

[84] H. Z. Cummins, L. Fourtune, and M. Rabaud, *Phys. Rev. E* **47**, 1727 (1993).

[85] R. J. Wiener and D. F. McAlister, *Phys. Rev. Lett.* **69**, 2915 (1992).

[86] D. J. Acheson, *Elementary Fluid Dynamics*, (Oxford University Press, New York, 1990).

[87] P. Tabeling, G. Zocchi, and A. Libchaber, *J. Fluid Mech.* **177**, 67 (1987)

[88] J. Greener, T. Sullivan, B. Turner, and S. Middleman, *Chem. Engng Commun* **5**, 73 (1980).

[89] H. Benkreira, M. F. Edwards, and W. L. Wilkinson, *Plastics Rubber Proc. Appl.* **2**, 137 (1982).

[90] M. Boucif, J. E. Wesfreid, and E. Guyon, *J. Phys. (Paris) Lett.* **45**, L413 (1984).

[91] D. S. Riley and S. H. Davis, *Phys. Fluids A* **1**, 1745 (1989).

[92] M. R. E. Proctor, *Phys. Fluids A* **3**, 299 (1991).